Mild-Slope Wave Modelling for Dynamic Mooring Analyses

An exploratory study into an efficient alternative to the wave penetration model

S.J. Dijsselbloem

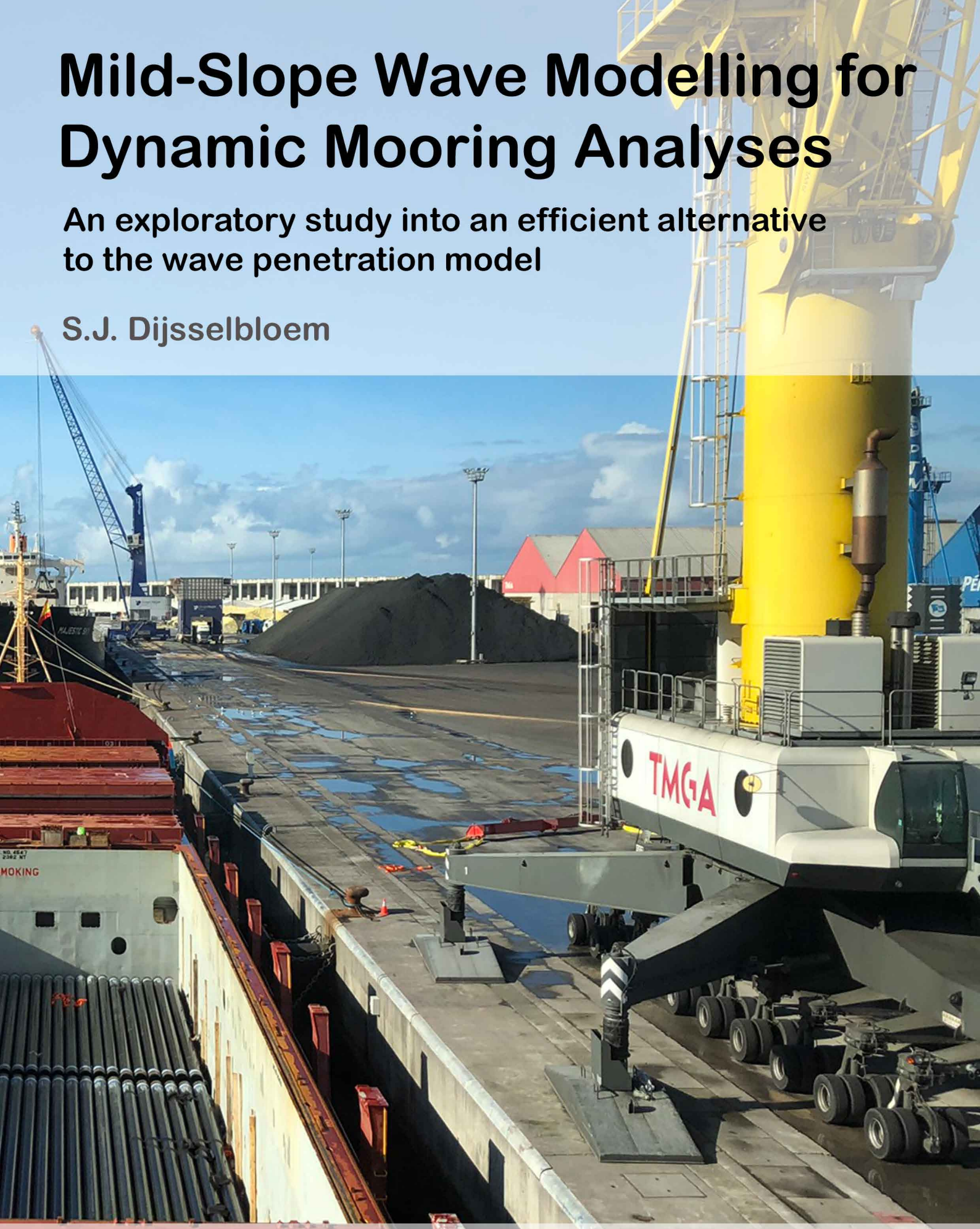

TU Delft Delft University of Technology
Royal HaskoningDHV Enhancing Society Together
Deltares Enabling Delta Life

Mild-Slope Wave Modelling for Dynamic Mooring Analyses

An exploratory study into an efficient alternative to the wave penetration model

by

S.J. Dijsselbloem

to obtain the degree of Master of Science
at the Delft University of Technology,
to be defended publicly on September 24, 2020 at 15:00 hrs

Student number:	4310233	
Project duration:	August 1, 2019 – September 24, 2020	
Thesis committee:	Prof. dr. ir. M. van Koningsveld,	TU Delft, chair
	Ir. A. J. van der Hout,	TU Delft, supervisor
	Dr. ir. A. van Deyzen,	Royal HaskoningDHV, supervisor
	Prof. dr. ir. E. Peña Gonzalez	University of La Coruña
	Dr. ir. S. Schreier	TU Delft

An electronic version of this thesis is available at `http://repository.tudelft.nl/`.

TU Delft

Nomenclature

Wave modelling

α	Adjustable constant
γ_s	Coefficient breaker height
∇	Spatial derivative
ω	Radial frequency
Φ	Complex velocity potential
ρ	Density of water
a	Amplitude
c	Wave celerity
c_g	Group velocity
d	Depth
f_w	Wave friction coefficient
$F_{x,y,z}$	Force in x,y and z direction
g	Gravitational acceleration
h	Water depth
H_{m0}	Significant wave height
H_m	Maximum possible wave height
H_{rms}	Root mean square wave height
i	Imaginary number
k	Wave number
p	Pressure
Q_b	Fraction of breaking waves
S_ρ	Local production of water
t	Time
U	Current velocity
U_e	Effective amplitude of the horizontal velocity
u_x	Water velocity in x direction
u_y	Water velocity in y direction
u_z	Water velocity in z direction
W	Energy dissipation

Diffraction modelling

$\ddot{z}$	Acceleration in z-direction
$\dot{z}$	Velocity in z-direction
a	Added mass
A_{wl}	Surface at water level
b	Damping
c	Spring constant
GM_l	Metacentric height lateral direction
GM_t	Metacentric height transversal direction
$K_{xx,yy,zz}$	Moment of inertia x,y,z direction
m	Mass
x_g, y_g, z_g	Coordinates center of gravity
z	Displacement in z-direction

List of Abbrevations

APAC Port Authority of A Coruna. 48

AWAC Acoustic Wave And Current. 49, 86, 87

DMA Dynamic Mooring Analysis. ix, 1, 2, 7, 8, 84, 86

DSPR one-sided Directional Width of the Wave Spectrum. 79

GEAMA Water and Environmental Engineering Group. 48

GUI Graphical User Interface. 24

IMU Inertial Measurement Unit. 48

JONSWAP Joint North Sea Wave Project. 36, 37, 40, 41, 43, 44, 46

LDM Laser Distance Meter. 48

LF Low-Frequency. 77, 78, 84, 85

MARIN Marine Research Institute the Netherlands. 16

PHAROS Program for Harbour Oscillation; Mild-slope wave model developed by Deltares. 2, 3, 5, 8–10, 12, 19–24, 26, 29, 33, 36–38, 40, 41, 43–45, 49, 84–88, 91

r-DPRA Rotational Directional Phase Resolving Analysis. 20–25, 28, 39, 40, 91, 93, 94

RAO Response Amplitude Operator. 14, 17

RMSE Root Mean Square Error. 43

SWASH Simulating Waves til Shore; Non-Hydrostatic wave-flow model developed at Delft University of Technology. 84

TRITON Boussinesq-type wave model developed by Deltares. 84

UDC University of La Coruna. 48

VTS Virtual Tracking System. 48

Preface

This MSc Thesis concludes my time studying at the Delft University of Technology. The last year, I spend working on this thesis at Royal Haskoning DHV after getting introduced to the topic of Dynamic Mooring Analysis already during my internship at their Lima office. I am thankful for the opportunities the gave me to combine the research with the commercial side of the subject. The support I got from Alex van Deyzen and the Dynamic Mooring Analysis team was really helpful.

Moreover, I would like thank Arne van der Hout for the guidance and taking as much time as was needed to help me out. Both in the role of TU Delft supervisor as the knowledge of PHAROS from the Deltares side is greatly appreciated. Also from Deltares, Bas Reijmerink helped me a lot with the PHAROS model, providing support when errors appeared.

Also, the people from MARIN were of great use for me. Frédérick Jaouën, Verena Schaap and Anand Ashok helped me with both DIFFRAC and aNySIM and provided useful feedback on my research.

In November, 2019, I spend two weeks at the University of La Coruña in Spain to help with the field measurements and collect data. I had a wonderful time there and the port visits were very interesting. I would like to thank Enrique Peña González for the guidance during the two weeks and for being part of the committee. Moreover, Raquel, Alex, José and Andrés made my stay both informative as amusing. In depth information about the history of the port and its operations I got from Enrique Maciñeira, for which I am very thankful. The people from Aquática provided the reflection coefficients of the boundaries, measured data and insights in the modelling of the outer port, I am very thankful for their contribution.

Last but definitely not least, I would like to thank my parents, family, friends and roommates for always supporting me, providing feedback and help me get through difficult times. Without this support, I would never have been able to keep my motivation. My friends really made my time in Delft very exciting, joyful and full of great experiences.

During the past 7 years in Delft, I promised myself to say 'yes' as much as I could, which resulted in many great experiences abroad: Spending half a year studying in Valencia, writing my BSc Thesis in Mozambique, doing a multidisciplinary project in Buenos Aires and the internship in Lima that initiated my interest in the subject of dynamic mooring analysis. I can look back very pleased on these experiences and I am looking forward to experiences that are yet to come.

S.J. Dijsselbloem
Delft, May 2020

Summary

Moored vessels in harbours around the world are affected by waves penetrating into the port basin. Hydraulic conditions can lead to severe vessel motions that influence the (un)loading efficiency. Moreover, it can eventually lead to the failure of fenders and mooring lines, creating unsafe situations for operating staff and structural damage.

A Dynamic Mooring Analysis (DMA) is a chain of numerical models that computes motions of moored vessels due to wind, currents or waves. It is used to model the behaviour of moored ships to evaluate operational conditions and assess the effect of structural or operational measures. The most computational costly model in the DMA model chain is the wave penetration model, which computes a local wave field. Currently, computationally more demanding wave models are applied, with computation times reaching up to multiple days or even weeks. Speeding up this part of the model chain can reduce time and costs of DMA's.

A different perspective from most DMA related research is taken by aiming to reduce required time for DMA's instead of improving the accuracy. In this research, the complex wave model is replaced by a computationally efficient alternative and its performance is evaluated. The main research question that is answered reads: *How can a mild-slope wave model be used for the ship motion calculation on ships moored in ports and what are the benefits and limitations?*

In order to answer this question, the research is split up into two parts: 1) Development of the coupling method and evaluating its application based on academic test cases, and 2) Applying the coupling to the case study of La Coruña, assessing its suitability and identifying important elements.

A practical and efficient coupling method is using the r-DPRA tool, developed by Deltares, to extract wave components from the wave penetration models wave field and directly imposing these components into the ship motion model. The accuracy of the wave height found by the r-DPRA tool is in the order of +/- 10%. The quay wall at the berth is modelled in the ship diffraction model to include the effect of it on the added mass and damping coefficients of the ship.

The newly developed method is applied to the case study of the port of La Coruña. In La Coruña, a measurement campaign was done over the last 5 years to measure the motions of moored vessels. An inertial measurement unit was placed on the bridge of the ship to capture the rotations, laser distance meters on the quay captured the sway motion and a camera using visual tracking captured the surge and heave motions. The vessel Aloe is chosen to be modelled and two separate moments in time are selected, one with moderate offshore wave conditions and one with more severe conditions.

In the measured time series of the surge and sway motions, a clear low frequency can be found. In the simulated time series of the surge and sway motions; both in moderate and heavy cases no low frequency wave patterns can be found. A hypothesis is that this low frequency pattern is caused by long waves, a non-linearity that is not modelled in the linear wave model. To take this effect into account, a schematic approach was used to include these waves in the wave model and ship motion model.

When this low frequency effect is included in the model chain, the low frequency wave pattern becomes visible in the time series of the surge and sway motions, see Figure 1. It improves the statistical parameters as well, leading to more accurate significant motions for surge and heave. The low frequency peak of the motion spectrum of the measured surge motion is found at a period of around 75 seconds. The modelled surge motion spectrum, however, does not show a clear peak at this wave period. A decay test is done to find the natural periods of the moored vessel and it is found to be much lower, around 31 seconds. This shows a discrepancy between the measured vessel and modelled vessel and can be a cause of the difference in motions. However, the approach to model the vessel is the same as it would be when used in a DMA, and is therefore

realistic with the available information.

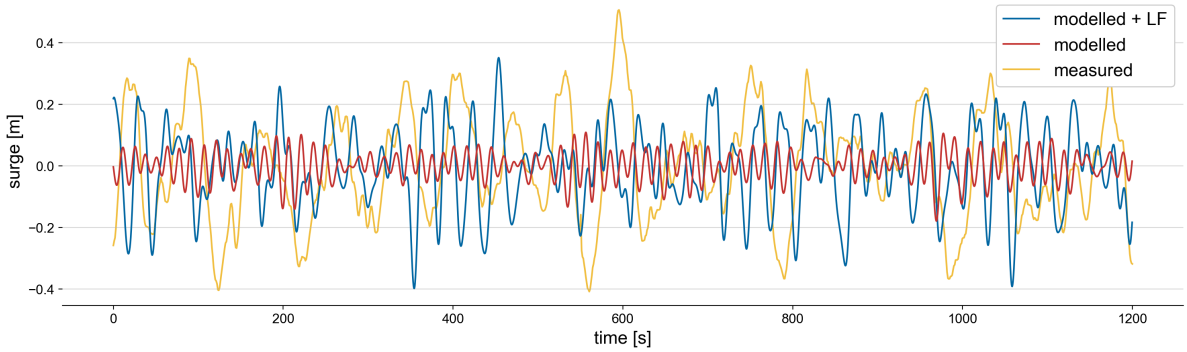

Figure 1: Comparison time series base case, including low frequency (LF) approach

In this research, the comparison is made with full scale measurements. This approach introduces uncertainties that complicate direct comparison of results. It can, however, identify elements and processes that are relevant for the dynamic mooring analysis concept. The aim of DMA's in general is to model the future real life situation and therefore the step to full scale measurements must also be made when starting with scale model tests. This emphasizes the exploratory character of this research in the broader idea of making DMA's more efficient to be used for preliminary studies.

Finally, the main research question is answered: *How can a mild-slope wave model be used for the ship motion calculation on ships moored in ports and what are the benefits and limitations?*

To conclude, a direct coupling using the r-DPRA tool was considered to be the most suitable and an efficient method of coupling for this particular research and was therefore applied. The comparison between the measured motions and modelled motions demonstrated the complexity of modelling real life events. As the surge and sway motions are caused by second order effects, which are not included in the applied linear wave model, an additional step must be applied to schematically include this long wave forcing. The result of this research demonstrates a clear potential for the development method. However, before applying it in practise, more fundamental research is required.

It is recommended to test the suitability of the method on a more fundamental case, e.g. the scale model data set of Deltares. This reduces uncertainties related to real life measurements and more conclusions about the performance of the coupling can be drawn. Moreover, the coupling should be tested for a case where the 2nd order low frequency wave forcing is negligible, as it is confirmed in this research that the developed method is less suitable for modelling non-linear 2nd order low frequency waves.

Contents

1 Introduction

1.1. Problem Description

Moored vessels in harbours around the world are affected by waves penetrating into the port basin. These waves lead to the dynamic forcing of moored vessels. With the fenders and the mooring lines, moored vessels behave as a mass-spring system. Hydraulic conditions can lead to severe vessel motions that influence the (un)loading efficiency. Moreover, it can even lead to the failure of fenders and mooring lines, creating unsafe situations for operating staff and structural damage. Engineering firms are frequently consulted to assess the moored behaviour of vessel and propose measures to reduce the downtime of a port. The downtime is the time a port is not able to operate, mostly due to environmental conditions like waves, currents and wind. Other factors influencing the downtime can be related to tidal windows, fog, rain, damaged equipment, working schedules or strikes. To determine the downtime related to environmental conditions, a so-called Dynamic Mooring Analysis (DMA) is performed.

A Dynamic Mooring Analysis is a chain of numerical models that computes motions of moored vessels due to wind, currents or waves. Jointly, with the fenders and mooring lines, vessels will respond to this forcing. Especially when the incoming waves have a period close to the natural period of the moored vessel, the response can become relatively high due to the resonant behaviour. Before investing in structural measures, a DMA can evaluate the influence of these measures. Moreover, DMA 's can be used in the design phase of a greenfield port to optimize the lay-out of the port basin in terms of hydrodynamics.

To perform a DMA, different combinations of numerical models are coupled, each with their own characteristics. The first model in the chain is a wave penetration model that computes the local wave field at the location of the moored ship based on offshore wave data. Second, a ship diffraction model translates the local wave field to forces on the vessel. Lastly, a ship motion model combines these two models and simulates the interaction between waves, ship and mooring equipment.

Various researches have coupled wave penetration models with ship diffraction and ship motion models. However, the coupled wave penetration models were often the more complex models. Van der Ven (2012) used TRITON and Dobrochinski (2014) and Wang (2018) both applied SWASH. Both these models are considered to be computational intensive wave penetration models.

More complex wave penetration models are able to simulate waves more accurately, including the non-linear behaviour of waves. These models come with their limitations regarding applicability. Certain aspects can be limited, e.g. the wave frequency, the wave heights and the bottom slope. Moreover, these complex models are computationally expensive, as non-linear systems have to be solved which can require a fine spatial resolution or even a vertical grid. Computationally expensive relates to the amount of resources, e.g. time and power, that are required for a computation. In common practice, these complex non-linear, time-domain wave models are used to model the wave penetration into harbours for the assessment of moored ship behaviour.

In this research, an efficient alternative for the more complex wave models will be investigated. The wave penetration is in general the most computational intensive model of the chain, which emphasizes the relevance of a computational efficient alternative. Computation times can be in the order of days per wave condition for these complex models (Van Mierlo, 2014). The ship diffraction model simulations can take hours, while the ship motion model takes minutes to hours, therefore the potential benefit is the largest for the wave penetration modelling. When computational times reduce, more wave conditions can be run at the same costs. Moreover, it can used to get a quick indication that can be used for decision making.

A computational efficient alternative for the more complex wave penetration models is incorporated into the DMA chain. The computational efficient wave penetration model PHAROS is used as alternative for the complex wave penetration models. PHAROS, a mild-slope wave penetration model, is a linear wave model and can therefore be solved in frequency domain, making it a potential computational efficient alternative. When this mild-slope wave model can be used for DMA's, run times can decrease significantly, lowering the costs of complete DMA's. Typical computational times of PHAROS are in the order of hours per wave condition (Van Mierlo, 2014). However, Mild-slope models come with limitations as well, such as limited 2nd order processes modelling, and these must be taken into account when evaluating the performance of the models. PHAROS is combined with the ship diffraction model DIFFRAC and the ship motion model aNySIM.

Oude Vrielink (2016) first investigated the coupling between PHAROS and DIFFRAC, considering two different coupling methods and applying them for a single harmonic and comparing the results with a reference model known to give accurate results. As complex geometries, 2D-wave spectra were not modelled, and the comparison was done based on reference computations, there is still research needed on the applicability of the coupling method for realistic cases.

1.2. Research Objective

This research must be seen in the broader context of dynamic mooring analysis modelling. As stated in the previous section, much research has been done on using the complex, computational more demanding wave penetration models in the DMA model chain. This research takes a different perspective and does not aim to make the results more accurate, but looks at how much accuracy can be sacrificed in order to win valuable time. This is a complete different approach and therefore this research can be regarded as exploratory, paving the way for further research.

The objective of this research is to assess the performance of the coupling method between a mild-slope model, a diffraction model and a ship motion simulation model (PHAROS - DIFFRAC - aNySIM) for port layouts. After verifying the proposed method, it will be applied to the port of La Coruña to evaluate the potential of this method. This combination of models is used as DIFFRAC and aNySIM are the conventionally used models at RHDHV and are therefore directly available.

The main research question that is answered in this report reads:
How can a mild-slope wave model be used for the ship motion calculation on ships moored in ports and what are the benefits and limitations?

In Chapter 2, a literature review is done, discussing the used models and the previous research done of the coupling of them. Then, the sub questions are answered in the next chapters according to the following structure:

- **Chapters 3,4 and 5 - Development and Validation coupling method**
    1. How will the coupling between the mild-slope model and the diffraction model be done and why?
    2. Which processes have to be included in DIFFRAC and which in PHAROS?
    3. What is the most efficient way of processing the wave field in the ship motion model?
- **Chapter 6 - Field Measurements**
    4. Which measurements in the port of La Coruña are suited for the verification?

- **Chapter 7 - Comparison Computations and Field Measurements**

  5. Which elements are of importance to calibrate the results?
  6. How sensitive are the results to the different parameters?

- **Chapter 8 - Discussion on suitability of the developed method**

  7. What are the limitations of the developed method?
  8. What are the benefits of the new method in comparison with conventional methods in terms of computational time and set-up time?

1.3. Research approach

The structure of this research is composed of two phases. In the first phase, the coupling method is developed and tested for schematized academic cases and incorporated into the DMA model chain. In the second phase of the research, the developed method is applied to the case study of the Port of La Coruña. The port layout is modelled in PHAROS, the vessel and quay are modelled in DIFFRAC and the mooring equipment in aNySIM. The full DMA chain is done and the model results are compared with the measurements. In Figure 1.1, a schematization is shown of the research approach. The two phases are on the left, and the steps taken within each phase on the right.

1.3.1. PHASE I - Development Coupling Method

First, a literature study is undertaken to position this research in relation with previous studies. Further, the underlying theory of the models is presented to provide more understanding of the used models (Chapter 2).

Then, the coupling between PHAROS and aNySIM is set up (Chapter 3). Scripts are written that translate the output of the PHAROS runs to match the input format of aNySIM. Two different methods are discussed to couple the output from a mild-slope wave model to the input of a diffraction model / ship motion model. One based taking into account the spatial variation of the wave field along the hull and one taking the conditions at the ships center by using a tool developed by Deltares (De Jong and Borsboom, 2012). After evaluating both methods, a choice is made between these coupling methods. Then, an assessment is done to evaluate the coupling. A test model is setup for which the analytical solution is known. This test case is used to assess the performance of the coupling for simplified cases.

Henceforth, in Chapter 4, an assessment is done to find out the optimal configuration of the coupling, taking into account both accuracy and computational costs. The test model of the previous chapter is extended by including a quay wall. It is evaluated how to incorporate the quay wall of the berth in the most efficient way, either modelling it in PHAROS or DIFFRAC. In port basins, multiple quay walls and/or breakwaters can be present that can be modelled in DIFFRAC to describe interaction between the vessel and the surrounding port geometry, however, at high computational costs. Therefore, a smart selection has to be made which (port-geometry) elements need to be modelled in DIFFRAC and which can be modelled in the, for this aspect more computationally efficient, wave model PHAROS. Choices like this will always be an compromise between required accuracy and acceptable computational speed.

In Chapter 5, it is assessed how the conversion from PHAROS output to aNySIM input can be done in the most efficient way for full 2-dimensional wave spectra, as in reality would be the case. The coupling method developed in Chapter 3 is evaluated on suitability for full 2D wave spectra. Different ways of implementing the method are discussed and finally the most efficient and practical one is chosen.

1.3.2. PHASE II - Case Study Port of La Coruña

Then, the case study of the port of La Coruña is used to verify the suitability of the method. aNySIM translates the wave forces calculated by DIFFRAC to ship motions and line and fender forces. The modelled motions are then compared with the measurements to assess the performance of the coupling method.

A field visit to the port of La Coruña is done to retrieve both qualitative and quantitative data and to involve in the measurements campaign. These measurements are then evaluated on the basis of suitability and finally

two distinct moments in time are selected to be modelled for the DMA verification of the developed method, one with a moderate wave climate and one with a heavier wave climate (Chapter 6).

In Chapter 7, the layout of the Port of La Coruña is modelled in PHAROS. The bathymetry, grid and boundaries are discussed and the wave climate is defined for both moments. The selected vessel is modelled twice in DIFFRAC, as at both distinct moments the water level and vessel draught are unique. The mooring lines and fenders are modelled in aNySIM, as per the mooring configuration. A comparison is made between the measurements and the model results, both statistically as based on a visual inspection of the time series. Elements that influence the model performance are identified and evaluated by means of a sensitivity analysis.

In the last chapter, Chapter 8, the research questions aforementioned are answered. The answers to the research question finally lead to a general conclusion on the applicability and suitability of the developed method. Furthermore, the approach used for this research is discussed and evaluated. Finally, the benefits and limitations of the proposed method are discussed and recommendations for further research are given.

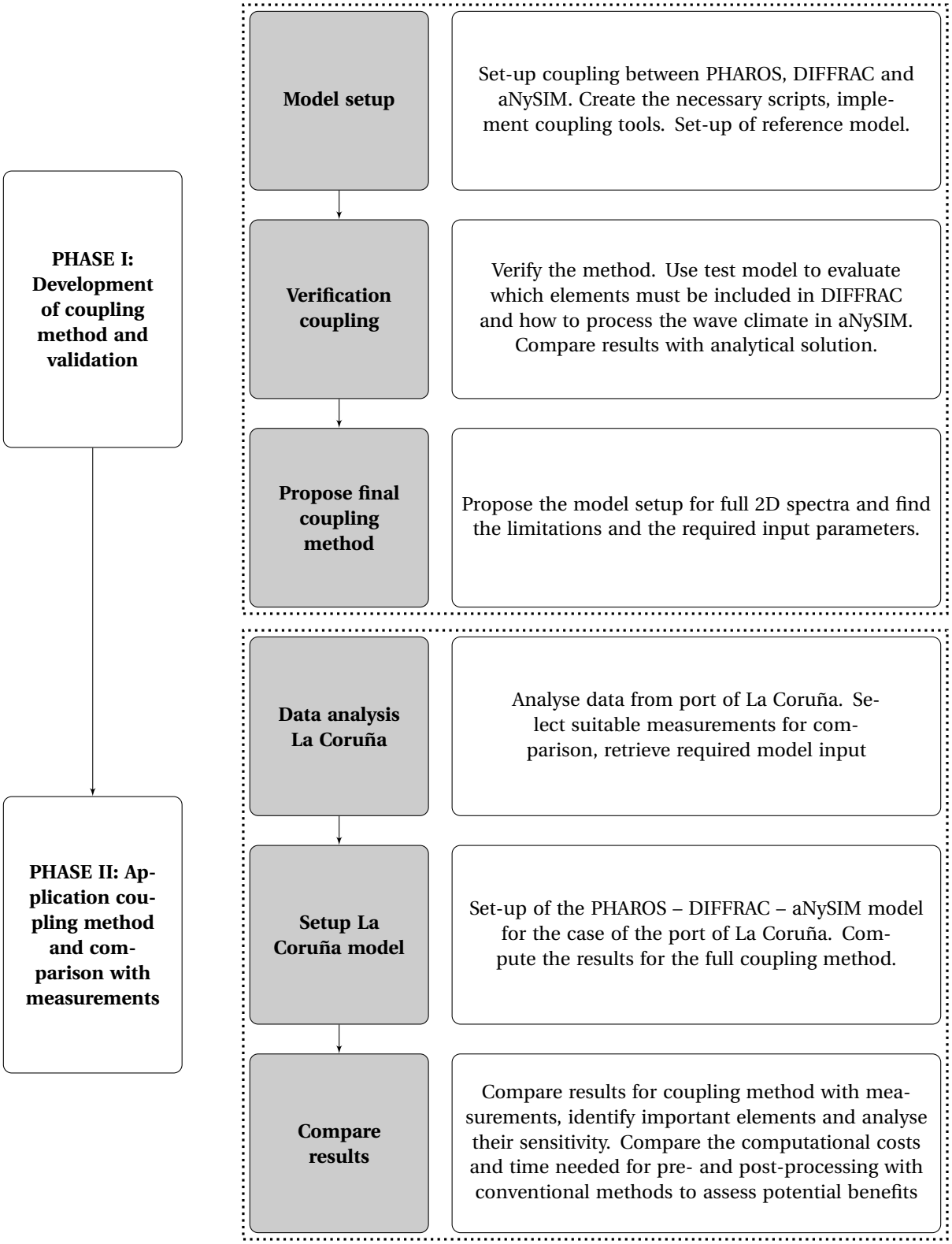

Figure 1.1: Research approach

2

Literature Review

In this chapter, an overview of DMA related research is given. Previous topics about coupling methods related to the DMA model chain are discussed. Then, the wave penetration model, wave diffraction model and ship motion model are discussed and their theoretical background is explained to provide insights in the physical processes that are modelled.

2.1. Coupling of Numerical models

Much research has been done about the coupling between numerical wave models, diffraction models and ship motion models, an overview of recent research is given in Table 2.1. Different model chains can be used, all with their own characteristics. In this section, an overview is given of the relevant research done so far. In Figure 2.1, the typical flow scheme of a DMA is shown. Wave models calculate wave potentials at the location of the ship, diffraction models translate potentials to forces on the hull of the ship and finally, the ship motion models translate the forces into ship motions.

Bingham (2000) described a computational technique for the modelling of wave induced force on moored ships using a Boussinesq-type wave model. The first order wave forcing was calculated in a frequency domain panel method and in time domain the ship motions were calculated, including the non-linear restoring forces.

Van der Molen and Wenneker (2006) developed two distinct methods for the modelling of waves in ports and the associated ship motions. The first method used a depth averaged non-linear flow model, that accurately models the low frequency wave propagation, but does not model the individual short waves. The second method used a Boussinesq type wave model coupled with a time-domain panel model and modelled both short waves as the bound long waves.

Van der Ven (2012) researched the coupling between TRITON (time domain Boussinesq-model), Harberth (time domain diffraction model) and QUAYSIM (time domain ship motion model). After comparing the computational results with the scale model tests results, it became clear that it is not straightforward to predict low frequency wave energy accurately both in numerical models as in physical scale models. As the deviations in the model, even after calibration, were significant, Harbert and QUAYSIM were not applied for the case study. It was emphasized that estimating ship motions purely on numerical model is discouraged and he recommended physical modelling for calibration. His research clearly indicates that even the computa-

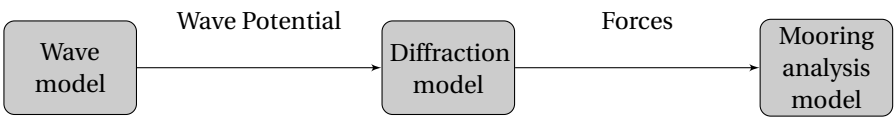

Figure 2.1: Typical flow chart of a DMA

tionally more demanding Boussinesq-type models not necessarily lead to the most accurate results.

Wang (2018) researched the coupling between SWASH and DIFFRAC. He developed a tool with a 'Full FFT' and a 'Partial Overlapping FFT' method. The tool appeared to be consistent for the test cases and the first order wave forces were generally well predicted. The coupling could not be validated for more complex harbour geometries.

The coupling between SWASH and Harberth, both time domain models, was researched by Dobrochinski (2014). It was proved that the dispersion error is negligible and the amplitude errors relatively small given that a sufficient number of vertical layers is used and the horizontal resolution is sufficient. This method was consistent for the simplified test cases and the first order wave forces were calculated accurately. This showed that the coupling between SWASH and Harberth has potential for being an alternative for future DMA's.

The coupling between PHAROS and ship diffraction model DIFFRAC has been researched by Oude Vrielink (2016). He compared two different methods of coupling and applied them on a simplified and idealised case:

1. r-DRPA tool: Extracting individual components at the location of the ship (De Jong and Borsboom, 2012).
2. A panel method that directly translates the wave potential to forces on the panels of the hull.

He concluded that that for a single harmonic the panel method performed slightly better.

Table 2.1: Overview recent research related to the coupling of models that can be used for a DMA

	Van de Ven 2012	Dobrochinski 2014	Wang 2018	Oude Vrielink 2016
Geometry	Port layout	Port layout	Port layout	Simplified
Wave model	TRITON	SWASH	SWASH	PHAROS
Diffraction model	Harberth	Harberth	DIFFRAC	DIFFRAC
Ship motion model	QUAYSIM	-	-	MOORINGS
Validation	Phys. scale tests	Phys. scale	Phys. scale	Numerical model

2.2. Wave Penetration Modelling

The objective of this research is investigating the suitability of using a mild-slope model (PHAROS) for a dynamic mooring analysis. First, the different wave model types are explained and subsequently compared based on previous research, to provide a better understanding of where the mild-slope models stand in comparison with the more complex wave penetration models and where the computational efficiency comes from. Then, mild-slope models are discussed with PHAROS in particular. Moreover, diffraction models and ship motion models are explained and compared.

2.2.1. Numerical wave penetration model types

Different type of numerical models can be used for modelling wave penetration inside a port basin. The most used model types are Boussinesq models , mild slope models and non-hydrostatic models . Each type of numerical model has its limits and its benefits.

Mild-slope models (PHAROS, HARES) are generally solved in the frequency domain and derived from the potential flow theory. As they are linear models, non-linear wave-wave interactions, such as bound long waves, are not included. Non-linear processes like bottom friction and wave breaking can be parameterized. Restrictions are set on the wave amplitude, the wave steepness and, as the name suggests, the bottom slope. Their main advantage is the computational efficiency, as they are solved in the frequency domain.

Boussinesq type models (TRITON, MIKE 21 BW) are also derived from potential flow theory. The vertical structure of the horizontal flow velocity is here not assumed constant, but approximated. This enables frequency dispersion and the modelling of non-linear waves and non-linear wave processes. Boussinesq models

are typically used in shallow water, as the kh value ($wavenumber \cdot waterdepth$), an indicator for the shallowness, is practically limited up to 3 or 4. This model type is especially suitable when non-linearities play a significant role. However, this model type is more computational expensive than the previously mentioned mild-slope models.

In the non-hydrostatic model type (SWASH), the vertical momentum balance is included and therefore a vertical grid is needed, making it a semi-3D model. Frequency dispersion can be accurately represented, depending on the vertical grid resolution. The extra vertical grid contributes to the relatively high computational costs of non-hydrostatic models. The non-linear process of bound long waves is accounted for in this model type.

In Figure 2.2, an overview is given of the different model types and their relation to each other.

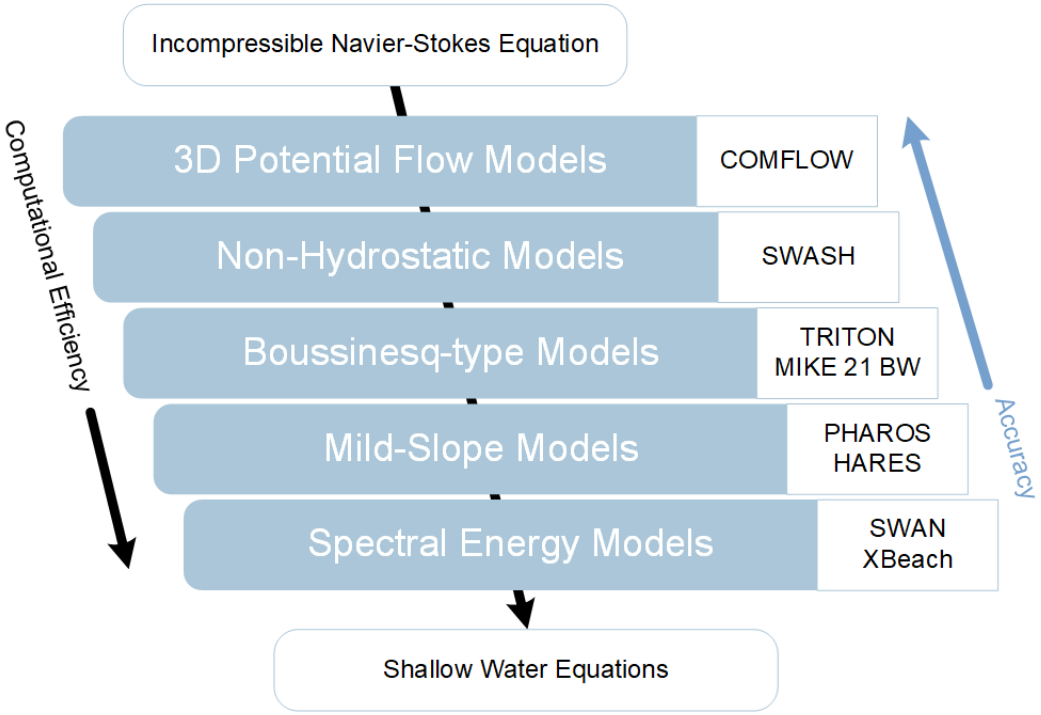

Figure 2.2: Schematization different numerical wave model types

2.2.2. Comparing wave penetration models

In this section, the relative performance of some of the afore mentioned wave models is discussed based on literature.

Van Mierlo (2014) used a dataset of physical scale model measurements provided by Deltares to compare the performance of TRITON, PHAROS and SWASH. These numerical methods represent Boussinesq-type, mild-slope and non-hydrostatic models respectively. Measurements from a physical scale test, representing a typical port layout, done by Deltares were used to compare the results of the different models. It concluded that TRITON and SWASH are capable of modelling primary waves in the harbour basin accurately. The PHAROS results were less accurate, overestimating wave height in sheltered zones. PHAROS was considered an appropriate tool to obtain a quick estimate of the wave height because of its efficiency and robustness.

Reijmerink (2012) compared the performance of SWAN and PHAROS for more complex harbour geometries with the more advanced wave model TRITON. He concluded that PHAROS performs well in ports without the presence of wind for the computation of significant wave heights. The model performed better for ports subjected to a wave spectrum with high directional spreading ($\sigma > 15°$). The performance of the model was proven to be independent of the complexity of the port layout. Furthermore, the PHAROS results were greatly

dependent on the number of discritized wave components. This is due to the standing wave pattern that occurs in the basin. For accurate comparison, a visual representation can best be used. Also for the spectral wave period, independent of the complexity of the geometry, the physical behaviour was modelled well. A special focus should be given to the reflective boundaries, mostly for cases with little directional spreading in the wave spectrum. This research shows that PHAROS is capable of modelling wave penetration into (complex) port basins, when the influence of locally generated wind waves is not significant.

Besides PHAROS, HARES has been developed by Svasek hydraulics. This mild slope model has been compared with spectral wave energy model SWAN and a 3D non-hydrostatic wave model SWASH. It was concluded that mild slope models combine the best of both worlds. The 2D time-independent spectral approach is computationally more efficient than the 3D time dependent model, like SWASH. The phase resolving of the mild slope models accurately includes diffraction as it is a phase related phenomena (Eikema et al., 2018).

2.2.3. Mild-slope models

A mild-slope wave penetration model is chosen to be used in the DMA model chain, because it offers more computational efficiency than the more complex wave models, but is still able to accurately model physical behaviour of waves inside port basin, in contrary with the even more computational efficient spectral wave models.

Mild-slope models are primarily based on the mild-slope equation, first described by Berkhoff (1972). The root of all mild-slope models is found in linear wave theory. This theory, also called airy wave theory, is based on the mass balance and momentum balance equations. When expressed in the velocity potential function (Φ) this results in the Laplace and Bernoulli equations. A propagating harmonic wave with a constant and relatively small amplitude is one of its solutions. The Laplace equation provides expressions for the (wave-induced) motions of the water particles. Applying a dynamic boundary condition, the dispersion relationship provides a relationship between the wave period and wave length (Holthuijsen, 2007).

Consequently, this leads to an expression for the phase speed and the group velocity. The linearised Bernoulli equation combined with the Laplace expressions, leads to an expression for the wave induced pressure in the water. Pressures integrated over the surface of a floating body lead to the forcing of this body.

Linear wave theory forms the basis of the mild-slope equation. The first assumption for Linear Wave theory is that the water is considered an ideal fluid and the water motions are only forced by the earth's gravitation force. An ideal fluid is assumed:

- To be in-compressible; The forces involved are relatively small so that the compression of the water can be ignored.
- To have a constant density; The horizontal scale on which oceanic water vary in density are much larger than the scale on which the linear theory is applied. Vertically, the density difference can play a role, therefore caution should be taken when applying linear wave theory in areas where temperature and salinity differences are expected.
- To have no viscosity; The effect of viscosity induced internal forces are negligible for the wave lengths considered (around 30 m and above). Moreover, the time variations are very slow so that these can be ignored.
- The water body is continuous. Linear wave theory does not apply when there is a significant discontinuity in the water, e.g. when it contains too many air bubbles. This is usually the case when waves break and in that case linear wave theory is not applicable. In that case, due to the wave steepness criterion, linear wave theory was already not applicable anymore.

Moreover, it's assumed that water particles cannot leave the water surface nor can they penetrate through the bottom. The only wave forcing that is considered is the gravitational force. This excludes other forcing mechanisms like surface tension, wave generation by wind, the Coriolis force and the influence of bottom friction. Furthermore, the wave height should be relatively small compared with the water depth and wave length (order of 5 to 10 % and for shallow water a wave height in the order of meters) and the water particles

are assumed to be irrotational, not rotating around their own axis.

The mass balance is based on the principle of a volume of water. The storage of an arbitrary quantity during a time interval is equal to the net import of that quantity plus the local production of that quantity during the same time interval. For the mass balance this quantity is the mass of the water itself, for the momentum balance equation this is the momentum.

Writing the above mentioned quantity as the density of water, the mass balance is formed. With ρ as the density of water, $u_x, u_y and u_z$ as the water velocities in x, y and z direction respectively and S_ρ the local production of water.

$$\frac{\delta\rho}{\delta t} + \frac{\delta\rho u_x}{\delta x} + \frac{\delta\rho u_y}{\delta y} + \frac{\delta\rho u_z}{\delta z} = S_\rho \tag{2.1}$$

Assuming constant density and no production of water, it is reduced to the continuity equation:

$$\frac{\delta u_x}{\delta x} + \frac{\delta u_y}{\delta y} + \frac{\delta u_z}{\delta z} = 0 \tag{2.2}$$

To create the momentum balance, the above mentioned quantity is taken as the mass density of water times the velocity of the water particles. This velocity is a vector quantity and therefore leads to the three component equations of the momentum balance. For the x-direction this leads to the following equation, with F_x the force in x-direction:

$$\frac{\delta(\rho u_x)}{\delta t} + \frac{\delta u_x(\rho u_x)}{\delta x} + \frac{\delta u_y(\rho u_x)}{\delta y} + \frac{\delta u_z(\rho u_x)}{\delta z} = F_x \tag{2.3}$$

As this equation still contains non-linear terms, these terms should be removed in order to comply with the linear wave theory. This leads to the linearised momentum balance equation:

$$\frac{\delta(\rho u_x)}{\delta t} = F_x \tag{2.4}$$

The forcing is solely due to gravity which is described by the horizontal pressure gradient in the water $\delta p/\delta x$. The force balance leads to

$$F_x = -\frac{\delta p}{\delta x} \tag{2.5}$$

Substituting this in the momentum balance equation leads to:

$$\frac{\delta u_x}{\delta t} = -\frac{1}{\rho}\frac{\delta p}{\delta x} \tag{2.6}$$

In the linearised momentum balance equation in the z-direction, the gravity term g is present due to the contribution of the weight of water body to the balance of forces.

The velocity potential (ϕ) function is introduced to find analytical solutions of the balance equations and their boundary conditions. The velocity potential is defined as a function of which the spatial derivatives are equal to the velocities of the water particles.

$$u_x = \frac{\delta\phi}{\delta x}, u_y = \frac{\delta\phi}{\delta y}, u_z = \frac{\delta\phi}{\delta z} \tag{2.7}$$

Substituting this velocity potential in the continuity equation leads to the Laplace equation:

$$\frac{\delta^2\phi}{\delta x^2} + \frac{\delta^2\phi}{\delta y^2} + \frac{\delta^2\phi}{\delta z^2} = 0 \tag{2.8}$$

When substituting the velocity potential function in the momentum balance and rewriting it, the linearised Bernoulli equation for unsteady flow is found:

$$\frac{\delta\phi}{\delta t} + \frac{p}{\rho} + gz = 0 \tag{2.9}$$

One of the analytical solutions of the Laplace equation is a long-crested harmonic propagating wave (ω as radial frequency, k as wave number and a as wave amplitude):

$$\eta(x,t) = a \cdot sin(\omega t - kx) \tag{2.10}$$

With the velocity potential function (d as water depth):

$$\phi = \frac{\omega a}{k} \frac{cosh[k(d+z)]}{sinh(kd)} \cdot cos(\omega t - kx) \tag{2.11}$$

Differentiating this velocity potential function to x, y and z leaves the corresponding velocities. E.g. for the x-direction, the velocity reads:

$$u_x = \omega a \frac{cosh[k(d+z)]}{sinh(kd)} \cdot sin(\omega t - kx) \tag{2.12}$$

2.2.4. PHAROS

PHAROS is chosen as the mild-slope wave model to be implemented in the DMA chain for practical reasons.

PHAROS, an acronym for *Program for Harbour Oscillation*, has been developed by Deltares to model wave agitation and harbour resonance (Deltares, 2018). In the engineering field, PHAROS is used to assess the hydrodynamic properties of the harbour, e.g. the effects of structural adjustments, quality of berthing locations and possible resonant wave conditions. Solving the mild-slope equation, PHAROS is capable of representing:

- Wave refraction over non-uniform depth profile
- Wave diffraction
- (partial) Wave reflection
- (partial) Wave transmission
- Energy dissipation by wave breaking and bottom friction (parameterized)
- Directional spreading of waves
- Frequency spreading of waves (wave spectrum)

The theoretical bases of PHAROS are the already mentioned linear wave theory assumptions and assumption that the wave steepness is small, allowing linearisation. With c as phase velocity and c_g the group velocity, the mild-slope equation reads:

$$\nabla(c \cdot c_g \cdot \nabla \cdot \phi) + k^2 \cdot c \cdot c_g \cdot \phi = -i \cdot \omega_r \cdot W \cdot \phi \tag{2.13}$$

In PHAROS, the non-linear processes of bottom friction and wave breaking are parameterized in order to be able to take them into account.
The energy source term, W represents the energy dissipation due to bottom friction and wave breaking.

$$W = W_b + W_f \tag{2.14}$$

Wave breaking, W_f, is modelled according to the formulation suggested by Battjes and Janssen (1978):

$$W_b = \frac{\alpha}{\pi} \cdot \omega_r \cdot Q_b \cdot \frac{H_m^2}{H_{rms}^2} \tag{2.15}$$

With:

$$H_s = \sqrt{2} \cdot H_{rms} \tag{2.16}$$

and:

$$\gamma_s = \frac{H}{h} = 0.8 \tag{2.17}$$

Bottom friction is based on the formulation of Putnam and Johnson (1949):

$$W_f = \frac{4}{3\pi} \frac{k}{sinh(kh)} f_w \frac{U_e}{cosh^2(kh)} \tag{2.18}$$

2.3. Ship Diffraction Modelling

The second model in the DMA chain is the ship diffraction model. This is not to be mistaken by the diffraction from a coastal engineering perspective. In this section, the theory behind these diffraction models is discussed and the used ship diffraction model DIFFRAC is explained.

2.3.1. Diffraction models

In Figure 2.3, the ship-fixed coordinate system used in describing ship motions. The three translations are called surge (x), sway (y) and heave (z) and the three rotations roll (ϕ), pitch (θ) and yaw (ψ).

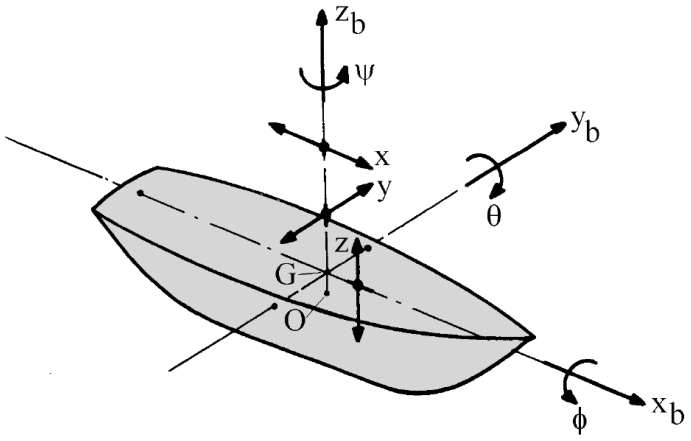

Figure 2.3: Ship-fixed coordinate system used for ship motions (Journée and Massie, 2001)

The next step towards ship motions is the calculation of wave forces on the hull of the ship. To describe the processes involved with ship motions, an analogy is made with a mass-spring-damper system, see Figure 2.4. In the case of a free floating vessel, the spring represents the buoyancy effect of the water, pushing the ship back to it's original position. When the vessel is moored, the spring constants are influenced by the mooring and fender forces. Buoyancy works mostly in the vertical direction and therefore only plays a significant role in the heave, roll and pitch motions for free floating vessels. The damper represents the radiated waves by the ship itself, passing energy to these radiated waves.

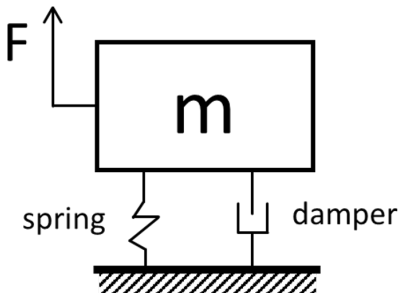

Figure 2.4: Mass-Spring-Damper analogy

The second law of Newton states that the sum of all forces on a body equals the mass times the acceleration. The system is linearized by separating the forces on the ship in the forces on a restrained ship and the forces of a oscillating ship in undisturbed water, see equation 2.19 and a schematization in Figure 2.5. The latter can be split into a hydrostatic force and a hydrodynamic force. The hydrostatic force is related to a ship's buoyancy. Archimedes' law states that the upward buoyant force that is exerted on a body immersed in a fluid is equal to the weight of the fluid that the body displaces and acts in upward direction at the center of mass of the displaced fluid.

$$m \cdot \ddot{z} = F_{hydrostatic} + F_{hydrodynamic} + F_{waves} \tag{2.19}$$

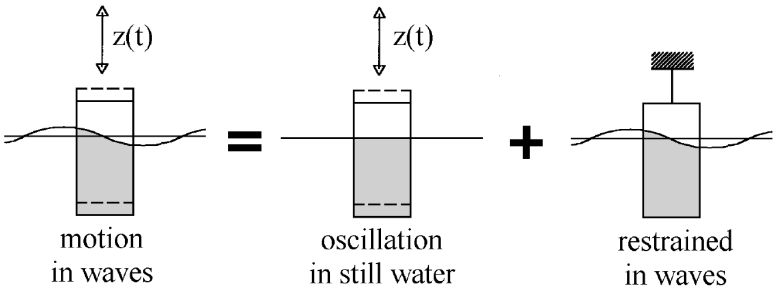

Figure 2.5: Superposition wave loads

$$m \cdot \ddot{z} = -c_3 \cdot z - a \cdot \ddot{z} - b \cdot \dot{z} + F_{waves} \tag{2.20}$$

$$(m + a) \cdot \ddot{z} + b \cdot \dot{z} + c \cdot z = F_{waves} \tag{2.21}$$

The added mass and damping are system properties and are dependent on the frequency and direction of oscillation. The forcing of the waves can be divided in the Froude-Krilov wave force and diffracted wave force. The Froude-Krilov force comes from the integration of the pressures of the undisturbed wave on the body. For very low frequencies, the Froude-Krilov forces are dominant, at higher frequencies the diffracted wave force becomes more important. The response of a body due to the wave forcing can be expressed as a Response Amplitude Operator (RAO). For every frequency, the relative response of that motion is given. A typical RAO for heave is shown in Figure 2.6. For very low frequencies, the heave amplitude follows directly the wave amplitude. Around the natural period of the system, the inertia and spring terms cancel out each other and the damping terms becomes dominant. For very high frequencies, the forcing is not strong enough to move the whole ship within that short period due to the inertia and therefore the heave amplitude goes to zero.

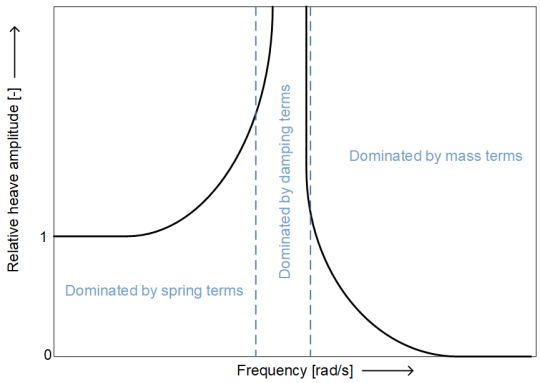

Figure 2.6: Typical RAO for heave

To calculate the potential field around the vessel, linear potential theory is used. This theory states that the total potential is the superposition of the potentials due to the radiation potentials of the 6 body motions, the incoming undisturbed wave and the diffracted wave:

$$\phi = \sum_{j=1}^{6} \phi_j + \phi_w + \phi_{dif} \tag{2.22}$$

The body, a vessel in this case, is described by panels, see Figure 2.7. Every panel has its contribution to the total forces and moments on the vessel. The smaller the panels, the more accurate results are found, but the higher computational costs. The required panel size is is usually determined based on the wave length of the shortest wave to be modelled.

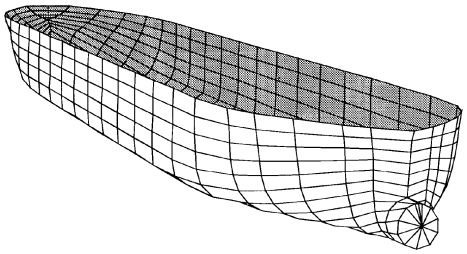

Figure 2.7: Panel distribution oil tanker (Journée and Massie, 2001)

So far, only regular waves have been discussed. However, wave signals mostly consists of irregular waves; a combination of multiple wave components with different frequencies and amplitudes. When this is the case, 2nd order effects can play a role. In irregular waves three components are considered important:

- Mean wave drift force; A mean displacement of the structure resulting from a constant load. Non-linear wave effects determine a new equilibrium and for moored ships, the mooring system plays a role here too.

- First order wave loads; As discussed earlier, the oscillating first order waves cause a harmonic response of the structure.

- Low-frequency wave drift forces; Non-linear elements in the waves cause oscillating displacements of the structure at very low frequencies. As ships tend to have a low natural frequency, large amplitudes can arise due to resonance.

In irregular wave fields, the so-called drift forces, which are 2nd order wave forces, start playing a role. The mean drift force is a constant force generated by interaction between the incoming wave and the wave reflected by the body. It is called a drift force as the body finds a new equilibrium position based on the mean drift forces. Therefore, the body "drifts" to a new preferred position.

The drift forces also contains a low frequency component, which can become dominant in shallow waters. Interaction between two harmonics with frequencies very close to each other creates a bound long wave, with a frequency equal to the difference frequency of the two components. Moored ship systems generally have a low natural frequency in the horizontal degrees of freedom: surge, sway and yaw, because of the relatively weak spring constants of the mooring lines. Moreover, there is little damping at the lower frequencies. As a consequence, this bound long wave, although small in amplitude, can provoke large motions of the moored vessel. In Figure 2.8, the principle of bound long waves is illustrated. Two components interacting creates a wave at a lower frequency.

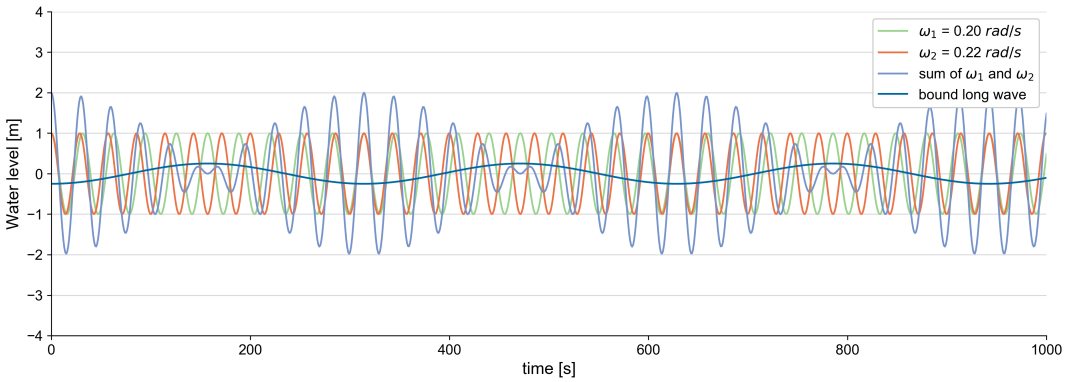

Figure 2.8: Two regular waves interacting

Table 2.2: Damping Matrix

	surge	**sway**	**heave**	**roll**	**pitch**	**yaw**
surge	B11	B12	B13	B14	B15	B16
sway	B21	B22	B23	B24	B25	B26
heave	B31	B32	B33	B34	B35	B36
roll	B41	B42	B43	B44	B45	B46
pitch	B51	B52	B53	B54	B55	B56
yaw	B61	B62	B63	B64	B65	B66

2.3.2. DIFFRAC

As ship diffraction model, DIFFRAC (MARIN, 2015) is used due to the availability as it is currently used for DMA's at RHDHV.

DIFFRAC, developed by MARIN, is a frequency domain simulation program to analyse body dynamics. It calculates the hydrodynamic properties of floating or moored bodies in both deep as shallow water. The hydrodynamics are based on potential theory, including diffracted waves and radiated waves. The most relevant output of DIFFRAC is:

- Added mass (a) and potential damping (b) coefficients (both 6x6 matrices)
- Wave forces and wave moments (amplitude and phase)
- Wave induced motions
- Water velocities over the hull of the body
- Pressure distribution over the hull of the body
- Mean and slowly varying wave drift forces

The main output of DIFFRAC consists of a HYD-file. This file contains the hydrodynamic database of the model. The first block of the HYD file provides more general information about the modelled vessel. The length (between perpendiculars), the beam and the draught are provided, as well as the radii of gyration in all three rotation directions: K_{xx}, K_{yy} and K_{zz}. Furthermore, mass [ton], displacement [m^3] and the modelled water depth [m] are given.

To account for viscous damping, usually 3% of the roll damping is assumed. DIFFRAC can calculate this and provide the value and the extra roll damping (b44) can be added in aNySIM. In the damping matrix, roll damping is defined as b44; It is the damping on the roll motion cause by the water displaced by the same roll motion, see Table 2.2

Consequently, the coordinates of the center of gravity are computed: x_g, y_g and z_g in [m]. Three more geometrical measures are given, the surface area at water level, A_{wl} and the metacentric heights in both lateral as in transversal direction. This GM value is an indicator for the stability of the ship in a certain direction. Physically seen, the GM_t is a lot lower than the GM_l, as the roll stability is much less than the pitch stability. A ship capsizes easier due to roll than to pitch motions. The GM value, which is a ship property and therefore provided, can be used to check the stiffness output parameters of DIFFRAC. The stiffness coefficients are defined according to the same definition as the damping coefficients in Table 2.2.

$$C44 = g \cdot m \cdot GMt \quad [Nm/rad] \tag{2.23}$$

$$C55 = g \cdot m \cdot GMl \quad [Nm/rad] \tag{2.24}$$

The previously mentioned bound long wave is also computed by DIFFRAC. For long crested wave modelling, a 2-dimensional Quadratic Transfer Function describes the 2nd order forces being a results of interaction between primary wave with a slightly different frequency. In 2D, there is only interaction when these waves

come from the exact same direction. When a short crested run is done, waves can come from multiple directions. In order to let those waves interact as well, the 4-dimensional Quadratic Transfer Function exists. This 4DQTF describes not only how waves with different frequencies interact, but also how waves with different directions interact. E.g. waves with 1° difference in direction are still likely to create a bound long wave, however waves with a difference of 90° are not. This is accounted for in the 4DQTF.

During this research, the 4DQTF functionality was not working correctly by a software error. Therefore, a workaround has been applied to account for directional interaction by binning components in directional bins of 10°. All components that fall into this bin create interaction between them for the bound long wave.

2.4. Ship Motion Modelling

The last model used in the DMA model chain is the ship motion model. Here, the purpose of the ship motion models is discussed and the chosen model, aNySIM, explained.

2.4.1. Ship Motion Models

For linear problems, a frequency domain analysis would be sufficient. RAO's calculated by DIFFRAC show the response of the vessel to the wave forcing. However, when non-linearities are added, a frequency domain analysis is insufficient. Such non-linearities are for example: Fenders, mooring lines, 2nd order wave loads, currents and wind. When these factors are of importance, a time domain simulation is required. As the objective of this research is to develop a method for modelling moored ship behaviour, a time domain analysis is needed and aNySIM is selected to be used for practical reasons. Alternative ship motion models used in previous research are QUAYSIM and MOORINGS.

The purpose of the time-domain ship motion model is to model the ships motions, so an operational assessment can be done related to the maximum motions, significant motions and fender and mooring line failure

2.4.2. aNySIM

As aNySIM is compatible with the hydrodynamic database created by DIFFRAC, it is used for the ship motion modelling.

aNySIM, a time domain ship motion model is, like DIFFRAC, developed by MARIN and therefore compatible with DIFFRAC (MARIN, 2018). In aNySIM, mooring equipment, like fenders and mooring lines can be implemented. Mooring lines connecting the bollards on the quay with the vessel, leading to reaction forces on the vessel, behave according to their user-defined but usually non-linear characteristics. The non-linearity is found in the force-elongation curves of the mooring lines and force-compression curve of the fenders. Furthermore, fenders can be added, which lead to non-linear reaction forces as well. Besides wave action, wind and current can be modelled as well, relevant for container vessels and open jetties respectively.

The XSFviewer software that comes with aNySIM, lets the user visualize the simulation. Fenders, mooring lines and the body are shown, just like the incoming waves can be seen. This is useful as a quality check to see if the dimensions and directions are correctly implemented. aNySIM is able to print all modelling parameters in two ways: The full time series, the value of the parameter at every time step and the statistics of the time series. This includes the maximum value, the minimum value, the mean and the standard deviation. The statistics are calculated from a user defined starting moment in order to let the body find its equilibrium position first. The standard output channels are the 6 degrees of motion; The translations surge, sway and heave and the rotations roll, pitch and yaw in the center of gravity of the body. Furthermore, sensors can implemented on any location of the body to track their positions. The forces and elongations of the mooring lines and compression of the fenders can be printed and a wave buoy can be installed on an user-defined location to check the wave signal.

3

Coupling and Verification for a Single Harmonic

In Figure 3.1, the structure of the proposed model chain is shown. In PHAROS, the port geometry is modelled and the wave boundary imposed. The local wave conditions, next to the quay are extracted and consequently imposed as wave field in aNySIM. DIFFRAC computes the forces, added mass and damping characteristics of the vessel. aNySIM extracts the necessary data from the HYD file, created by DIFFRAC, based on the incoming wave field.

The objective of this chapter is to develop the coupling method between the wave model and ship diffraction/motion models for a single harmonic. Therefore, a test model is created in PHAROS of which the analytical solution is known. This is done by excluding structure interaction, bottom friction and wave breaking.

In Chapter 4, it is evaluated for relatively simple wave conditions which elements to include in DIFFRAC and which in PHAROS and in Chapter 5, the wave field is made more complex by imposing a 2-dimensional wave spectrum.

The performance of the coupling method is assessed by comparing the results with the analytical solution. This means the boundary imposed in PHAROS is directly imposed in aNySIM instead of extracted from PHAROS. The wave field in PHAROS should be uniform in space and equal to the imposed boundary, as no diffraction, reflection, friction or wave breaking processes occur.

A monochromatic wave is imposed as boundary in the PHAROS model and for the reference model this monochromatic wave is directly imposed in aNySIM. The vessel is spatially fixed, and the comparison is made on the level of forces on the vessel. The last model in the chain, aNySIM, is used for extracting the wave forces. Because the non-linearities of the mooring system or left out in aNySIM, it is expected that the potential errors introduced by the coupling linearly translates to the forces.

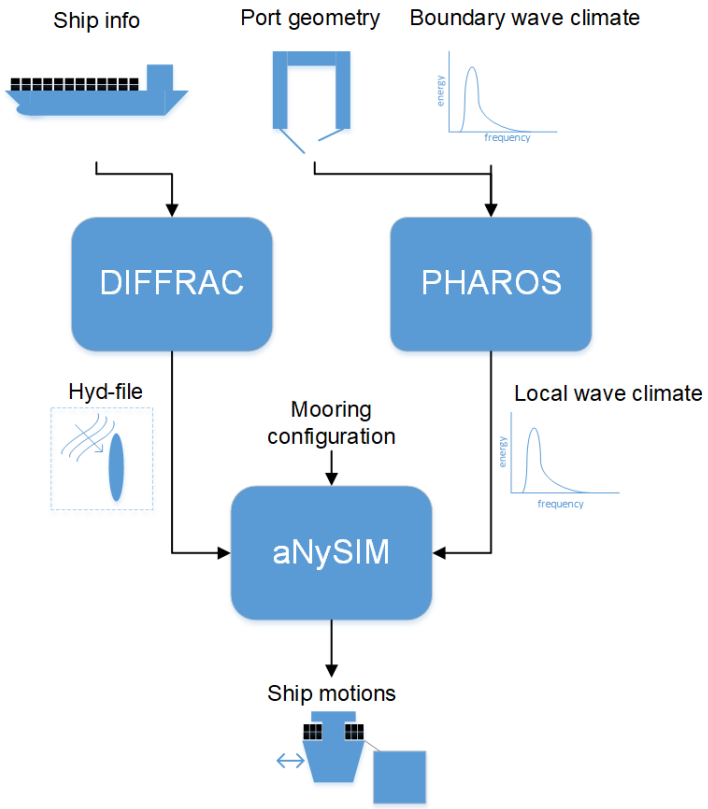

Figure 3.1: Proposed model chain of the coupling method. For the test case, the final comparison is made on level of forces on the vessel instead of ship motions.

3.1. Coupling method PHAROS - DIFFRAC/aNySIM

3.1.1. Comparing available coupling methods

PHAROS computes the local wave field at the mooring location based on the incoming wave imposed on the model boundary. The wave model computes the propagation of this wave in the model. As output, a total local wave height is given, consisting of the incoming wave and possible reflected components by structures.

To calculate the response of a moored vessel, it is insufficient to only know the total local wave height. It is also important to know the directions of the separate components, both incoming and reflected. In PHAROS, there is no standard output for these directions and therefore a method must be selected to extract this information.

Two different methods can be implemented to convert the PHAROS output to input of DIFFRAC. Their structures are presented in Figure 3.2.

1. The first one uses the r-DPRA tool, developed by Deltares (De Jong and Borsboom, 2012). The deterministic Rotational Directional Phase-Resolving Analysis tool uses a least-squares approach to distinguish between wave directions. Phase information is contained and therefore it is suitable for vessel motion calculations. The original goal of r-DPRA was detecting the main wave directions, but an extension was made where the directional spreading is based on the total spectral energy per frequency and resolution (Van Essen et al., 2013). The r-DPRA tool is based on the DPRA approach of Janssen and Van Dongeren (2001). DPRA, however, requires user intervention to determine the wave directions, while r-DPRA is based on optimization. r-DPRA can only be used when sufficient data points are available, like in numerical models. For field campaigns, with generally less data points, DPRA is more suitable. (De Jong and Borsboom, 2012)

2. The second method is a more direct coupling. As the output of PHAROS contains complex wave potentials at the cell locations, these can be directly imposed on the panels of the model vessel. By means of

interpolation, the complex wave potential can be found on the centers of the panels. DIFFRAC facilitates this method by letting the user define the wave potential per panel in separate files per frequency-direction combination. In DIFFRAC, the spatial variations in the wave field are then already included and time series of forces are exported and are used in aNySIM. Furthermore, the direction of the waves and their relative phases are automatically preserved by this method, since this information is contained in the spatial variation of the complex wave potentials.

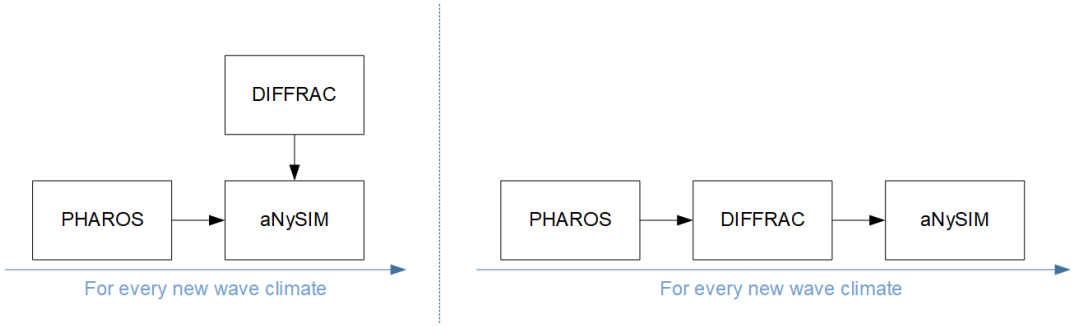

Figure 3.2: Model structures methods; Left the structure of the first method, using the r-DPRA tool, on the right the structure of second method, using the panel method

The second method preserves the spatial variation of the wave field along the hull of the vessel in a more accurate way than the first method using r-DPRA described above, but the coupling is more complex and the HYD file created by DIFFRAC is not applicable anymore, for every wave field a separate DIFFRAC run must be done. In order to be able to model different wave climates, the whole range of periods and directions must be included already in the HYD-file. It was chosen to continue with the r-DPRA method as this method has already been verified and is considered more practical. Moreover, Oude Vrielink (2016) showed that the panel method only slightly increases the accuracy. The computational time for DIFFRAC would be lower for one single run, however, for every wave climate a new DIFFRAC run must be done, therefore at the end leading to higher computational times.

3.1.2. Working of the r-DPRA tool

r-DPRA is applied by analysing data points, situated within a circle with in the center the desired target point. From a high resolution complex wave field, r-DPRA can isolate different main wave directions. Phase resolving wave models, e.g. PHAROS, require a minimum of 8 - 10 grid points per wave length (the shortest wave length) and therefore delivers a high number of grid points to be used by the r-DPRA. Per frequency, the wave parameters are determined. r-DPRA does not require predefined directions by the user, it uses predefined sets of analysis directions. These sets consist of an increasing number of directions equally distributed on the circle. For every set, the least-squared fit of wave height and phase are calculated per frequency. Rotating the set of directions gives the full 360° wave energy. In Figure 3.3, the principle of an increasing number of directions and the rotation principle are shown.

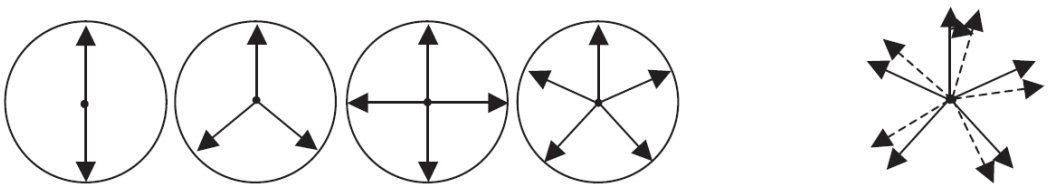

Figure 3.3: Rotation principle of the r-DPRA tool

With this r-DPRA tool, for every frequency, direction and wave height of an incoming wave component the local direction and wave height can be found, see Figure 3.4 as an example. Therefore, it is possible to construct a local 2D discretized energy density spectrum. For automation purposes, Deltares included a batch run extension for the r-DPRA tool. Without intervention, the batch mode can execute the r-DPRA analysis

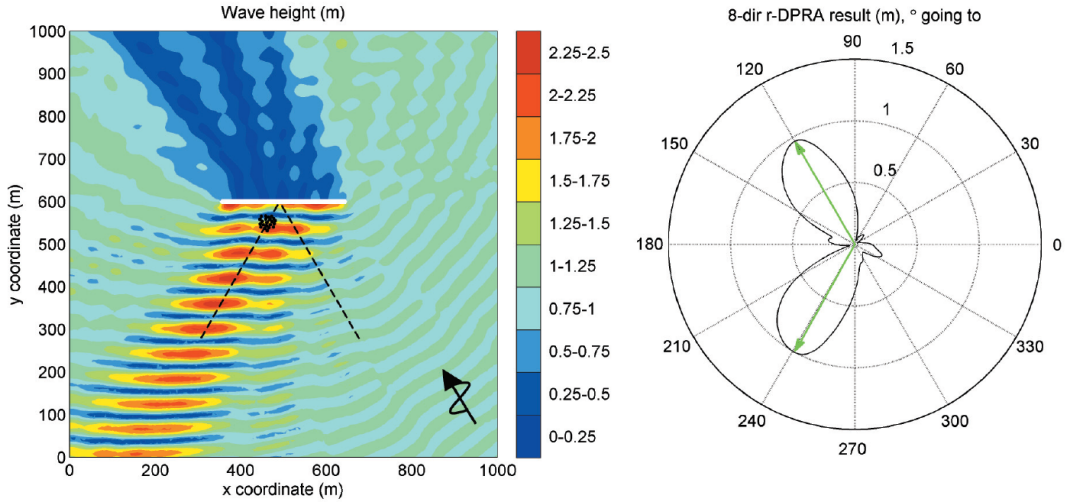

Figure 3.4: Example of the application of the r-DPRA tool. A single harmonic with a wave height of 1 m is imposed at the boundary and is reflected by the structure in the middle of the domain. In the right panel, the results of the analysis done by the r-DPRA tool are shown, both the incoming as the reflected components is found (De Jong and Borsboom, 2012).

for all directions and frequencies at once. The results are stored per run in JSON format, giving the measured wave heights and their directions. From these separate output files, a new spectrum can be constructed that represents the local wave conditions.

3.1.3. r-DPRA sensitivity

One important issue that is raised in this model, is the limitation of the r-DPRA tool. To determine the wave height and direction in one specified location, the r-DPRA tool takes a circle around that point and selects the grid points within that circle for the analysis. The diameter of this circle is recommended to be in between 0.1 and 0.3 times the local wave length. For a wave period of 15 seconds and a depth of 20 m, the local wave length equals around 220 m. The radius, therefore, is recommended to be chosen in between 22 m and 67 m. As a typical medium-sized bulk carrier has a beam of around 30 m, the distance between the quay and the ship is usually in the order of 2 or 3 m and therefore the midpoint lays about 15 m away from the quay.

However, if the depth does not vary much in front of the quay and the point that is selected is not too far from the quay, the found components approximate the conditions at the ships midpoint. The standing wave pattern does not influence the individual wave components found by r-DPRA, as the r-DPRA tool is especially designed to filter out the nodes and anti-nodes.

In the User Manual of the r-DPRA tool (Deltares, 2018), recommendations and limitations are given. As mentioned before, r-DPRA requires a constant depth along the circle to be analysed, a warning is raised if the difference in wave number exceeds the threshold value of 10 %. When applied correctly, the accuracy of the method is estimated to be in the order of 10%. Lastly, the r-DPRA tool must be used accurately around thin structures, as some points on the circle might be located on the other side of the structure, not influencing the real wave field on the desired location. It is recommended to have most of the circle within the PHAROS grid and desired wave field, to included as many grid points as possible in the analysis. The circle radius can be decreased to obtain results closer to the quay wall, however, Appendix A shows results become less accurate for too small radii.

To perform a r-DPRA analysis, a decision must be made on the location and the size of the radius. A sensitivity analysis is done for these parameters for the quay wall model, see Appendix A. It concludes that choosing a radius of 0.1 times the wave length can lead to non-existing wave components to be found and is therefore not recommended. Furthermore, large radii close to the quay are not favourable, as the number of data points is small, and for more complex geometries, some points may be located on the other side of a thin structure. The sensitivity analysis shows that the wave height of the incoming wave component can be off by 30%, if

parameters are selected poorly. Finally, a radius of 0.2 times the wavelength and a distance of 40 m from the quay wall is chosen. In that case, the radius size is sufficient and there is no cutoff of the circle.

3.2. Verification of coupling method for a single harmonic wave - PHAROS

For the most simple case, for which the coupling is set up, there are no structures involved and there is a uniform depth. A single monochromatic long crested wave is set as boundary condition. The r-DPRA batch mode is used to extract the local wave condition, although only one single harmonic should be found. This is done for consistency, as in a later stage, with spectral computations, the batch mode is required to extract the wave conditions from multiple runs. As this case is a theoretical situation to be compared with DIFFRAC only, bottom friction and wave breaking are disabled.

3.2.1. Grid, bathymetry and boundaries

The layout of the base case is visualised in Figure 3.5. The domain covers a square of 1,000 x 1,000 m, with in the center of the domain the midpoint of the ship. A uniform depth of 10 m is applied for the whole domain. Four boundaries are distinguished: North, East, South and West, with the waves entering from the Southern and Eastern boundaries (Figure 3.6). The coordinate system used is a Cartesian coordinate system expressed in the going-to directions of the waves, with counter-clockwise being the positive direction. For example, waves travelling northwards have a direction of 90°

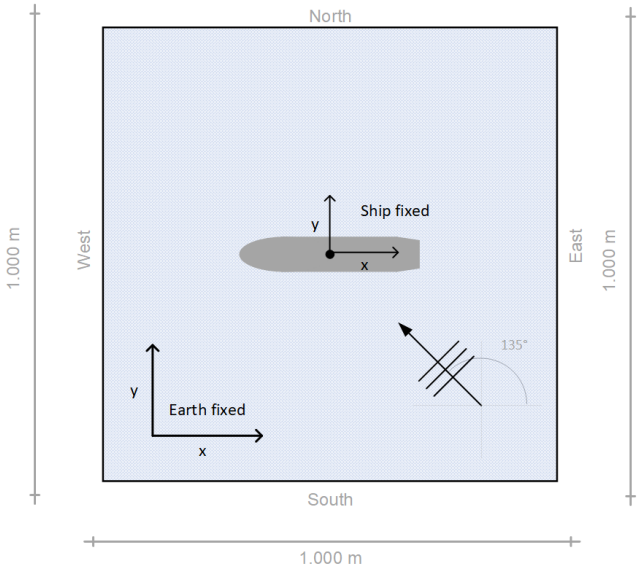

Figure 3.5: Schematized layout of the test case. A rectangular domain with the ship positioned in the middle. Angles of waves in going-to directions in Cartesian coordinate system

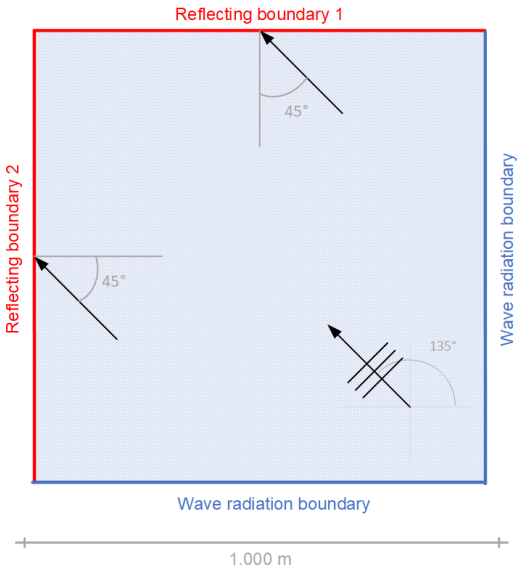

Figure 3.6: Definition of boundaries test case. Reflection coefficients are set to zero for wave with an incident wave angle of 45° with the normal of that boundary

To create the triangular grid, first the building points have to be placed. This is done by ACE/gredit, a build-in PHAROS tool. To automatically place the build points, PHAROS asks for the smallest wave period to be modelled and the number of cells per wave length. It is advised by the PHAROS manual to start with a coarse grid and later to refine it, to minimise manual adjustments. For short waves (T>6 s) PHAROS advises to have at least 8 cells per wave length. For the first coarse grid, this parameter is set to 4, with a minimum wave period of 10 s. After splitting cells, the number of cells per wave length becomes the minimum required 8 cells. In Figure 3.7, a close-up is shown of the used computational grid.

For this case, two kinds of boundaries are used: Reflective boundaries and wave radiation boundaries. The Southern and Eastern boundaries together form one wave radiation boundary on which the waves enter the domain. The Northern and Western boundaries are considered two separate boundaries, each with its own reflection coefficient, see Figure 3.6 for a schematized view of the boundaries.

As in the base case there are no structures involved, the reflection coefficients of both reflecting boundaries

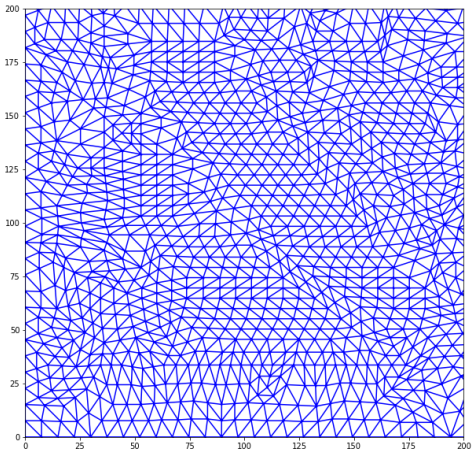

Figure 3.7: Close-up of the triangular computational grid used for the test case

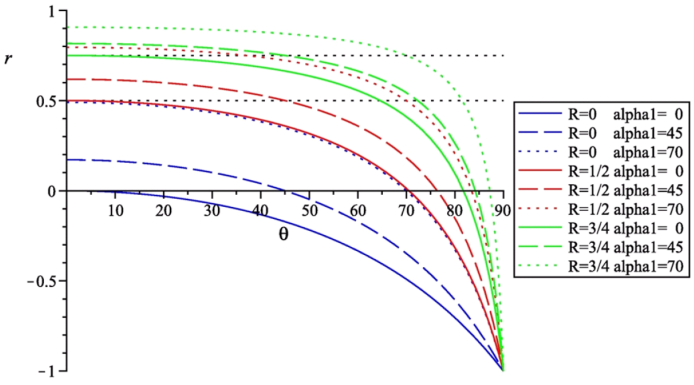

Figure 3.8: Reflection coefficients determined by PHAROS. Deviation from the expected value changes the reflection coefficient accordingly (Deltares, 2018)

must be set to zero. In PHAROS, the reflecting coefficient is set for a certain incoming wave direction. This means the incoming wave direction at the reflecting boundary must be known a priori. This is thus an implicit method, the solution is function of the solution itself. When the angle of incidence deviates from the expected angle of incidence, the reflection coefficient will change according to Figure 3.8 For this particular case, it can simply be determined that for both reflecting boundaries the incoming wave direction equals 45°, see Figure 3.6. For more complex geometries, iterations have to be done to compute the final solution. The r-DPRA tool was initially developed for this purpose.

3.2.2. Wave conditions

As discussed earlier, for this test case a monochromatic long crested wave is modelled. A wave period of 14 seconds is set, as this is a typical swell wave period. As PHAROS is a linear wave model, the simulations are run with a unit wave height, a wave of 1.0 m. For simplicity reasons, the incoming wave direction is chosen to be 135°, as for both reflecting boundaries this results in a 45° incoming wave angle, see Figure 3.6. A water level of +10 m is used to create a total water depth of 20 m, a reasonable depth for port basins. As bottom friction and wave breaking are disabled, this only influences the wave number.

3.2.3. Results PHAROS computation

For this base case, the PHAROS output is a single data file, is a combination of one wave period and one wave direction only. The result of this base run can be seen in Figure 3.9. The result is as expected; no reflections are noticed and the waves do not diffrac. To find the wave condition in the center of the domain, the r-DPRA tool is used. For single runs, the tool can be applied by using the MATLAB plugin GUI of r-DPRA that comes with PHAROS. The radius of the circle on which the considered points are located is recommended to be in between 0.1 and 0.3 times the wave length, preferred 0.2 as shown in Appendix A. The latter is used here. For the GUI option, the result is given as a polar diagram, see Figure 3.12. As can be seen in Figure 3.10, some reflection is found at the boundaries. The effect on the wave height is in the order of 0.5 - 1 percent. When the r-DPRA result is checked, it can be seen that the wave direction is found exactly, but the resolved wave height has been reduced to $H = 0.92m$, instead of $H = 1m$. This is a consequence of the r-DPRA tool, as in Figure 3.10, the PHAROS output shows a difference in wave height of less than 0.02 m. In Appendix A, an elaborate sensitivity analysis is done for the r-DRPA tool. When r-DPRA is run in batch mode, output files are generated in JSON format, see Figure 3.11.

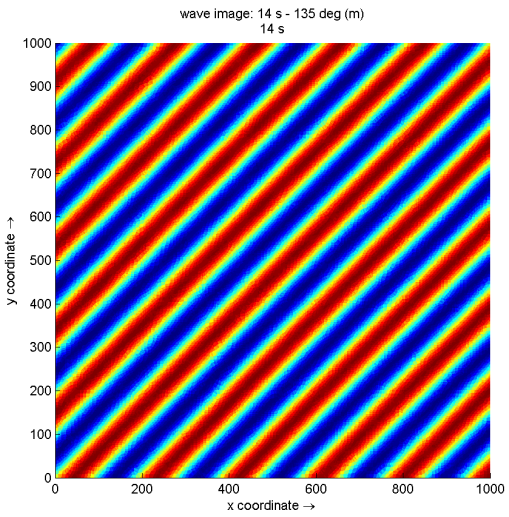

Figure 3.9: Wave image of base case run with T=14 s and wave direction 135°

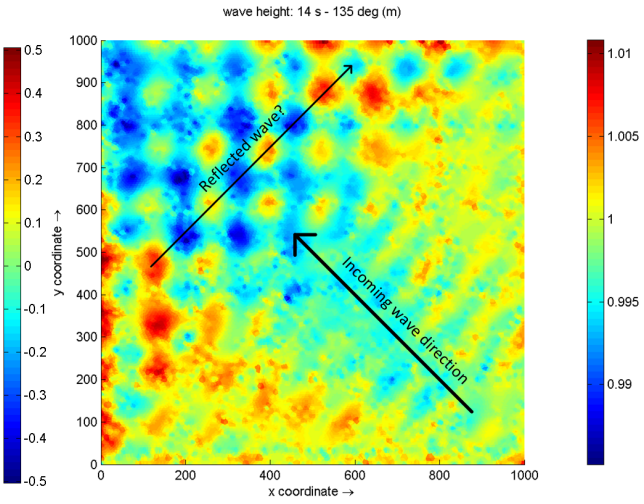

Figure 3.10: Wave height of base run with T=14s and wave direction 135°. Note the small scale of the colourbar, which has a range of only 0.03 m

```
"wave_heights": [
        {
                "cart": 135,
                "naut": 135,
                "H": 0.92,
                "perc": 100
        }
],
```

Figure 3.11: Batch mode output of r-DPRA analysis, in JSON-format

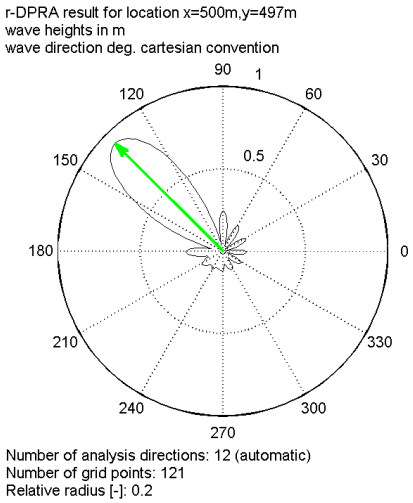

Figure 3.12: r-DPRA output of the base case; T = 14 s and a direction of 135°

3.3. Verification linearity in coupling DIFFRAC - aNySIM

In the previous section, the performance of the r-DPRA tool was tested for a single harmonic. An error was found in the wave height, and in this section the consequences of such an error are tested. Two checks are done:

1. A check to see if the hydrodynamic database and aNySIM are compatible. When taking on specific wave component that is stored in the database, the amplitude can be compared with the amplitude of the time series in aNySIM

2. A second check to see how the error introduced by the r-DPRA tool translates to forces on the ship.

3.3.1. DIFFRAC model

In this section, the setup of the DIFFRAC model is discussed. DIFFRAC creates a hydrodynamic database of the forces on the ship caused by waves, including added mass and damping in the frequency domain. This hydrodynamic database (HYD-file) is used by aNySIM to model the ship motions in time domain.
The first step in setting up the DIFFRAC model is to select the ship to be modelled. As this is an academic test case, a practical choice is made here. The starting point of generating a hull mesh is a linesplan of the

ship, this linesplan can then be scaled in order to accurately model a specific ship. To prevent any errors in scaling, an unscaled linesplan is used of a bulk carrier. Linesplans are files that describe the hull of a vessel by providing the coordinates of the hull points for multiple cross-sections.

One medium-sized bulk carrier, with a length between perpendiculars of 187 m, is selected to be modelled for this academic test case. The vessel is not scaled to avoid an unnecessary introduction of errors. For case studies or real DMA's, however, this scaling must be done in order to recreate the measured or required vessel. The characteristics of the selected vessel are presented in Table 3.1, its body plan is shown in Figure 3.13 and the 3D mesh of the hull in Figure 3.14.

Table 3.1: Characteristics of the bulk carrier selected to be used for the academic test case.

		Bulk Carrier	
Length between perpendiculars	Lpp	187.0	m
Beam	B	29.0	m
Draught	T	10.95	m
Depth	D	13.0	m
Displacement	displ.	47,032	m^3
length /width ratio	L/B	6.45	-
width / draught ratio	B/T	2.65	-
blocking coefficient	Cb	0.79	-

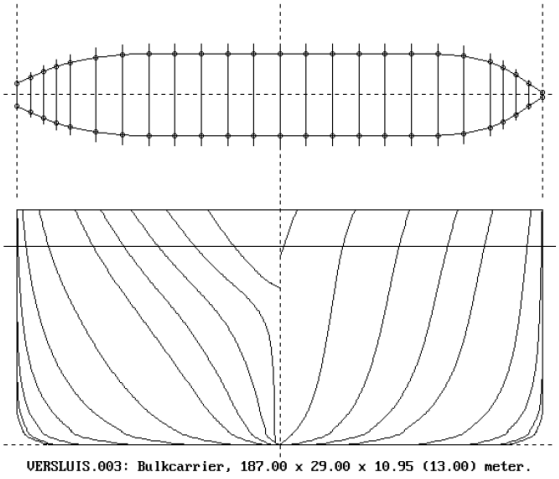

Figure 3.13: Bodyplan of the selected bulk carrier, used for the academic test case

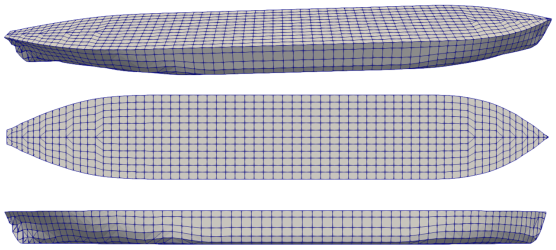

Figure 3.14: 3D mesh grid of the hull of the modelled bulk carrier

Other characteristics of the vessel must be estimated. These estimations are done based on Journée and Massie (2001) and are presented in Table 3.2. The radii of gyration are $K_{xx} = 0.3 \cdot B$ and $K_{yy} = 0.25 \cdot L$. The GM_t value is estimated by $GM_t = 0.12 \cdot B$. The KG follows from the GM_t and ship characteristics. The displacement is calculated based on the hull geometry.

For the single harmonic base case, the frequency range for which the added mass and damping are calculated is 0.1 rad/s to 1 rad/s with steps of 0.05 rad/s, which equals waves with periods ranging from 3 s to 31 s. The directional resolution is chosen to be 10°, covering a full 360° circle. When wave components are found within these steps, values are interpolated in aNySIM. These parameters influence the computational time needed for a DIFFRAC run. Important is to have a frequency resolution that is fine enough to distinguish every single wave component of a PHAROS run. It is inefficient to have DIFFRAC run for a very fine resolution but PHAROS for a coarse resolution and the other way around as the accuracy is determined by the coarsest resolution. The option to add either a basin wall or a quay wall is disabled, as for this case no structures are involved.

Table 3.2: Characteristics vessel modelled in DIFFRAC for the test case, Versluis003

		Versluis003	
Keel to CoG	KG	8.5	m
CoG to Metacentric height, transversal	GMt	3.44	m
CoG to Metacentric height, longitudinal	GMl	226.65	m
Radius of gyration	kxx	7.25	m
Radius of gyration	kyy	56.1	m
Panel size	-	2.7	m
Water depth	d	20.0	m
Mass	m	48,207	t

3.3.2. aNySIM model

Here, the setup of the last numerical model in the chain is described. aNySIM is a time domain ship motion simulation program, that is needed if non-linearities are introduced by the mooring arrangement, so that it cannot be solved in the frequency domain.

aNySIM creates a 2-dimensional wave field based on the discreet components that are imposed as incoming waves. By assigning random phases and summing all components, the conversion is made from the frequency domain to the time domain. .The hydrodynamic database made by DIFFRAC is then called to calculate the motions of the vessel and the forces in the fenders and mooring lines, by solving the mass-spring equations with the right mass and damping coefficients.

For the base case, no structures are involved and no nonlinear mooring equipment is included in the model. As the incoming wave is a single regular harmonic, this case can be considered a linear problem. Therefore, the comparison is done on the level of wave forces.

3.3.3. Verification compatibility and linearity

First, the compatibility is checked by looking at the amplitude of the forces from the aNySIM output and comparing it with the amplitudes in the hydrodynamic database created by DIFFRAC. To check this, the ship is fixed in space, no motions allowed and the forces acting on the ship are printed. A single harmonic that exactly matches one of the discreet wave frequencies stored in the hydrodynamic database is set as forcing. In this case, $\omega = 0.5 rad/s$ is chosen, which equals a wave period of $T = 12.57s$ and an incoming wave direction of 180°, bow-on waves as this a component exactly defined in the hydrodynamic database. The wave amplitude is set to 1 m, as DIFFRAC calculates the response for a unit wave. The phase of the incoming wave is unknown and is assigned randomly by aNySIM, the amplitude of the force is not influenced by this random phase.

From the statistics file created by aNySIM, the minimum and maximum values of the force in surge direction can be retrieved. These are then related to the amplitude of the force. This amplitude must be equal to the force amplitude for surge calculated by DIFFRAC and stored in the hydrodynamic database. A visual inspection is done to check the output signal, see Figure 3.15, and the amplitudes are compared. For all 6 degrees of freedom, the forces or moments are exactly equal to the values in the hydrodynamic database.

In Figure 3.15, also the force in surge direction of the aNySIM run with a wave with a 8% lower amplitude is shown. It can be seen in Table 3.3 that the 8% error in the wave height linearly translates to an 8% error in force amplitude.

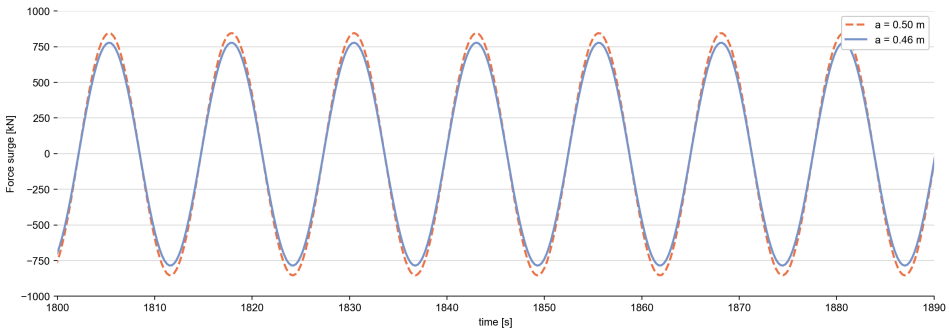

Figure 3.15: Time series of surge force response for the theoretical a = 0.5 m and the amplitude with an amplitude error of 0.04 m

Table 3.3: Modelled force and moment amplitudes test case single harmonic

Motion	**Amplitude**		**Difference**
	$a = 0.50m$	$a = 0.46m$	
Force surge [N]	8.50×10^5	7.82×10^5	8 %
Force sway [N]	6.83×10^1	6.28×10^1	8 %
Force heave [N]	1.16×10^6	1.06×10^6	8 %
Moment roll [Nm]	2.07×10^2	1.91×10^2	8 %
Moment pitch [Nm]	3.54×10^8	3.26×10^8	8 %
Moment yaw [Nm]	8.63×10^3	7.94×10^3	8 %

3.4. Conclusion Coupling Method

The two existing methods for retrieving wave components while conserving their directions were discussed. For practical reasons and for the sake of applicability, the r-DPRA tool method was selected to be implemented as coupling method between PHAROS and aNySIM and DIFFRAC. This r-DPRA tool introduces an error in wave height, direction and number of components that has been evaluated in Appendix A.

As can be expected because of linearity, an 8 % error in wave height leads to a 8 % error in the amplitude of force on the ship. It must be noted that this is with the ship in a fixed position, no motions allowed. Therefore, only the incoming and diffracted waves are tested, not the radiated waves. It can be concluded that for a single regular harmonic wave, without any structures involved, an error is introduced by the r-DPRA that linearly translates to the wave forces acting on the ship.

It was found that the magnitude of the error highly depends on the location of the r-DRPR analysis. For the analysed position, the error was 8 %, while for several other locations close to the original location the error was 1 % to 3 %. According to the User Manual of the r-DPRA tool, the magnitude of the error can be in the order of 10%. In Appendix A, a more elaborate sensitivity analysis has been done for the r-DPRA tool. This analysis concluded that the target point should be far enough from structures to prevent cut-off of the circle of data points and the already recommended by Deltares diameter of 0.2 times the local wave length leads to the best results (Deltares, 2018).

In the next chapter, the influence of a quay wall is assessed. In ports, vessel can be moored directly next to quay walls and therefore the interaction between the quay wall and the vessel can be of importance.

4

Assessing Influence Quay Wall Modelling

In this chapter, the most efficient way of modelling a quay wall is evaluated. Modelling a quay wall is possible in DIFFRAC without increasing the computational time significantly. However, the quay wall is already modelled in PHAROS and therefore the r-DPRA tool also finds reflected components. Two ways of modelling the quay wall are assessed, first on the level of primary waves and second on the added mass and damping coefficients. Finally, a decision is made on how to efficiently incorporate the quay wall in the coupling method.

4.1. Approach

The same test case as in Chapter 3 is used, with the ship being positioned next to a quay wall, in this case the northern reflecting boundary. It is tested how the quay can be taken into account in the most accurate and efficient way. For this verification, two model set-ups are configured:

1. In the first set-up (upper row, Figure 4.1), the vessel is moored next to a full reflecting quay wall. This quay wall is modelled in PHAROS and after using the r-DPRA tool, also reflected components are found. In this method, DIFFRAC does not model a quay wall, only the body of the vessel is modelled and its response is stored in the HYD-file. All components found by the r-DPRA tool are imposed in aNySIM, therefore including the reflected components.

2. In the second set-up (lower row, Figure 4.1), the quay wall is still modelled in PHAROS, however, the reflected components found by the r-DPRA tool are filtered out. The quay wall is then modelled by DIFFRAC and forces, added mass and damping that are stored in the HYD-file include the presence of a quay wall.

The incoming wave that is modelled is equal to the incoming wave used in the test model of Chapter 3, an incoming angle of 45°.

The schematic model domain is shown in Figure 4.2. The incoming wave boundaries are still the east and south borders, while the north and west boundaries stay reflective boundaries. The difference is, that for the incident wave direction of 45°, the reflection coefficient of the northern boundary is set to 100%. This boundary represents the solid quay wall, and therefore waves should be fully reflected.

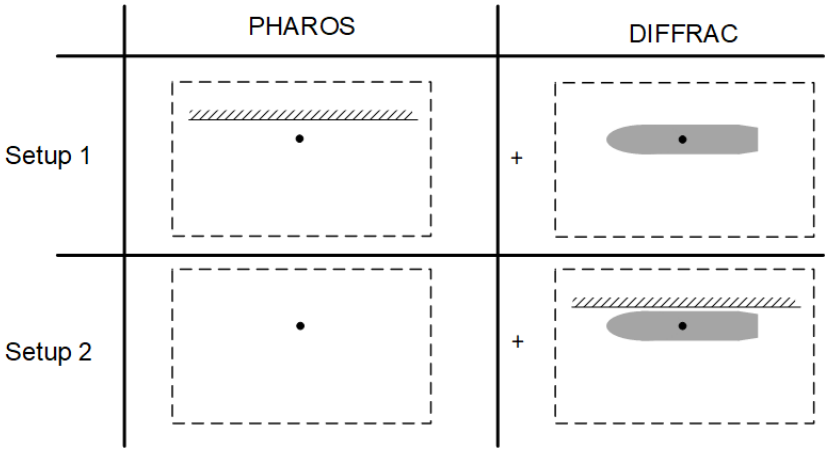

Figure 4.1: Approach to assess the modelling of a quay wall. In setup 1, the quay is modelled in PHAROS only, while in setup 2 the quay is modelled in DIFFRAC

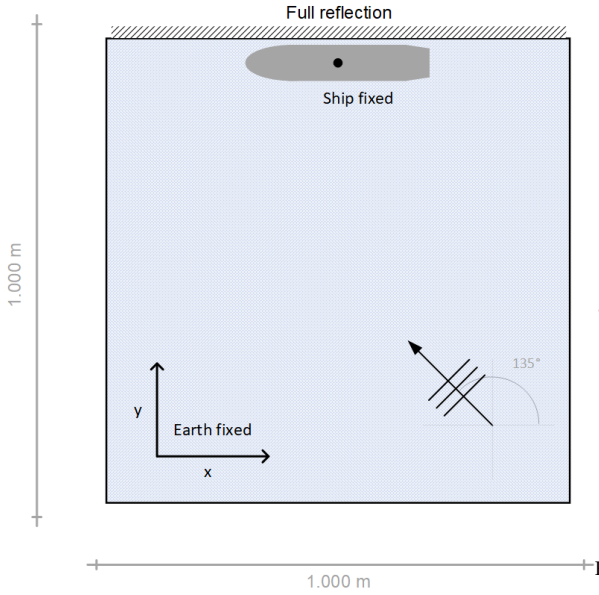

Figure 4.2: Layout of the model domain with quay wall at the north boundary. Ship is positions next the quay wall.

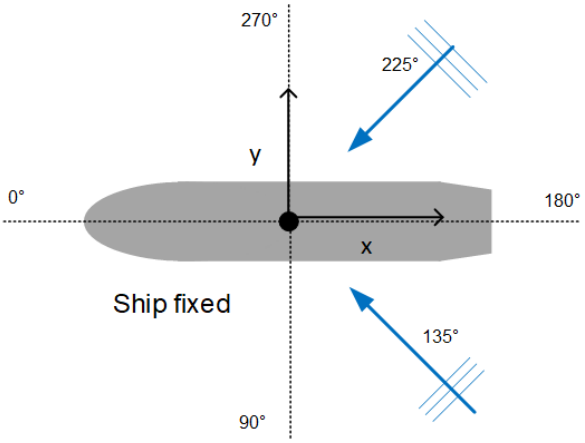

Figure 4.3: Directions of incoming and reflected wave

4.2. Primary wave forcing

In this section, the effect of modelling a quay wall on the incoming and reflected wave field is discussed.

For the first setup, two single harmonics with a wave period of 15 s are imposed in aNySIM as wave climate that represent the incoming wave and the reflected wave found by the r-DPRA analysis of the PHAROS computation, see Figure 4.3. As both wave periods are equal, the phase angle between the incoming and reflected component is expected to greatly influence the resultant wave field. This sensitivity is examined.

The comparison is made with the values found for the 2nd setup in which the quay wall is modelled in DIFFRAC, and thus where the phase angle between the incoming and reflected wave is modelled accurately. The theoretical wave heights and directions are used in order to isolate the error imposed by the unknown phase angle. In Tables 4.1 and 4.2, the used parameters for setup 1 and 2 respectively are shown.

As can be seen from Table 4.3, the resultant force amplitudes are greatly dependent on the phase angle between the incoming and reflected wave. This causes problems when modelling single harmonic wave bound-

Table 4.1: aNySIM parameters used for setup 1

Parameter	Incoming	Reflected
wave period	15 s	15 s
amplitude	0.50 m	0.50 m
direction	135°	225°
phase	random	variable

Table 4.2: aNySIM parameters used for setup 2

Parameter	Incoming
wave period	15 s
amplitude	0.50 m
direction	135°
phase	random

Table 4.3: Force and moment amplitudes test case for different phase angles between incoming and reflected wave.

Motion	Phase angle		
	0°	90°	180°
Force surge [N]	7%	-24%	-100%
Force sway [N]	3%	240%	381%
Force heave [N]	23%	-13%	-80%
Moment roll [Nm]	10%	249%	380%
Moment pitch [Nm]	5%	-27%	-93%
Moment yaw [Nm]	-73%	609%	909%

aries, as the phases are unknown and the resultant force and moments could even double or cancel out each other.

However, when modelling a full wave spectrum, the phase dependency is expected to be reduced. If the spectrum is discretized in a sufficient number of wave components and random phases are assigned to the different components, the real wave field is approximated more accurately as errors cancel out each other. Comparing the results from setup 2 that includes the quay in DIFFRAC with setup 1 that does not include the quay wall in DIFFRAC, not one single phase angle approximates the reference model accurately. There is no general phase angle between the incoming and reflected waves. Therefore, it cannot be determined what phase angle the two harmonics have with respect to each other.

This phase angle difference between the incoming and the reflected wave plays a role when the quay wall is not included in DIFFRAC, the first setup. In the second setup, with the quay wall modelled in DIFFRAC, the phase angle is preserved, as the reflection is modelled in DIFFRAC and that information is saved. In both setups, the phase angle of the incoming wave is unknown, but the phase angle of the reflected wave with respect to the incoming wave is known for the setup that includes a quay wall in DIFFRAC.

Based on this analysis of the primary waves, it is recommended to use the second setup and model the quay wall in DIFFRAC and consequently filter out the reflected wave components extracted by the r-DPRA tool before imposing the list of components in aNySIM.

4.3. Added mass and damping

Then, the effects of including a quay wall on radiated waves, thus added mass and damping, are discussed.

When modelling a quay wall in DIFFRAC, a numerical damping lid is added in the gap between the quay and the vessel and a typical value of 30% damping is applied. This is done because viscous effects are not accounted for in DIFFRAC and unrealistic high wave elevations would be found if this damping lid at the free surface would not be included (MARIN, 2015).

As an example, the difference in additional damping in sway direction due to sway motion (B22) is shown in Figure 4.4. When a vessel is pushed in sway direction, the water body on the going-to side of the vessel has to flow away in order to create space for the vessel. This flow is limited to the area of which it must flow through. In a simplified 2D case, there is much more area to flow through without a quay wall than there is with the quay wall. This limited flow area due to the quay wall causes extra resistance or damping to the sway motion of the vessel.

In Figure 4.5, this effect is confirmed by the added damping coefficients stored in the hydrodynamic databases. For the lower frequencies, there is hardly any damping, as in both cases the water has sufficient time to flow away. For the higher frequencies, the oscillation is too fast and there is no time for the water flow away. This holds for both the quay wall situation and the open water situation. In the range of the intermediate frequencies, the effect of the quay wall is visible. It can be seen that the damping coefficient can reach over 250,000 $kN/(m/s)$, while in the situation of no quay wall it reaches about 30,000 $kN/(m/s)$, a factor in the order of 10 difference.

For the added mass, the difference can be seen in Figure 4.6. Not only the magnitude of the added mass becomes higher, for a certain range of frequencies the added mass becomes negative. This can happen when free-surface effects are important (Mciver and Evans, 1984).

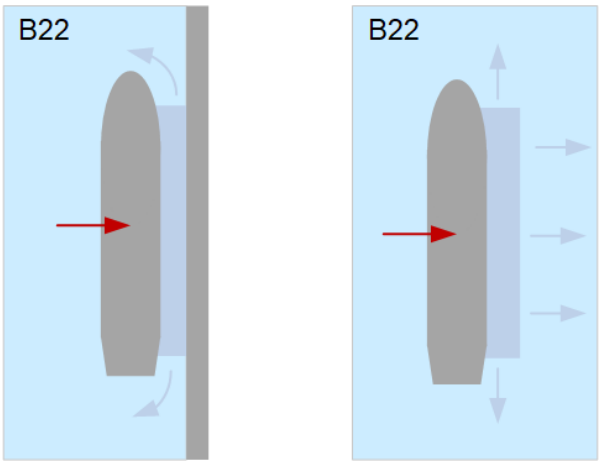

Figure 4.4: Added damping by quay wall principle

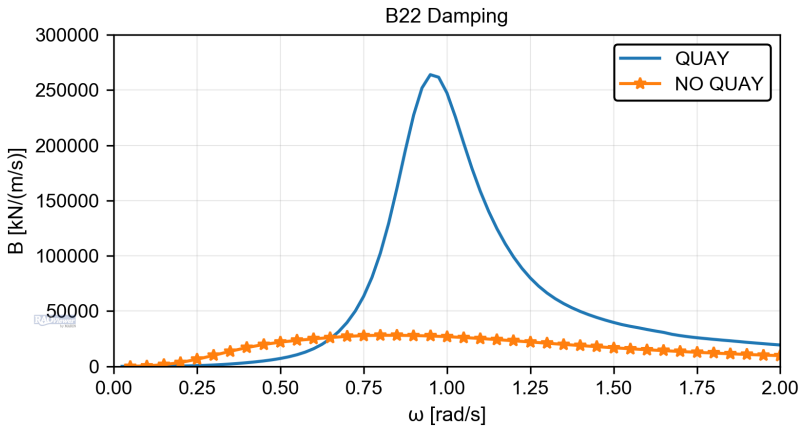

Figure 4.5: Damping in sway direction; B22 coefficient with and without quay wall modelled in DIFFRAC

In DIFFRAC, it is also possible to include structures like breakwaters as separate bodies. They are assigned a relatively large mass and thus become position fixed. The computational times are higher, as two bodies with their own grids must be modelled. Moreover, a sloped bottom can be modelled by panels as well, increasing the computational time. However, including a quay wall only is simple, as this is not modelled as separate body. Computational times do not increase significantly by including only one quay wall directly adjacent to the ship.

In PHAROS, the vessel itself is not modelled, only the undisturbed wave field at the location were the vessel is moored. Because the vessel is not included in PHAROS, it is not possible to include vessel-quay wall interac-

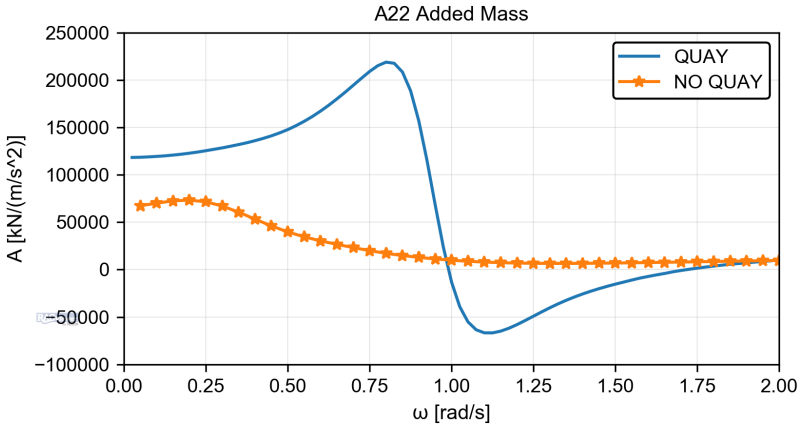

Figure 4.6: Added mass in sway direction; A22 coefficient with and without quay wall modelled in DIFFRAC

tion effects into account in the wave model PHAROS.

In PHAROS, all the structures are already included. Therefore, when directly using the results of the complete wave field as computed by PHAROS, the structures should not be modelled in DIFFRAC. The disadvantage of not modelling the structures in DIFFRAC is that the effect of reflected radiated waves is not taken into account. However, as their wave heights are relatively small and the distance over which the waves travel is large, this aspect can be considered of minor importance. In Figures 4.7 and 4.8, the principles of the reflected radiated waves is illustrated. Due to the spreading of energy following from the outward propagation of ring waves from a point source (the ship), the reflected wave heights become smaller and if the structure is far away enough, the waves become negligible.

The same holds for the diffracted waves, the effect of diffracted waves being reflected by port infrastructure and travelling back towards the ship is not taken into account in DIFFRAC. The DIFFRAC theory is based on the so-called radiation condition: It states that wave disturbances (radiated and diffracted waves) decay far away from the bodies, which holds for the infinite boundaries (MARIN, 2015).

It is more accurate to have all structures and the bottom slope in DIFFRAC, however, the added panels lead to much higher computational times and therefore, it is not favourable to included them in DIFFRAC. Especially for port layouts, it is not feasible to model all the port related infrastructure in DIFFRAC.

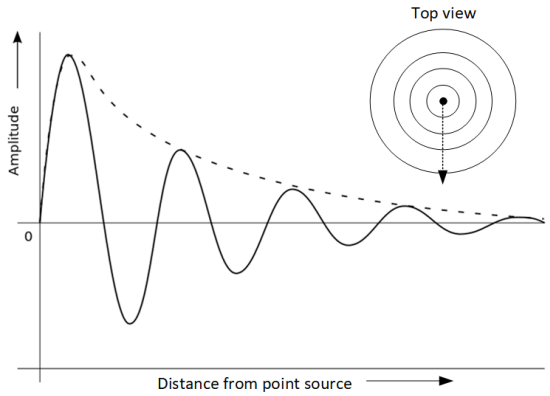

Figure 4.7: Spreading of energy due to outward propagation of ring waves from a point source decreases the wave height

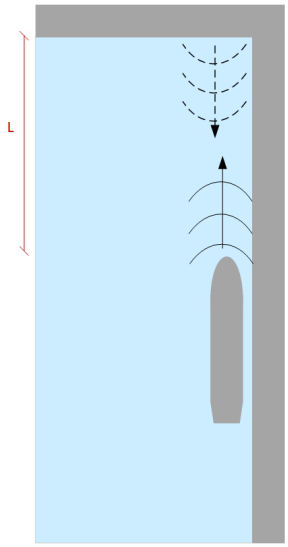

Figure 4.8: Radiated wave being reflected by port infrastructure and travelling back towards the ship.

4.4. Conclusion Quay Wall Modelling

In the previous sections, the effect of including a quay wall in the DIFFRAC has been investigated. The conclusion that can be drawn is that the quay wall should be included in the hydrodynamic database created by DIFFRAC, setup 2 of Figure 4.1, based on the following reasons:

- The forces on the vessel are highly depended on the phase angles between the incoming and reflected waves. As these are unknown after extracting components with the r-DPRA tool, there is an error introduced by assuming random phase angles that greatly influences the resultant vessel forcing. When modelling the quay wall in DIFFRAC, this phase angle between the incoming and reflected wave is preserved.
- The effect on the added mass and damping of the vessel is significant and only included in the case where the quay wall is modelled in DIFFRAC and included in the HYD file.
- The objective of the model chain is to reduce computational times without increasing the manual work to be done and therefore aiming for simplicity. As introducing a quay wall is simple and the computational times do not increase significantly, including it does not compromise the objective of the model chain. By adding a quay wall in DIFFRAC however, the wave components reflected off the quay wall need to be filtered out the PHAROS results to avoid erroneous "double counting" of wave components. This filter step is a relatively straightforward postprocessing step of the PHAROS results, and therefore does not add much complexity to the method
- The other structures apart from the quay wall the vessel is moored alongside do not need to be included in DIFFRAC, as the computational costs increase significantly and the effect on the vessel motion is negligible. That is because other structures need their own mesh grid, this increases the computational time.

5

Wave field coupling method

In real case studies, the incoming wave climate consists of more than just one single regular harmonic wave, as discussed in Chapters 3 and 4. The concept of a wave spectrum is then used to describe the sea-state, see Figure 5.1 and 5.2.

"*If the waves are not too steep and the water is not too shallow, the physically and statistically most meaningful phase-averaged characteristic of the waves is the wave spectrum. This spectrum is based on the notion that the profile of ocean waves can be seen as the superposition of very many propagating harmonic waves, each with its own amplitude, frequency, wave length, direction and phase (the random-phase/amplitude model).*" (Holthuijsen, 2007)

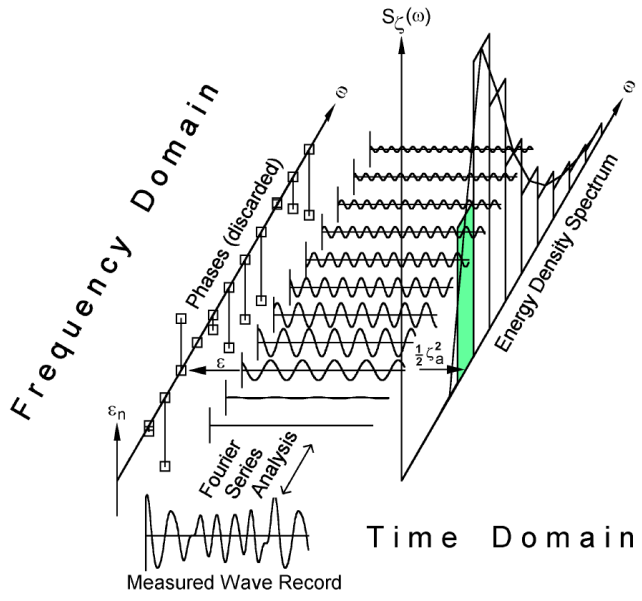

Figure 5.1: The principle of a wave spectrum (Journée and Massie, 2001)

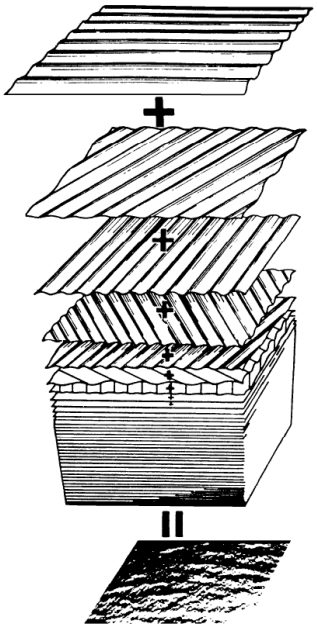

Figure 5.2: Sea state as a summation of different harmonics (Journée and Massie, 2001)

The above mentioned wave spectrum principle also holds for a 2-dimensional case. The energy is not only distributed in frequency domain, but also in the directional domain. In Figure 5.3, a 2D wave spectrum is shown. Its projections on the axes show the distributions in frequency and direction domain.

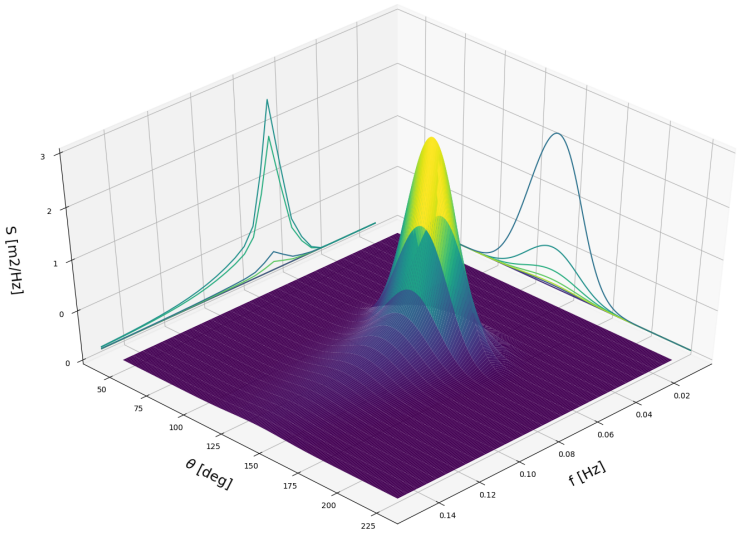

Figure 5.3: 2D Wave Spectrum

5.1. PHAROS

The structure of a PHAROS model, shown in Figure 5.4, consists of the following steps:

- The first step is to define the wave spectrum at the boundary. This consists of both physical parameters (wave height, wave period, direction) as artificial parameters that describe the shape of the 2D spectrum (peak enhancement factor, directional spreading factor).
- Then, the spectrum must be discretized into separate wave components each with their own frequency and direction. This is needed as PHAROS solves the wave field in frequency domain.
- Third, the PHAROS wave field computation is done. Here, PHAROS calculates the field wave for the full domain. This is done by modelling every component separately. The final wave field is a result of the weighted sum of all individual runs.
- Finally, the r-DPRA tool is applied to extract individual components and their directions from the seperate PHAROS runs at the desired location. The final output of the r-DPRA tool is a list with for every separate run the found components, containing both wave height as direction.

When modelling a wave spectrum, PHAROS automatically assumes a JONSWAP wave spectrum. For case studies, either other wave model output, e.g. SWAN, or measured wave buoy statistics are taken as input for the PHAROS runs. For the La Coruña case study, in Chapter 6, the available hourly wave buoy statistics are:

- Significant wave height [m]
- Maximum significant wave height [m]
- Mean wave direction [degrees]
- Peak wave direction [degrees]
- Mean wave period [s]
- Peak wave period [s]

From these statistics, the significant wave height, peak wave direction and peak wave period are used for the PHAROS wave modelling. As PHAROS is a frequency domain wave model, the spectrum is divided into discreet wave frequencies. For every frequency, a separate run is done by PHAROS. All runs are executed with a wave height of 1.0 m for this test case. To represent the spectrum, weight factors should be appointed to each frequency, as every frequency has its own energy. The energy distribution over the frequencies is

done based on the equal weight distribution. This distribution aims to assign every component with roughly the same weight factor. The high energy around the peak is not represented by a high weight factor, it is represented by a higher resolution around the peak.

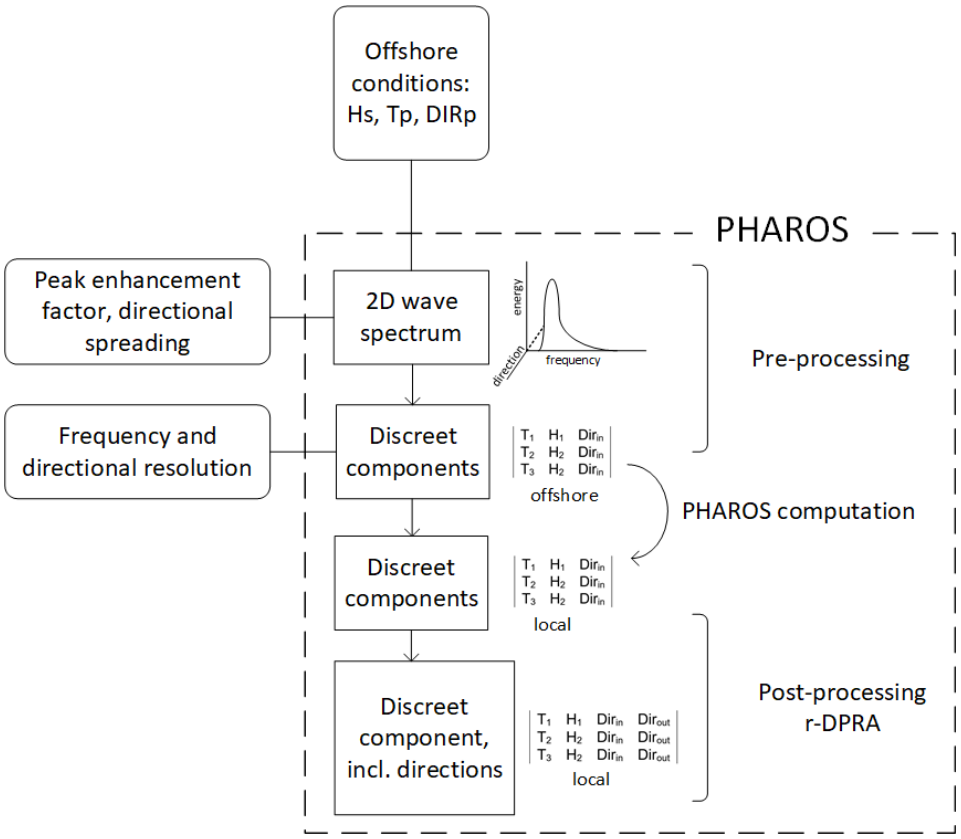

Figure 5.4: PHAROS flow scheme

5.1.1. Discretization Wave Components

The goal of the discretization is to represent the spectrum at sufficient resolution, without the need to run a large number of computations. Therefore, the resolution is a trade-off between accuracy and computational time. The spectrum can be presented in two ways: The spectrum itself and the cumulative spectrum. To select the discreet wave periods, PHAROS recommends taking, from the cumulative spectrum, the periods at which the cumulative energy is 10%, 30%, 50%, 70% and 90% of the total energy. In order to increase the resolution, the 20%, 40%, 60% and 80% wave periods are used as well. In Figure 5.5, the cumulative JONSWAP is shown, including as an example the 70% wave period.

In Figures 5.6 and 5.7, the JONSWAP spectrum is drawn. First with the selected discreet wave periods and next to it with the weight factors plotted at those frequencies. It can be seen that all the weight factors weigh around 10% with the outer wave periods having a slightly higher weight factor. This is due to the low resolution at those wave periods. The resultant wave heights that are computed by PHAROS must be multiplied accordingly by their weight factors in order to find the wave height contribution of the component to the local wave field.

Besides discretization in frequency domain, there is also the discretization in the spatial (angular) domain. When no directional spreading is assumed, all individual wave components have the same direction. However usually there is a certain spreading in directions. A peak direction can be distinguished while the other wave directions are close to the peak direction. When this is the case, a 2-dimensional wave spectrum is required, as the energy is not only spread over different frequencies, it is also over different wave directions.

To find the weight factor per component, the frequency weight factors must be multiplied by the directional

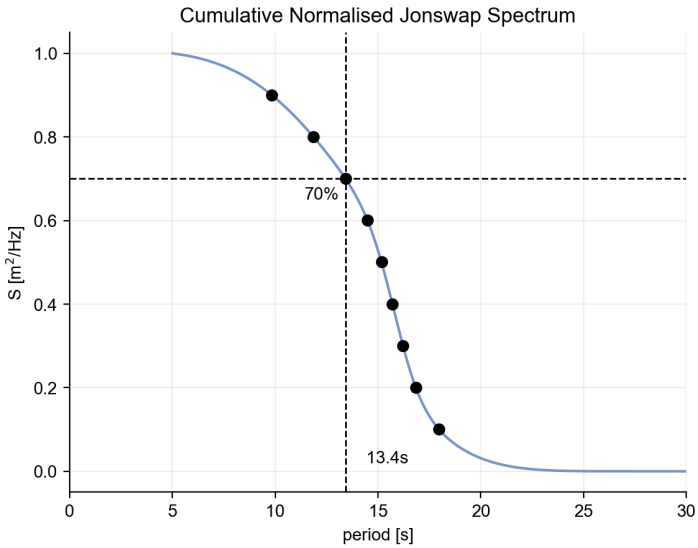

Figure 5.5: Cumulative normalised JONSWAP spectrum of the test case with $\gamma = 3.3$

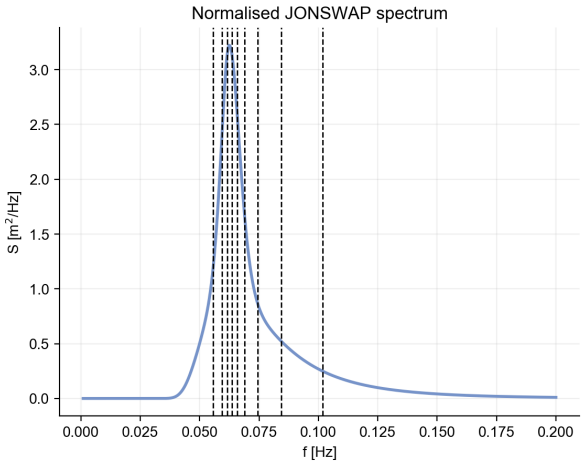

Figure 5.6: JONSWAP spectrum of the test case with selected discreet wave periods

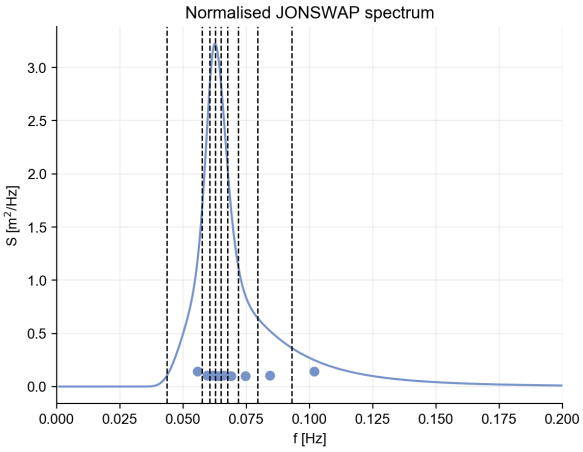

Figure 5.7: JONSWAP spectrum of the test case with weight factors and the frequency limits that are covered by the weight factors

weight factor. This results in a weight factor matrix of size $m * n$ with m being the number of directions and n the number of frequencies. The resultant wave height of a run must be multiplied with the components weight factor. The significant wave height is imposed as wave height of the component in PHAROS and the weight factors are normalised. For the verification process, the runs are done with a wave height of 1.0 m. In Figures 5.9 and 5.8, it can be seen that the peak direction contains the most energy and the outer frequencies contain slightly more energy than the other frequencies, as explained in the previous section. The weight factor matrix is used to assign weights to the components imposed in PHAROS after extracting the local wave components by means of the r-DPRA tool.

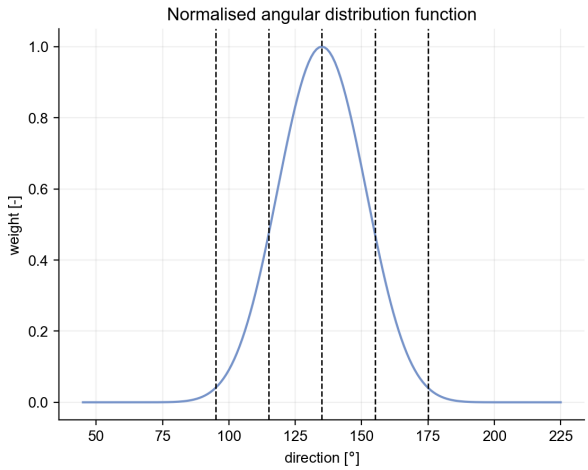

Figure 5.8: Directional spreading test case, discreet wave directions

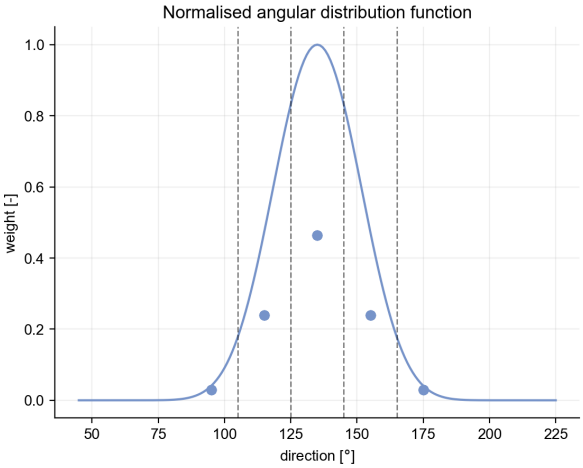

Figure 5.9: Directional spreading test case, with weight factors and the directional limits that are covered by the weight factors

5.1.2. Output r-DPRA analysis

In Figure 5.10, the theoretical components are plotted, thus the components directly from the discretization step. In Figure 5.11, the actual components found by r-DPRA are shown based on a PHAROS run with a model domain as shown in Figure 3.5. It can be seen that their directions are deviating slightly and a few random components are found. This effect can also be seen when a higher resolution is used for the discretization of the wave spectrum, as in the Figures 5.12 and 5.13.

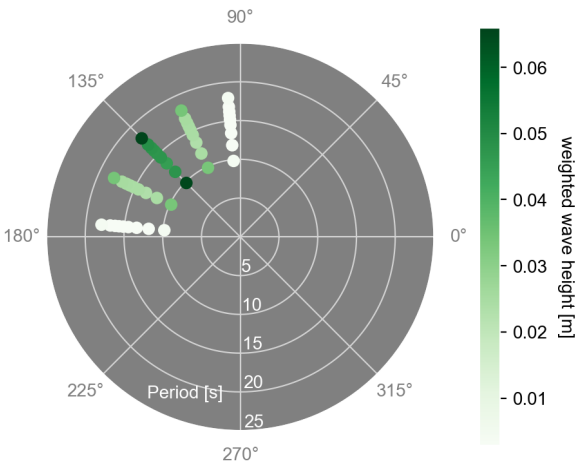

Figure 5.10: Theoretical components for $T_p = 16s$, $N_f = 19$ and $N_{dir} = 5$

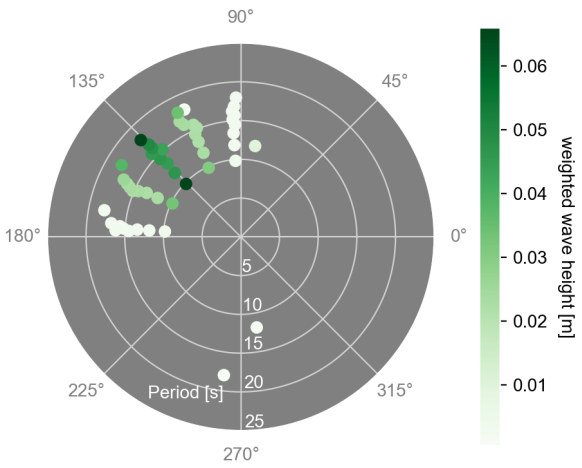

Figure 5.11: r-DPRA output components for $T_p = 16s$, $N_f = 19$ and $N_{dir} = 5$

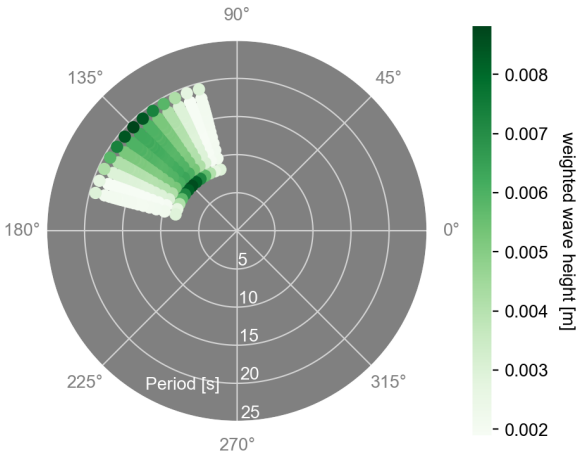

Figure 5.12: Theoretical components for $T_p = 16s$, $N_f = 19$ and $N_{dir} = 13$

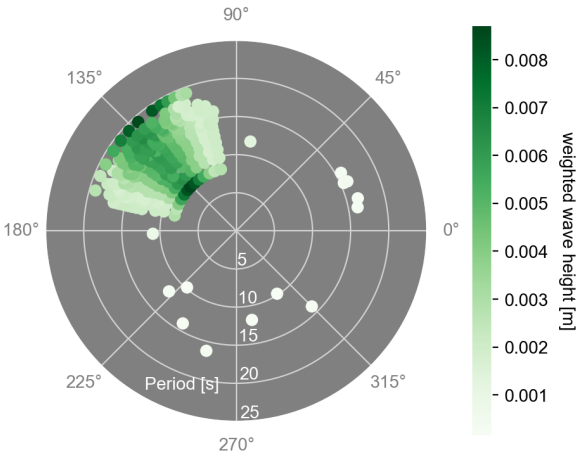

Figure 5.13: r-DPRA output components for $T_p = 16s$, $N_f = 19$ and $N_{dir} = 13$

5.2. DIFFRAC setup

For a 2D spectral simulation, the hydrodynamic database created by DIFFRAC for the single harmonic is not sufficient anymore. As the spectrum is discretized in multiple frequencies and directions, the steps sizes in DIFFRAC should also be decreased to have a similar resolution in PHAROS and DIFFRAC. Based on feedback from MARIN, it was chosen that the primary wave frequencies range from 0.05 rad/s to 4 rad/s with a step size of 0.05 rad/s. The upper limit is double with respect to the previous HYD file, which had a limit of 2 rad/s. The directional resolution is increased as well, to step sizes of 5° instead of 10°.

5.3. aNySIM

The output of the PHAROS computation consists of discreet wave harmonics with their own amplitude, direction and frequency. The next step is to implement this in the ship motion model aNySIM. A limiting factor here is the capabilities of the aNySIM package and the DIFFRAC hydrodynamic database. The most efficient way of implementing the wave components must still be compatible with aNySIM or DIFFRAC. Furthermore, the conservation of directional spreading is a limiting factor. In Figure 5.14, 4 methods of transfer of wave information are schematized.

The first method is to create a one-dimensional wave signal by adding all individual components with random phases. In this method, however, only a single direction is given. This method is already known to be compatible with aNySIM and DIFFRAC. However directional spreading is not preserved in this method. Furthermore, weighted averaging in port basin can become a challenge, as multiple reflected components can be found. When all components approach from a single directional bin of for example 90°, as is the case in the test situation, averaging is straight forward. When components approach from multiple directions, the average direction can become unrepresentative for the local wave field.

The second and third methods are based on fitting a JONSWAP spectrum based on energy conservation. For the second method, the spectrum is 1D, meaning it is assumed that all energy comes from a single direction. The third method, however, also applies the fitting in the directional spectrum.

Though, with these methods, a fundamental question can be raised if a JONSWAP spectrum is representative for the wave conditions at a berth in a port basin. In the pre-processing of PHAROS, a JONSWAP spectrum is split up in discreet wave components. The reverse can be done as well, constructing a JONSWAP based on discreet wave components. In the method of discretization, weight factors are allocated to wave periods based on the energy contained in their region of the Energy Density Spectrum. When applying the reverse, for every component, the energy package is known, just not the shape of the spectrum. An iteration can be done to fit JONSWAP spectra with different parameters to match the energies of the discreet wave components. In a directional spread run, the same can be done in the directional domain. The end product is a

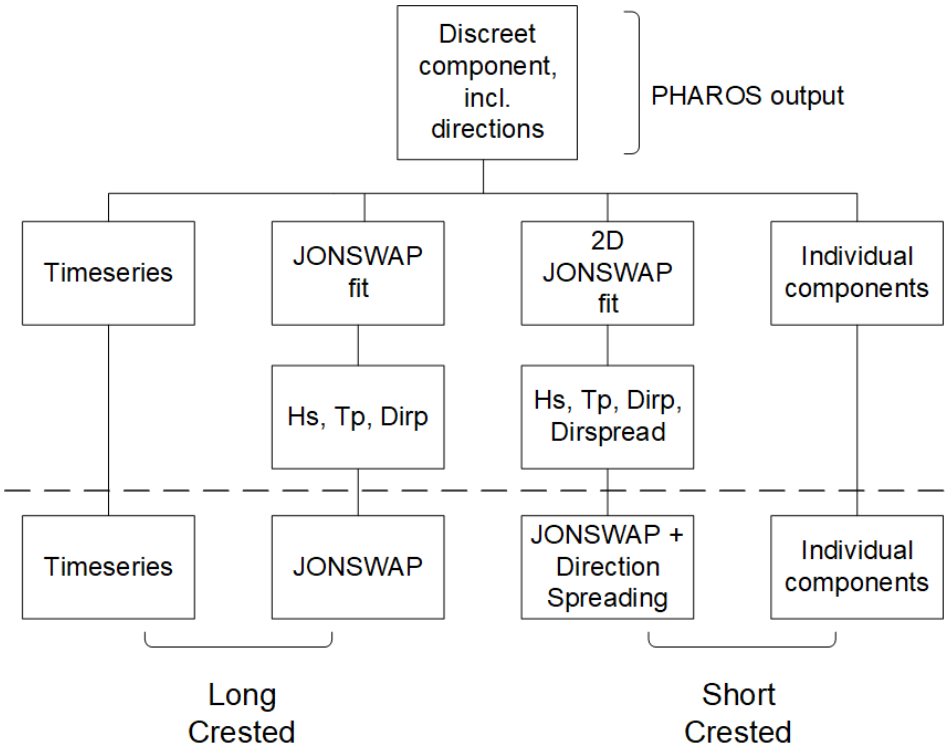

Figure 5.14: Conversion methods that are considered for the coupling of PHAROS and aNySIM

JONSWAP spectrum with a certain directional spreading. This is also known to be compatible with DIFFRAC and aNySIM.

The fourth method is a one-on-one translation of the discreet wave components. A list is given to aNySIM containing all components, with their amplitudes, phases, frequencies, directions. This is the cleanest way of implementing the PHAROS results in aNySIM, as only errors due to the random allocation of phases are introduced, but the exact shape of the wave spectrum at the berth (as computed by PHAROS) is preserved. An advantage is also that directionality is preserved.

5.3.1. Reference model

The results of the different methods are compared with the analytical solution. In this reference case (PHAROS run as shown in Figure 3.5), the wave boundary of PHAROS is directly imposed in aNySIM. As there are no structures in the domain, a constant depth and no bottom friction, the wave climate should be the same at any point in the domain as the boundary. Therefore, imposing this boundary in aNySIM can be considered as the analytical solution.

Imposed is a JONSWAP spectrum with a peak period of 16 s and a significant wave height (H_{m0}) of 1 m, going to 135°. The one-sided spreading range is set to 55°, the number of frequencies to 40 and the number of discreet directions to 30. A large number of aNySIM simulations in done to check the dependency of the vessel forcing results on the assumed random phase angles. Each simulation consists of a combination of the same wave components with different random phases as input. What can be seen when looking at the wave signal of these distinct runs, is that randomness also plays a role here, which is confirmed by the statistics of the water level elevation. In Figures 5.15 and 5.16, the convergence of the averages are shown. After every run with a simulation time of 1 hour, the average is calculated of the previous simulations and normalised with respect to the average after 25 simulations. It shows the effect of running more simulations on the average values. For the primary waves, the average becomes within a 3% accuracy already after 5 simulations. The same holds for the modelled water level, see Figure 5.17.

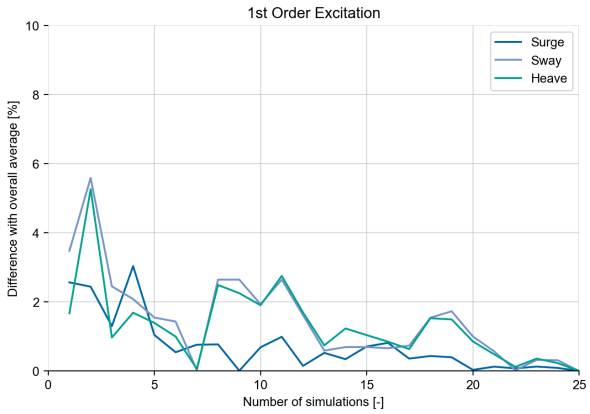

Figure 5.15: 1st Order Excitation results, Reference model

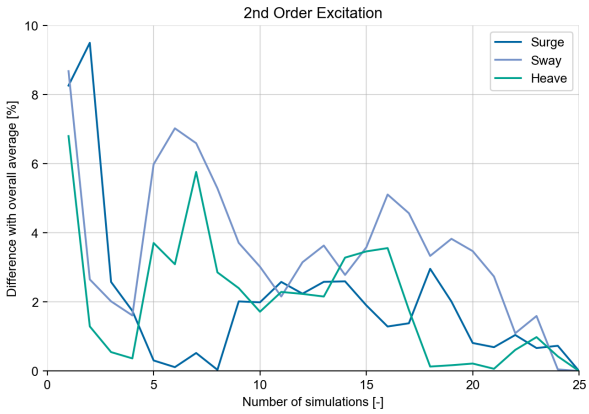

Figure 5.16: 2nd Order Excitation results, Reference model

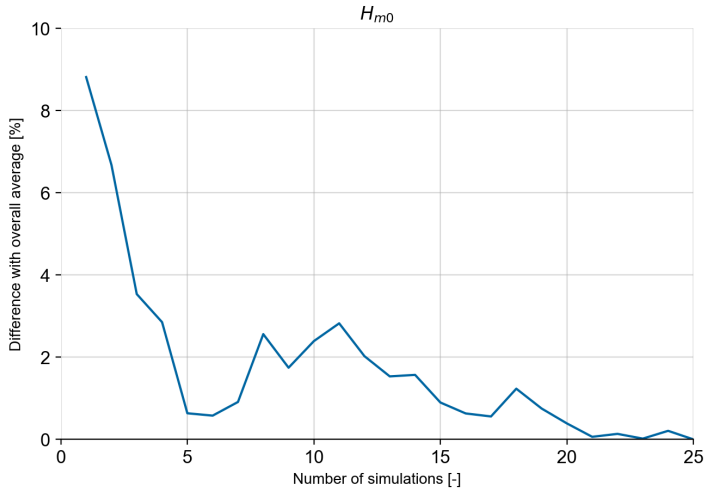

Figure 5.17: Wave height results, Reference model

5.3.2. Method 1 - Time Series, Long Crested

In the first method, all separate components are summed, discarding their directions. By weighted averaging, the peak direction is found. The full time trace travels to the peak direction, making this a long crested method. Directional spreading is not taken into account. The energy of the individual components is summed per frequency, so every frequency is represented by one single harmonic. The components are assigned a random phase and then summed. This creates a time trace that is saved as a text file and loaded into aNySIM.

5 Simulations with different time series from the same list of components are created. The difference between them is solely due to the random phases assigned to the components. A comparison is made with the reference model. In Table 5.1, the average differences with the reference model are shown. E.g. in the third row, the value equals the difference between the reference run and the average of the 3 simulations above. The comparison is made between the standard deviations of the time traces generated by aNySIM, as this is a measure for amplitudes. It can be seen that the difference does not change much when averaging over multiple runs. This means the time duration of the simulation is sufficient and the random phase allocation errors disappeared. In this method, there is therefore no need for running more simulations and averaging to get rid of possible initial phase angle induced errors.

The second order excitation forces are greatly overestimated, in the order of thousands of percents. This is explained by the assumption that is made is this method, all components travel from a single direction. For the bound long wave, a second order effect, this means all components interact to create the bound long

wave. However, the r-DPRA tool finds that components travel from different directions. This means not all of them interact to create a bound long wave, only components coming from the same direction (and directions close to that direction). Therefore, the second order wave forces are overestimated as seen in Table 5.1.

Table 5.1: Time Series ship forces; difference between the average of the simulation with respect to the reference run (comparison in standard deviations of time traces)

	1st Order Excitation Force			**2nd Order Excitation Force**			
	Surge	**Sway**	**Heave**	**Surge**	**Sway**	**Heave**	**Hm0**
sim1	13.1%	-20.3%	-11.0%	2101.9%	2907.3%	119.0%	0.8%
sim2	13.3%	-20.2%	-10.8%	2226.4%	3083.4%	118.8%	1.1%
sim3	12.7%	-20.5%	-11.3%	2234.0%	3084.7%	117.0%	0.7%
sim4	12.5%	-20.7%	-11.4%	2225.9%	3077.9%	118.3%	0.5%
sim5	12.6%	-20.6%	-11.3%	2182.2%	3023.5%	119.2%	0.6%

5.3.3. Methods 2 and 3 - JONSWAP-fit, Short and Long Crested

A second method that is evaluated is the JONSWAP fit. This can be done for both short crested as long crested runs. In the case of long crested runs, the energy is summed per frequency and all frequencies are assigned the same direction, the peak direction that follows from averaging all components according to their weights. The core of this method is the reverse of the pre-processing step. In that step, a 2D JONSWAP spectrum is divided into discreet components. Here, the opposite happens, discreet components are used to construct a JONSWAP spectrum. Every component contains a certain amount of energy which represents its weight. This energy changes due to the propagation through the PHAROS model. An iteration is done to check which spectrum shape, parameters, approaches the discreet energy distribution the best. The H_{m0}, T_p and γ are changed for every iteration, and the Root Mean Square Error (RMSE) are calculated. Finally, the results are evaluated and the combination of parameters with the smallest RMSE is selected. The results showed almost a perfect fit, as this is a highly theoretical case.

The most important disadvantage of this method is the assumption that the local wave climate is well represented by a JONSWAP spectrum. After penetrating into the port basin, wave diffraction and reflection causes the wave field to change. It is uncertain if the local wave field is still described by a JONSWAP spectrum. In the test case, the wave energy does not change significantly and therefore a very accurate fit is found. This can however not be said for more complex cases. Therefore, this method is discarded, both the 1D and 2D versions.

5.3.4. Method 4 - Direct Component, Short Crested

This method is considered the cleanest. The discreet components are directly implemented in aNySIM, and therefore no additional errors are introduced. In aNySIM, a list of components is set with the variables: Amplitude, Potential Amplitude, the relative wave number in both x and y direction, the radial frequency, the phase and the water depth, see Table 5.2. The wave number components in x and y direction are normalised with the wave number. With this list, aNySIM generates a wave field. This is basically the same as aNySIM does when imposing a prescribed spectrum with directional spreading: It discretizes the components and calculates the parameters. Consequently, the wave field is computed by summing all the components.

Table 5.2: Input parameters Direct Component method

Parameter	**Definition**	**Determination**
a	amplitude	$0.5 * H$
c	potential amplitude	$(a * g)/\omega$
k_x	x component wave number	$k * cos(\theta)$
k_y	y component wave number	$k * sin(\theta)$
ω	radial frequency	prescribed
ϕ	phase	random
h	water depth	prescribed

First, an analysis is done that compares the theoretical wave field with the computed wave field. At the

PHAROS boundary, a JONSWAP wave spectrum with a Tp of 16 seconds and a directional spreading of m = 12 are imposed. Two different PHAROS runs are considered with different resolutions in the frequency domain. The resolutions are 9 and 19 components in the frequency domain and 5 components in the directional domain, which leads to 45 and 95 separate PHAROS runs respectively. The difference in computational time for this base case was considered negligible.

By plotting the components in a polar plot, as shown in Figures 5.10 and 5.11, visual interpretation can be done to identify patterns.

To compare the theoretical wave field following from the direct component method with the computed wave field, the H_{m0} values are compared. The theoretical H_{m0} is known, as this is imposed. The computed significant wave height H_{m0} is computed by looking at the statistics file of aNySIM. The statistics file gives the standard deviation of the water level. As waves are considered to be Gaussian distributed, the H_{m0} can be calculated by $H_{m0} = 4 \cdot \sigma$.

This comparison is made for different significant wave heights, to check if the error due to the phase-locking behaves linearly as well. Moreover, a higher resolution is applied as well (N=19 vs N=9) to check whether the error reduces with a higher resolution. The results are plotted in Figures 5.18 and 5.19.

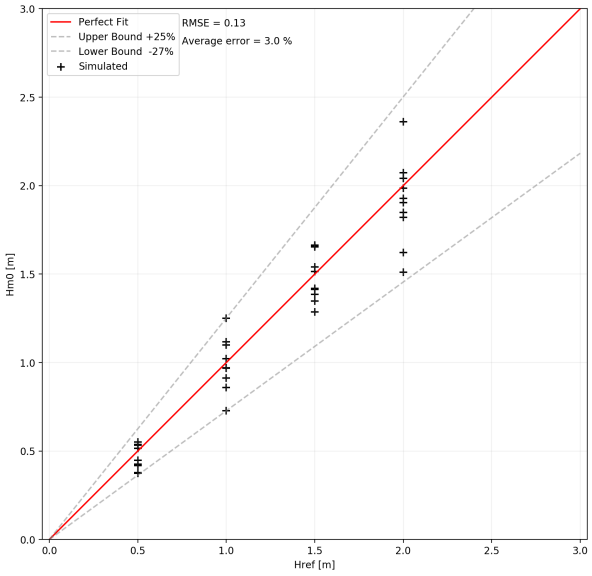

Figure 5.18: Phase sensitivity for $N = 9$, Direct Component method

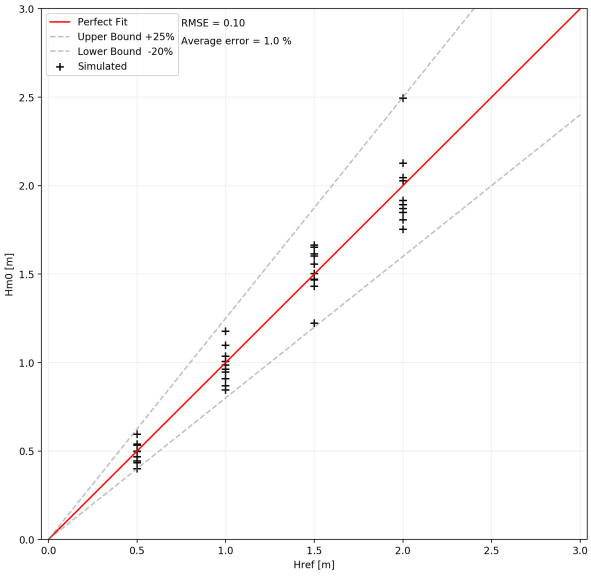

Figure 5.19: Phase sensitivity for $N = 19$, Direct Component method

The phases are randomly selected; every time the script creates the list of components, different phases are assigned to the components. This randomness leads to different wave fields in aNySIM for every set of initial phase angles. The analysis is done for both a frequency resolution of 9 components and 19 components to compare results. It can be seen that the influence of the resolution is as expected: The higher the resolution, the lower the errors, although the difference is minimal. Moreover, the error behaves linearly, as expected, with the significant wave height.

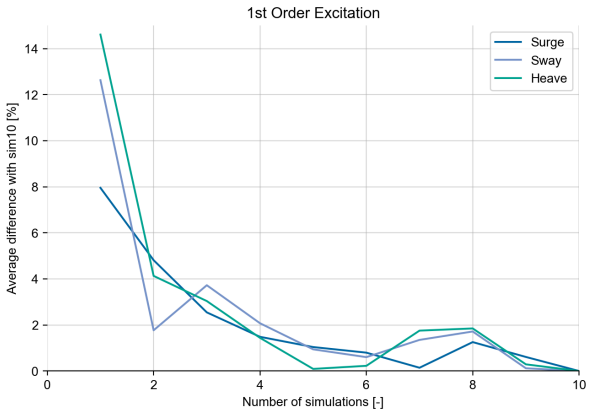

Figure 5.20: Divergence standard deviation average 1st Order Excitation. Compared with average over 10 simulations

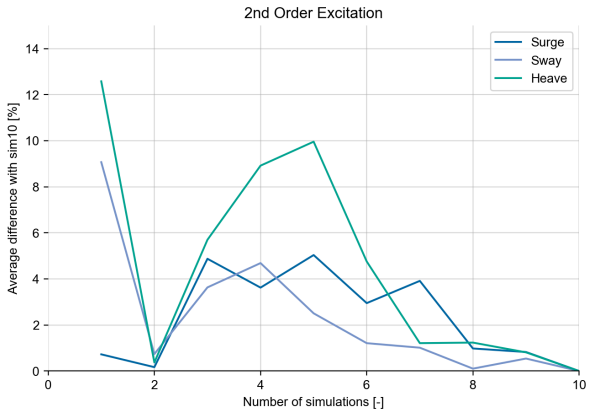

Figure 5.21: Divergence standard deviation average 2nd Order Excitation. Compared with average over 10 simulations

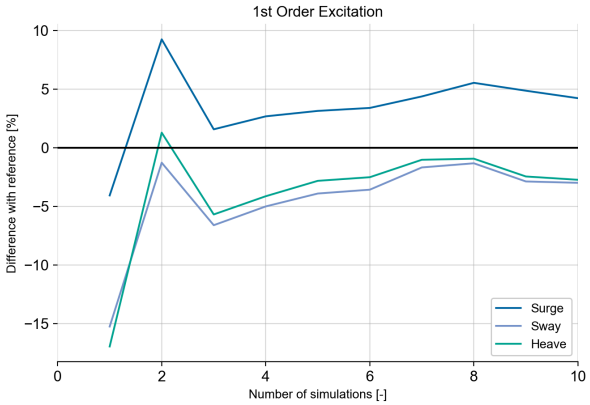

Figure 5.22: Divergence standard deviation average 1st Order Excitation compared with reference case.

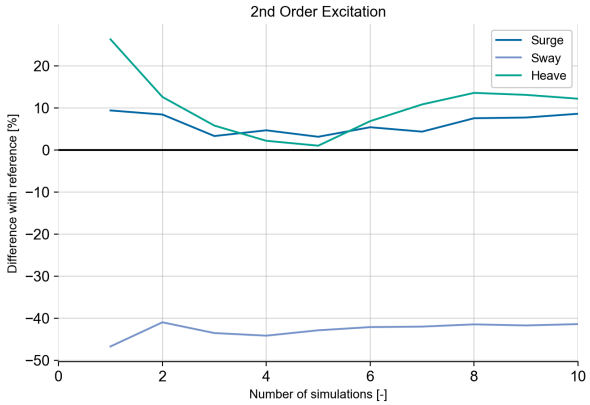

Figure 5.23: Divergence standard deviation average 2nd Order Excitation compared with reference case.

In Figures 5.20 and 5.21, the convergence is shown for the direct components method. The number of simulations on the horizontal axis indicate the number of simulations of which the resultant amplitudes are averaged. Like in the reference method, the convergence in the first 5 runs is much stronger than in the last runs. In Figures 5.22 and 5.23, the comparison is made with the reference run. Here, the same holds: The graphs are stable after 4 or 5 simulations. This shows that for the Direct Component method, in order to get steady average results, 5 simulations can be considered sufficient. Running longer simulations does not improve the results as a phenomena called phase-locking occurs. The discretization leads to a list of components where every frequency contains components in multiple directions. As their frequencies are equal, their propagation velocity is equal as well. This causes deviation between runs with different relative initial phase angles, as they do not die out over time, their phases are *"locked"*. In Appendix D, an alternative method is discussed, the *single summation method*. This method has potential to overcome the phase locking issue, however, it was chosen to continue with the original *double summation method*, that is currently implemented as standard in aNySIM. The alternative method divides the multiple components from a single frequency over the frequency band. Therefore it introduces errors, as different frequencies behave differently in PHAROS. Moreover, simulation times can reach up to a day in order to get rid of the phase-locking phenomena, while a typical representative aNySIM simulation has a duration 3.5 hours.

5.3.5. Comparison methods

The performance of the two considered methods, Direct Component and Time Series, are compared and the results are shown in Table 5.3 based on an average of 5 aNySIM simulations.

It can be seen that the Direct Component method performs better than the Time Series method, both for the 1st order excitation as the 2nd order excitation. Especially for the 2nd order excitation, the differences are

Table 5.3: Performance of standard deviations Direct Component and Time Series method with respect to the reference run

	1st Order Excitation Force			2nd Order Excitation Force			
	Surge	**Sway**	**Heave**	**Surge**	**Sway**	**Heave**	**Hm0**
Direct Component	4%	-3%	-3%	9%	-41%	12%	0%
Time Series	13%	-21%	-11%	2182%	3023%	119%	1%

significant. As mentioned earlier, the Time Series method greatly overestimates the 2nd order excitation by assuming all components interact to a bound long wave. For the direct component method, only the components coming from (nearly) the same direction interact and this is a better representation of the physical process.

5.4. Conclusion Coupling 2D Wave Field

After evaluating the performance of 4 different conversion methods, the two (long-crested and short-crested) JONSWAP fitting methods were discarded at first, due to the uncertainty about how well a wave climate within a port basin is represented by a JONSWAP spectrum and moreover because it would introduce new errors due to the conversion from a discreet to a continue spectrum. The Time Series method and Direct Component were tested and it was concluded that the Direct Component method was the most promising, as directional spreading is preserved and the difference in computational effort was negligible (matter of seconds longer runs).

Moreover, the Time Series method has disadvantages when applied in complex port basin geometries. When multiple reflected and diffracted waves are present at the location, the weighted averaging is not straight forward, as the different components must be distinguished manually. Furthermore, the second order excitation forces are greatly overestimated by the Time Series method. As all components travel from the same direction, all components interact to create a bound long wave. When a large spreading is present, components can have large differences in directions, making it unrealistic that they create a bound long wave. The Direct Component does take this difference in direction into account for the calculation of the bound long wave.

For the Direct Component method, a phenomena called phase-locking occurred that greatly influences the results. This is not related to the coupling method itself, but to the way a spectrum is described in aNySIM, namely using the double summation method. The same phase-locking phenomenon therefore occurs in the reference run presented here using a standard JONSWAP spectrum as input in aNySIM. Therefore also for the reference run an average of multiple simulations was used. To overcome the strong dependency of the solution on the selected random phases, two methods were discussed: Running multiple aNySIM runs and averaging and using the single summation method instead of the (standard) double summation method. As the for the latter new errors were introduced and the simulation times became significantly larger, it was decided to use the former method.

To conclude, the Direct Component Method is used for the coupling of PHAROS, aNySIM and DIFFRAC for full 2D wave spectra, after extracting components with the r-DPRA tool. In the next chapters, the coupling is applied to a case study, the outer port of La Coruña.

6

Measurements Outer Port of La Coruña

6.1. The Outer Port of La Coruña

The motive for constructing a new exterior port can be found in 3 incidents that were related to the waters around La Coruña. The 12th of May, 1979, the oil tanker Urquiola struck bottom just before entering the port of La Coruña. Oil began leaking out and in order to avoid having explosions inside the harbour, the ship was directed offshore. When sailing towards offshore, it struck the bottom again and got stuck in between the two entrance channels. Several explosions followed which killed the captain of the ship. 100,000 tonnes of crude oil were spilled of which a quarter washed ashore (International Tanker Owners Pollution Federation, 2019). It could struck the bottom because the location of the entrance channels was not indicated properly.

The oil tanker named Aegean Sea was the next incident near the coast of La Coruña. On the 3th of December 1992, After being ordered into the port the heavy conditions pushed it away from its path and it ran aground. After breaking in half, crude oil started to spill. 67,000 tonnes of oil was spilled, nearly 3 times as much as with the Urquiola. Soon after breaking, the ship caught fire and kept burning for 5 days. The coast was affected up to 300 km away from the city, but fortunately the full crew survived.

The largest environmental disaster in the history of Spain and Portugal happened on the 13th of November 2002. The oil tanker named Prestige started leaking oil due to a combination of structural deficiency and severe weather conditions. After 5 days, it eventually sank 250 kilometres away from the Galician coast. 63,000 tonnes of oil were spilled and thousands of kilometers of coastline were polluted in both Spain, Portugal and France.

These accidents raised the question what would have happened if the disasters happened within the port, or even at the quay. Looking at the inner port layout, the consequences can already be seen if such disasters would happen there. The oil terminal is relatively close to residential areas, with even the pipes to the refinery passing the residential area. A second disadvantage is contamination of the bulk terminal, where coal is handled. With a prevailing wind direction transporting the pollutants to the residential area as well. It was therefore decided that it was highly necessary to construct a new outer port, further away from the city of La Coruña. Although the environmental conditions are far from ideal for constructing a port, no feasible alternatives were found. Around the year 2000, the first designs were made for the outer port of La Coruña, named Langosteira, especially meant for harmful and polluting cargo like coal and oil. The enormous dimensions were a challenge and many scale models were used to optimize the design. A limiting factor was the lack of reliable wave data at the location. The final design was made for a significant wave height of 15 meters.

Figure 6.1: Outer port of La Coruña, february 2017 ((Port Authority of A Coruña, 2019b))

During the construction phases, the geometry of the port changed a lot. New inner breakwaters affected the behaviour of the harbour and it was therefore expected that the response of moored ships would change as well. The Port Authority of A Coruña (APAC) asked the GEAMA, Water and Environmental Engineering Group, of the University of A Coruña (UDC) to analyse the response of moored vessels. The Bulk Carriers all moored at the Transversal dock, see Figure 6.1, while the general cargo vessels moored more to the west, a dock still under construction.

6.2. Measurements campaign

In this section, the measurement campaign in the Outer port of La Coruña is explained. Different measurement techniques that were used for the measurement of ship motions are discussed and other measurement devices are presented.

Peña et al. (2017) explained the measuring methods in detail. Here, the methods are briefly discussed. The IMU, which stands for **Inertial Measurement Unit**, is used to estimate angular motions of the vessel. The gyroscope that is included in this device is the primary source to obtain the orientation information. To avoid interference, the device is installed away from electromagnetic sources, normally inside the bridge of the vessel. The recording frequency of roll, pitch and yaw is 4 Hz, 4 measurements per second.

The second measurement technique is the **Virtual Tracking System**, VTS. Cameras were used to register the heave and surge motion of moored vessels. An algorithm chooses certain points that are tracked by analysing the area around the original pixel. By selecting tracking points on the middle line of the vessel, the error due to rotations can be minimized.

The last measurement technique is the **Laser Distance Meter**, LDM. Two units are installed on the quay where the vessel is moored. The lasers measure the distance between the quay and the hull of the ship. Therefore the positions has to be chosen, that a constant surface is present around the point where the laser beam hits the vessel. Installing one at the bow and one at the stern leads to yaw and sway measurements. The sway is considered the main information, with the yaw information as additional measure, as this is already measured by the IMU (Peña et al., 2017).

A **Tidal Gauge** installed inside the port basin continuously measures the water level. Once a minute mean sea levels can be retrieved from the website of the Ministerio de Transportes Movilidad Y Agenda Urbana (2019).

At the entrance of the port basin, an **AWAC** is installed. The AWAC, Acoustic Wave And Current, unit was developed by Nortek and is used as current profiler and directional wave system. This system was deployed to provide hourly wave statistics. Due to the battery duration, the AWAC was not deployed continuously and some mooring periods do not have AWAC data. However, 4 vessels were identified during measurements of the AWAC, and therefore the AWAC data can be used for validation of the PHAROS model. The statistical parameters that are measured by the AWAC are shown in Table 6.1.

Table 6.1: Hourly AWAC data

Significant Height (H_{m0})	Peak Period (T_p)	Peak Direction (dir_{Tp})
Mean 1/3 Height (H_3)	Mean 1/3 Period (T_3)	Directional Spread (dir_{spr})
Mean 1/10 Height (H_{10})	Mean 1/10 Period (T_{10})	Mean Direction (dir_m)
Maximum Height (H_{max})	Maximum Period (T_{max})	
Mean Height (H_{mean})	Mean Period (T_{m02})	

Just 1.5 km outside the port, a **Wave Buoy** is deployed that provides real-time wave climate information. Like the AWAC, the wave buoys output is hourly statistical data, see Table 6.2.

Table 6.2: Hourly Buoy data

Significant Height (Hs)	Mean Period (Tm)	Mean Direction (Mdir)	Wind Velocity (Wvel)
Maximum Height (Hmax)	Peak Period (Tp)	Peak Direction (Pdir)	Wind Direction (Wdir)

The **SIMAR** inside the port basin provides the necessary wind data. Every hour, the wind direction and velocity are returned. During the measurement campaign, pressure sensors were also deployed in the corners of the basin. However, there were no recordings during the measurements of the vessels.

In Figure 6.2, the locations of the different measurement devices are shown: The tidal gauge, AWAC and SIMAR inside the port basin and the wave buoy just outside the basin.

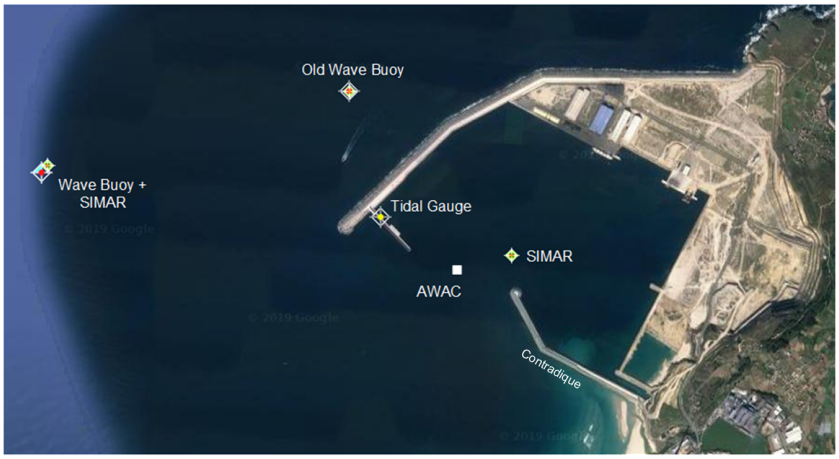

Figure 6.2: Locations measurement devices. Old wave buoy used until 2011

After consulting the Port Authority, some qualitative aspects of the port operations were found. Of all 6 motions, roll causes the most hindrance for the port operations in general. Looking the location and orientation of the quay, the expected predominant wave direction is almost perpendicular to the quay, this can explain the roll motions. Furthermore, in extreme conditions, the breaking of multiple mooring lines can occur. As the tidal range at the berth can be up to 4 m, mooring lines constantly have to be adjusted to prevent breaking of mooring lines and extreme ship motions. It was said that the general idea is that when a single mooring line breaks, that line was not properly adjusted to the change in water level. If more than one line breaks, the most probable cause would be the heavy wave climate. For these breaking lines, the campaign was set-up, in

order to try to predict which conditions are limiting for safe mooring and to prevent unsafe situations like the breaking of mooring lines.

6.3. Measurements

From the winter of 2015-2016 until the winter of 2018-2019, several vessels were monitored. In this period, 19 Bulk Carriers and 17 General Cargo vessels were included in the campaign. As three independent measurement techniques were used, not for every vessel all 3 methods were functional. To install the gyroscope, permission must be granted by the captain and to install the laser-distance meters, safety on the quay must be guaranteed. The cameras registering heave and surge are attached to the lampposts, this means that only if ships berth in front of one of these posts, the surge and heave can be registered. During the campaign, the offshore buoy registered a maximum significant wave height of 12.37 m and a maximum peak period of 20 seconds.

A selection must to be made of vessels that are suitable for the model validation. To select these vessels for the model validation, the limiting factor is that all the data must be present at exact the same time. During these years, new structures were build in the port basin, also changing the bathymetry. It is chosen to use the most up-to-date bathymetry, meaning the "Contradique", shown in Figure 6.2, is included. This means 2 of the 4 winters can be used with the most monitored vessels. The general cargo vessels moored at a quay without installed cameras, and therefore no heave and surge motions were registered. These vessels are discarded for the model validation. The final selection of vessels is presented in Table 6.3.

Table 6.3: Overview vessels suitable for model validation

Vessel	**DWT**	**Length**	**Cargo**
Kyzikos	92,598 t	229.5 m	Mais
Nord Saturn	77,288 t	225.0 m	Bauxite
CSK Unity	77,105 t	225.0 m	Mais
Aloe	30,618 t	178.7 m	Wheat
Don Juan	21,057 t	158.0 m	Coal, clinker
Pegasus	81,852 t	179.9 m	Unknown

3 independent measuring methods were used to capture both the vessels rotations as translations. An IMU was installed in the bridge for all three rotations, a LDM on the quay measured the sway motion and lastly a camera combined with a VTS captured the heave and surge motions. The vessel Aloe was chosen as it had the most hours of data available of all three sources.

Then, a window had to be found were all these 3 different data sources were available. Two windows were suitable, both lasting approximately 8 hours. As draught estimations had to be made based on the photo at the start of the window and the mooring configuration was only captured at the same moment, the first window was chosen.

6.3.1. Wave Climate

Table 6.4: Hourly Buoy data (C.R. = Cero Redmar

	Base Case	**Heavy Case**
Date	20/02/2018	20/02/2018
Time	10:40 hrs	18:00 hrs
Significant Wave Height	2.41 m	3.70 m
Peak Period	14.3 s	16.7 s
Peak Direction	312°	316°
Water level	C.R. +1.05 m	C.R. +3.45 m

During the mooring of the vessel Aloe, the offshore significant wave height ranged from around 2.3 m to 3.7 m. The peak period ranges between 12 s and 18 s, which are considered swell waves. The dominant wave

direction, where the energy peak comes from ranges from 311° to 342°. In Figure 6.3, the time series can be seen of the wave height, wave periods and wave directions during the mooring. The time series represent hourly data. The selected moments for the modelling are determined based on the availability of the ship motion measurements.

Two different conditions are modelled: a moderate condition and a condition with a heavier wave climate. From the wave buoy data, the first and last 20 minutes of the window are chosen. The significant wave heights were 2.41 m and 3.70 m respectively and their peak periods 14.3 s and 16.7 s. The first moment the measurements of the motions of the vessel Aloe started was at 20th of February 2018, 10:40. Then, the heave and surge measurements started. This moment in time is used as the base case.

The 20th of February 2018, 18:00 hrs was selected as heavy case, as both wave height as wave period increased severely, as can be seen in Figure 6.3. Moreover, in contrast with the base case, there was a high tide at this moment, see Figure 6.4. The governing conditions are summed up in Table 6.4. The tidal water level is shown for the mooring of the Aloe in Figure 6.4.

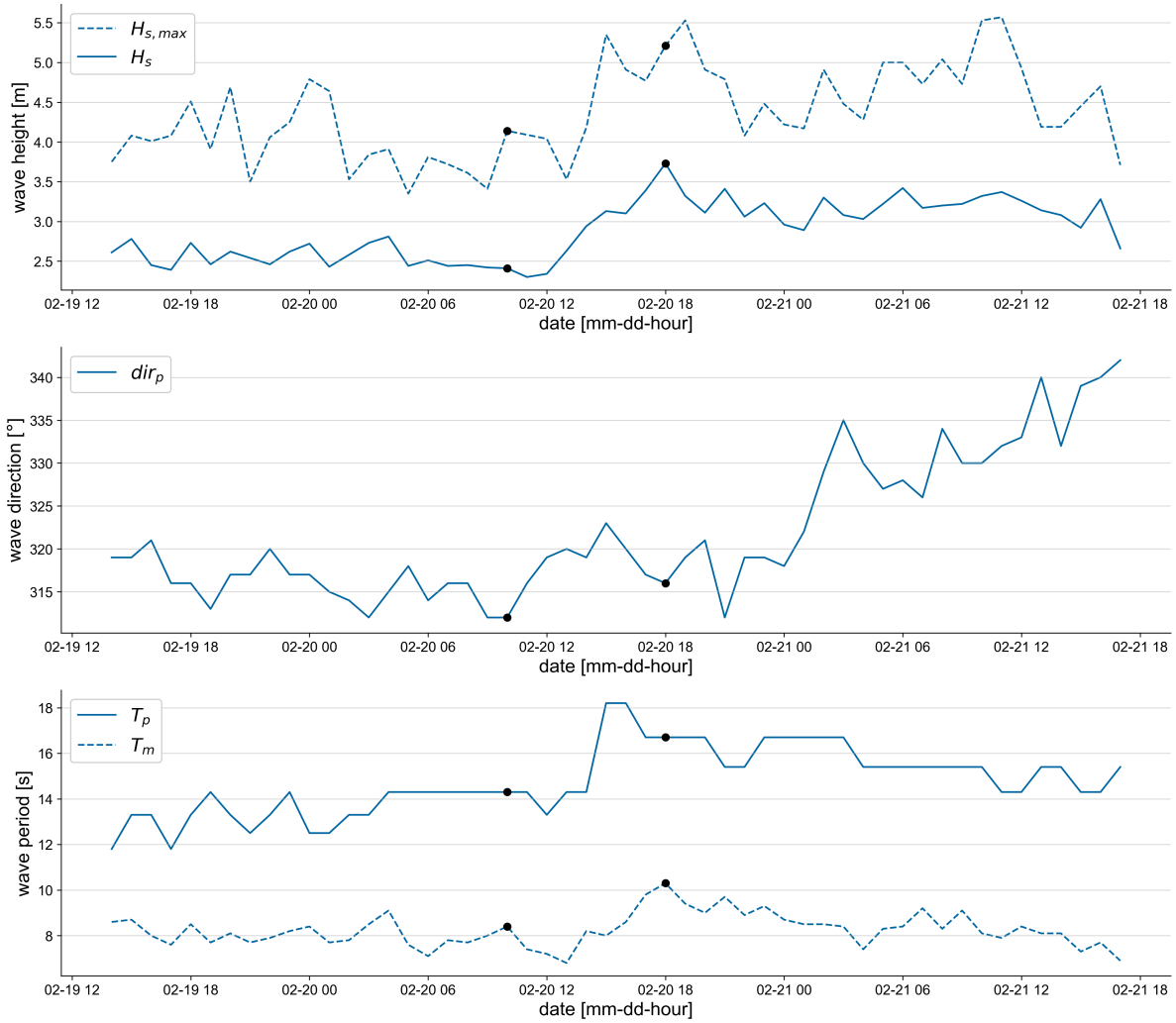

Figure 6.3: Offshore wave climate during mooring of the vessel Aloe, measured by the wave buoy

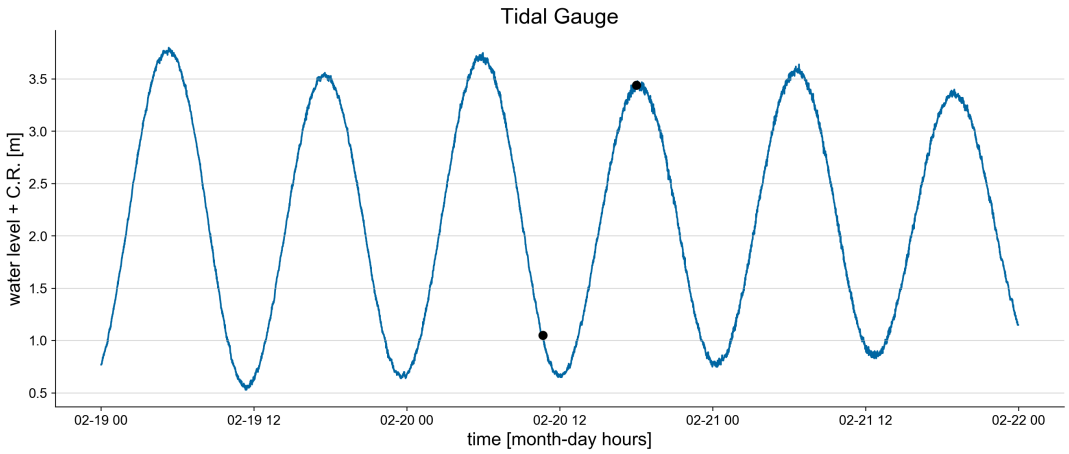

Figure 6.4: Water level measurement during mooring of the vessel Aloe

6.3.2. Ship Motions

The validation is based on the measurements of the vessel Aloe. This vessel was moored in the outer port of La Coruña between the 19th and 21st of February 2018. During the mooring the six motions of freedom were measured and made available for this research by providing both the raw data as the 20-minute statistics. The significant value is calculated by taking the mean of the third highest values. The values, similar to the wave height calculation, are calculated by taking the distance between a consecutive through and crest.

Here, the motion measurements of the vessel Aloe are presented. First, the statistics of the measurements during the full mooring time are presented. Then, the two selected moments are discussed, both the statistics as the time series.

In Figure 6.5 and Figure 6.6, the statistics of the rotations and translations are shown. It can be seen that the rotations were constantly measured, while the heave and surge were only measured a limited amount of time, also caused by low visibility.

Figure 6.5: Measured statistics rotations during mooring of Aloe

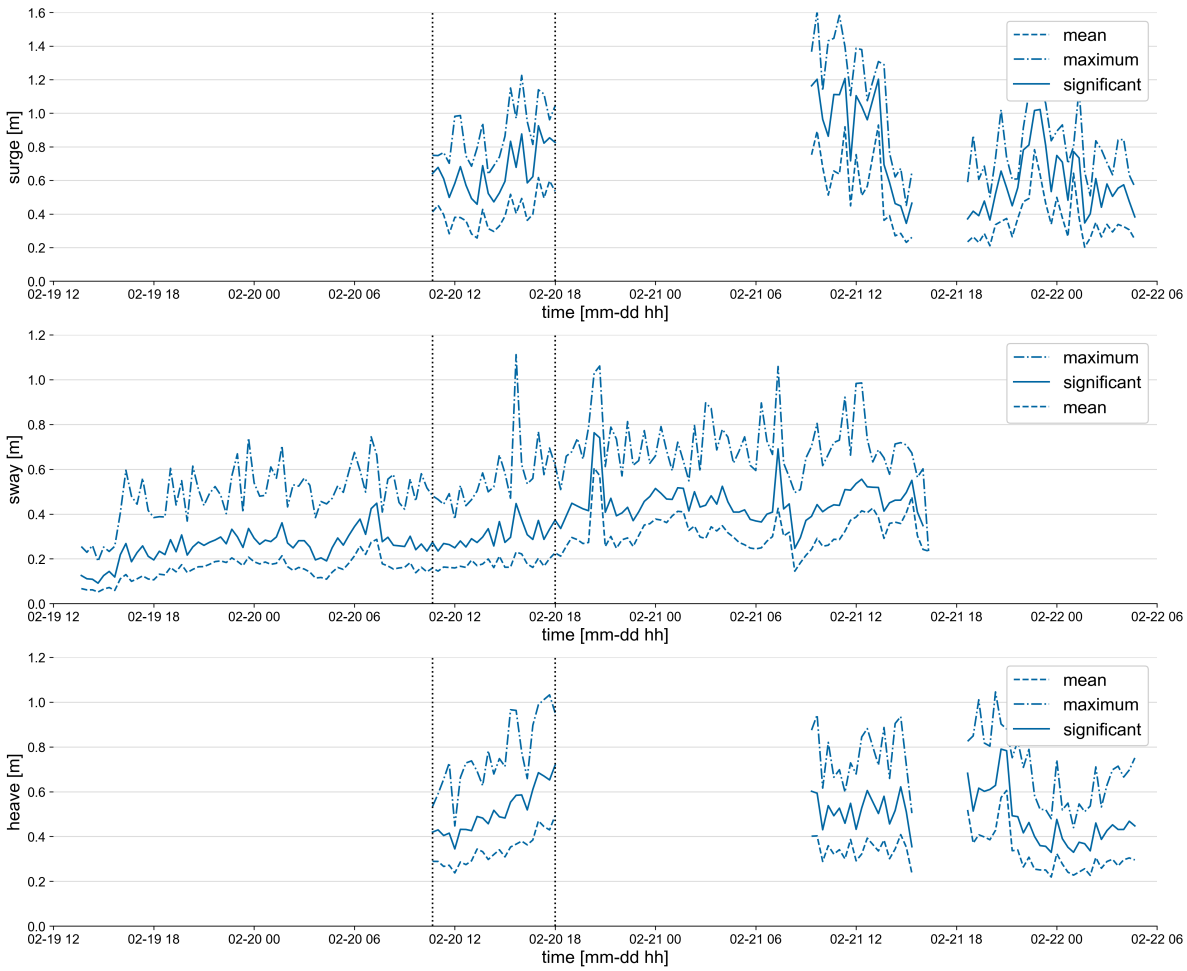

Figure 6.6: Measured statistics translations during mooring of Aloe

Then, the two different cases are considered: The base case and the heavy case. In Table 6.5 and Table 6.6 respectively, the statistics are shown for the 20-min interval.

Table 6.5: Measured peak-peak and significant motions base case Aloe

Motion	Peak-Peak	Significant
Roll	1.59°	1.21°
Pitch	0.32°	0.19°
Yaw	3.16°	2.29°
Surge	0.75 m	0.64 m
Sway	0.25 m	0.07 m
Heave	0.53 m	0.42 m

Table 6.6: Measured peak-peak and significant motions heavier case Aloe

Motion	Peak-Peak	Significant
Roll	1.36°	0.90°
Pitch	0.33°	0.23°
Yaw	2.54°	1.72°
Surge	1.04 m	0.83 m
Sway	0.62 m	0.37 m
Heave	0.96 m	0.72 m

In Figure 6.7 the time series of the rotations are shown for the base case and in Figure 6.8 the time series of the translations.

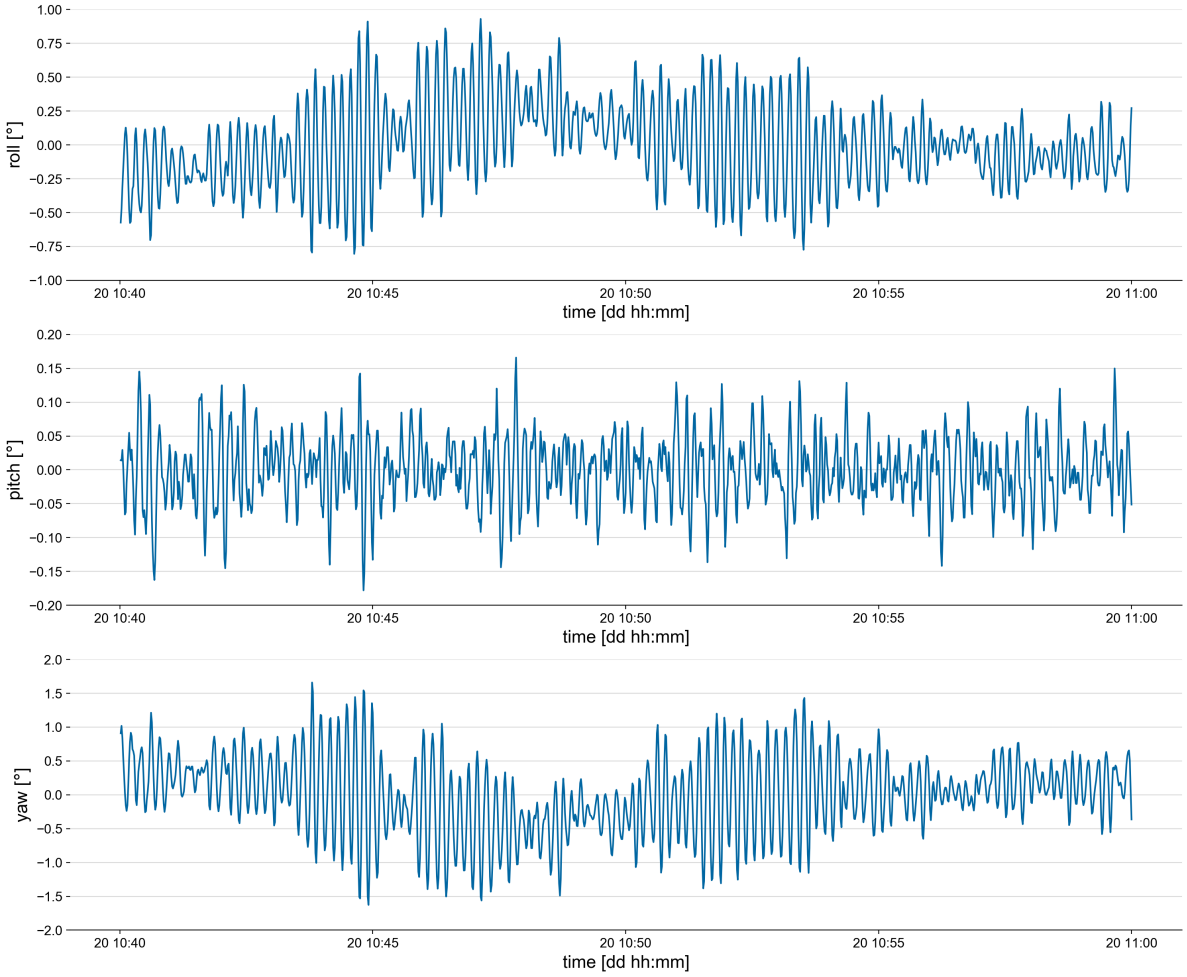

Figure 6.7: Measured rotation time series base case

For all 6 motions, a Fast Fourier Transformation has been done in order to create their motion spectra. A smoothing is applied to be able to more clearly distinguish the most energetic peaks. These are shown in Figure 6.9. The time series and wave spectra of the heavy case, can be found in Appendix E.
For the base case, several aspects can be highlighted from the measurements.

First, a discrepancy is found in the Roll and Yaw motion. They seem to have the exact same pattern and their

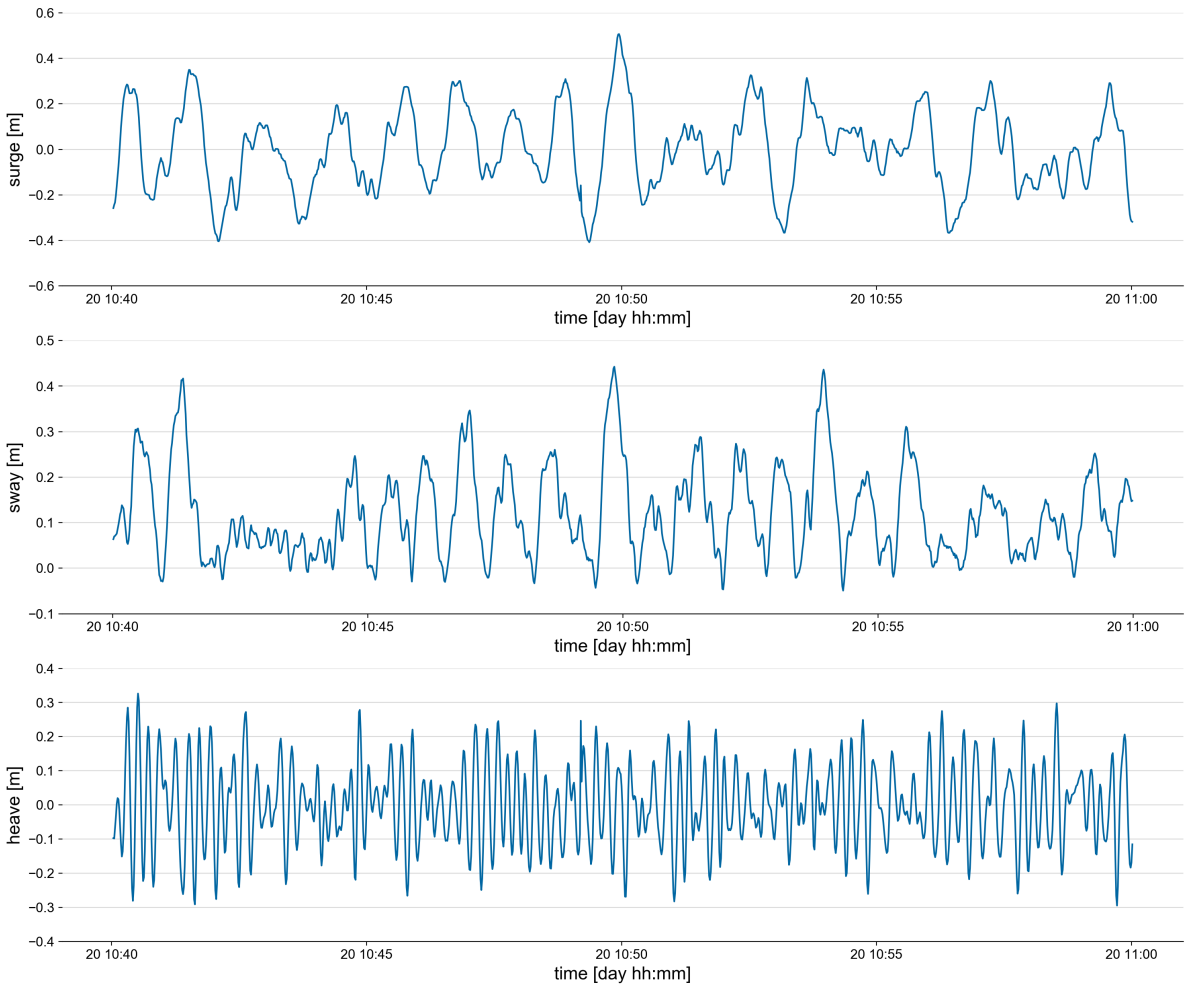

Figure 6.8: Measured motion time series base case

spectra are exactly equal. In is unclear if this an error in the measurement equipment or there is a very strong correlation between these rotations.

Secondly, a strong long wave pattern is found in the time series of the surge and sway. These motions are known to be prone to long wave excitation, as the mooring system and low damping tend to create low natural periods. In the spectra from Figure 6.9, a clear peak in energy is found for surge at approximately 75 s and for sway a less clear peak at approximately 48 s. In Appendix E, an analysis of the natural periods of the system is done, but the surge peak at 75 s was not found to be close to the natural period of the modelled ship.

Third, especially for the heave and pitch motions, there is a wide distribution of energy along the swell frequencies. This can be expected as well, as these motions are less subject to long wave excitation and the mooring system has less influence on the vertical motions of the vessel.

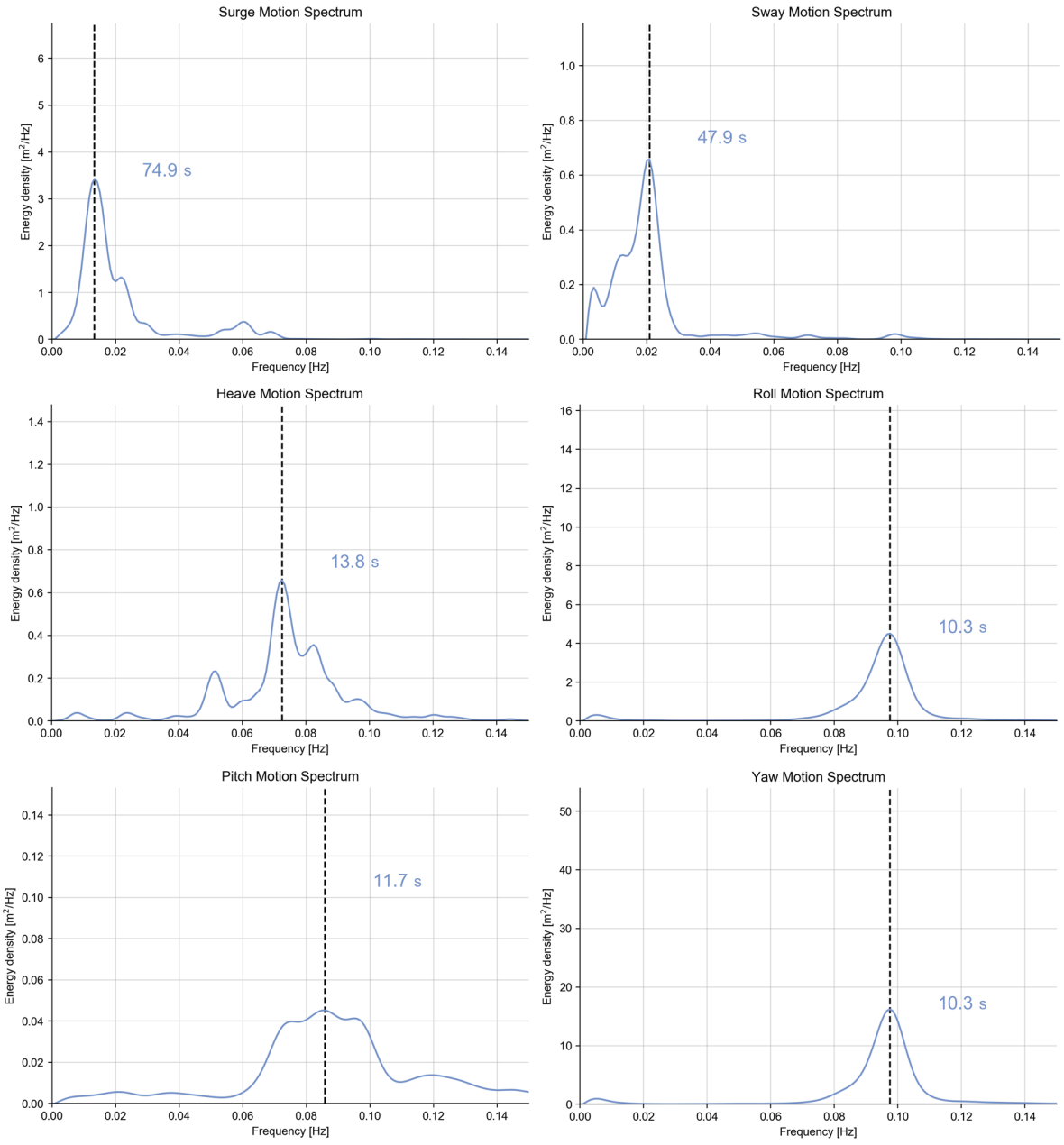

Figure 6.9: Measured spectra base case

7

Computations and comparison

7.1. Model Setup

7.1.1. Bathymetry

The bathymetry map of the coastal area around the outer is shown in Figure 7.1.

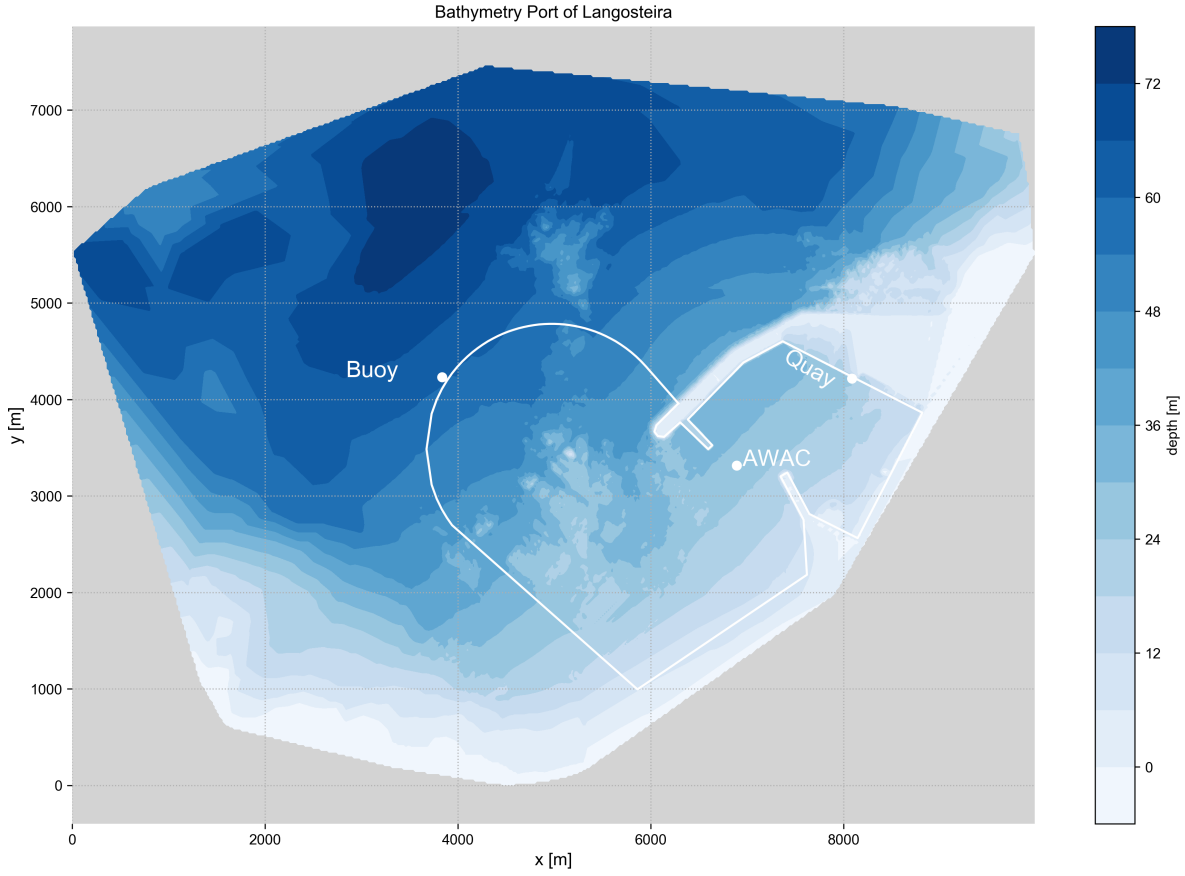

Figure 7.1: Bathymetry map of the port of La Coruña and its surroundings

The bathymetry map of the coastal zone around the port of La Coruña consists of multiple mappings from different moments in time. The larger bathymetry that comprises the coastal stretch and reaches offshore dated from a TOPONORT mapping of 2012 (Port Authority of A Coruña, 2019a). The bathymetry around the port is composed of maps made between 2014 and 2017 constructed by TOPONORT and TOPCAD, including the structures present during the 2018 measurement campaign (Port Authority of A Coruña, 2019a). The

bathymetry maps are combined to one single bathymetry map that serves as input for PHAROS, see Figure 7.1. The location of the wave buoy is shown in Figure 7.1, just like the locations of the AWAC and the moored vessel.

7.1.2. Boundaries

For every boundary, the reflection coefficient must be determined. As discussed in Chapter 3, this coefficient is set for one incoming wave angle. When the incoming wave angle deviates from this angle, the reflection coefficient changes according to Figure 3.8. The boundary determination is shown in Figures 7.2 and 7.3.

Therefore, in PHAROS, for every directional component of the wave spectrum, the expected incoming wave angle must be determined per boundary. This is an iterative process, as the reflected wave, which can be an incoming wave for a different boundary, is influenced by the reflection coefficient. The r-DPRA tool is also used for this process. A script is written that calculates for every boundary the angle of the normal line at mid-boundary and consequently provides coordinates of a point directly in front of the boundary where the r-DPRA tool needs to find the waves direction. The results of one computation of this script is shown in Figure 7.4. The arrows indicate the incoming wave direction, the related value is the the direction with respect to the normal of the boundary.

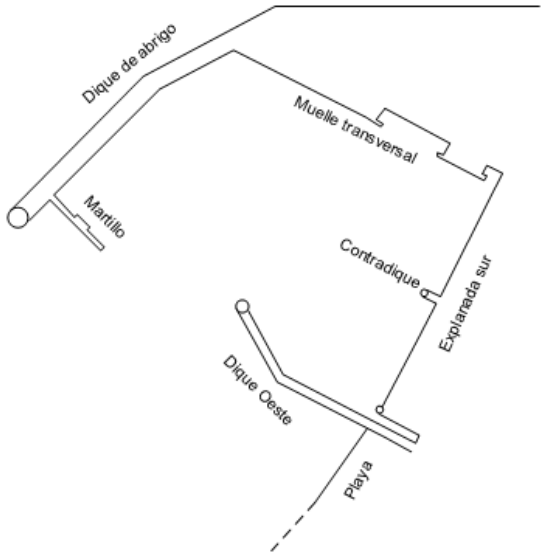

Figure 7.2: Characterization boundaries PHAROS model

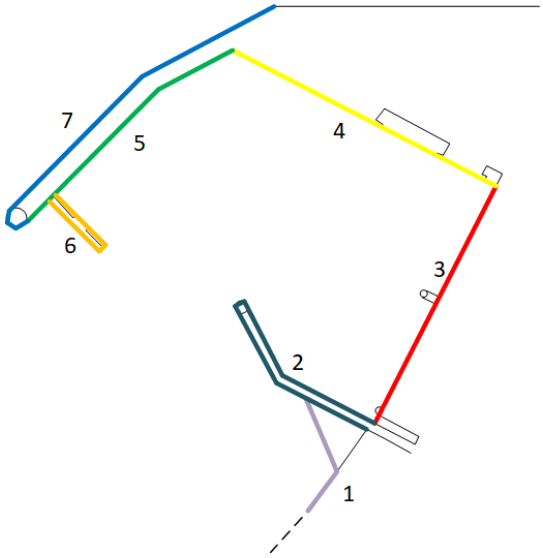

Figure 7.3: Boundary reflection definition PHAROS model

As the quay is subjected to waves from various directions and the reflection coefficient can only be set for one single direction, it is decided to take the most energetic wave component to be leading.

Reflection coefficients for the different boundaries within the model domain are determined by Aquatica, for their own model (Aquatica, 2019). These coefficients are used for this model as well, see Table 7.1.

Table 7.1: PHAROS Boundaries, related with Figure 7.3

Number	Name Boundary	Reflection coefficient
1	Playa	0.15
2	Dique Oeste	0.4
3	Explanada sur	0.4
4	Muelle transversal	0.9
5	Dique de abrigo (inside)	0.7
6	Martillo	0.9
7	Dique de abrigo (outside)	0.4

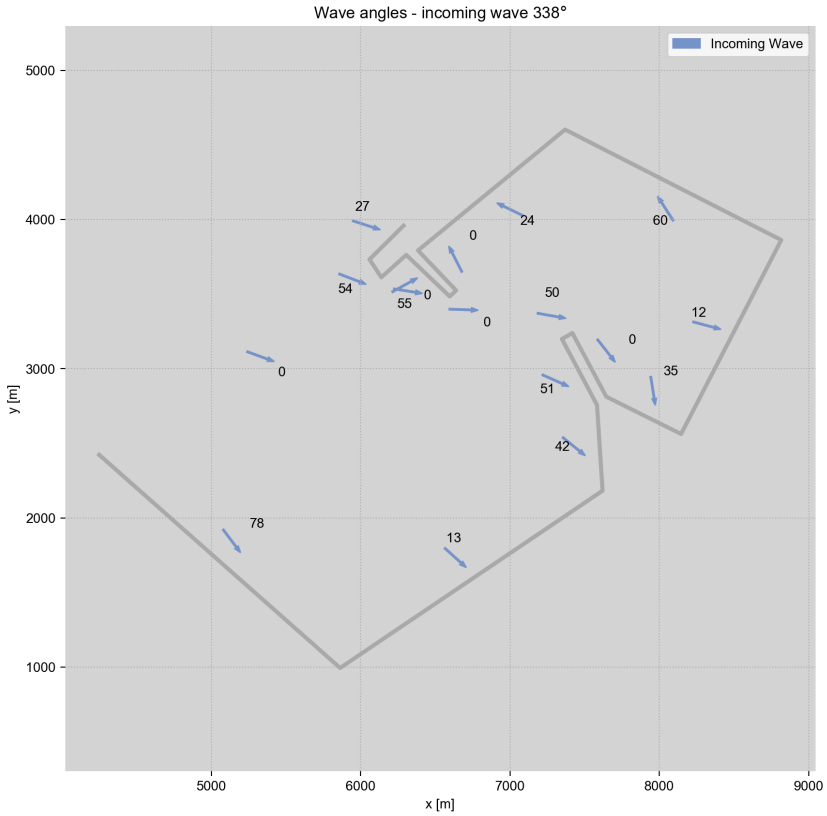

Figure 7.4: Boundary reflection determination, going to direction of the most energetic incoming wave, determined by the r-DPRA tool. Values indicate the angle of the wave direction with respect to the normal of the boundary

7.1.3. Grid

The grid has been made using the standard tool ACE/Gredit. A number of grid points per wave length is set at the beginning and the program places nodal points based on that parameter. The shortest wave to be modelled is used to calculate the wave length. The recommended number of grid points per wave length is 8. As a strategy, one can start with 2 or 4 grid points per wave length and then refine the grid by splitting grid cells into multiple cells. This strategy was used here as well. After some fine-tuning, the resultant grid consisted of 342,317 grid points and 684,200 cells.

7.1.4. DIFFRAC

In DIFFRAC, the hydrodynamic database of the vessel Aloe must be created. This starts with selecting the right linesplan. The dimensions are similar to the dimensions of the linesplan Versluis003, which was used in the model validation as well. An in-house developed MATLAB script of RHDHV is used to convert the linesplan into a 3D hull mesh. The mesh size is dependent on the water depth, to obtain a sufficient number of grid cells per wave length, which is depended of the wave number and thus water depth. This also means that for every water level, if still shallow water, a new DIFFRAC model must be set-up. The characteristic of the vessel Aloe and the linesplan it is based on (Versluis003) are presented in Table 7.2.
To add damping related to the quay wall, a damping lid is used in between the vessel and the quay. Here, 30% artificial damping is added to the model. The length of the lid is set to 2/3 of the vessels length, with the center in line with the mid line of the vessel.

Table 7.2: Vessel characteristics

	Aloe	**Versluis003**
Length (L_{oa}) [m]	179	187
Breadth [m]	28	29
Depth [m]	14	13
Draught [m]	8.5	10.95
L/B [-]	6.39	6.45
B/T [-]	3.29	2.65
CB [-]	0.77	0.79
Displ. [m^3]	32815	47032

7.1.5. aNySIM

In aNySIM, the bollards, mooring lines and fenders are modelled together with the vessel to form the mass-spring-system. The fenders installed at the quay are from the brand Prosertek and a single model is used: SC 1450 H quality grade C. In the fender data sheet of Prosertek (Prosertek, 2016), the capacity is found: The reaction force 1301 kN and the energy absorption 821 kNm per fender cone. Every fender system includes a board of 6.50 m height and 2.95 m width, supported by two cone fenders in a vertical line, see Figures 7.5 and 7.6.

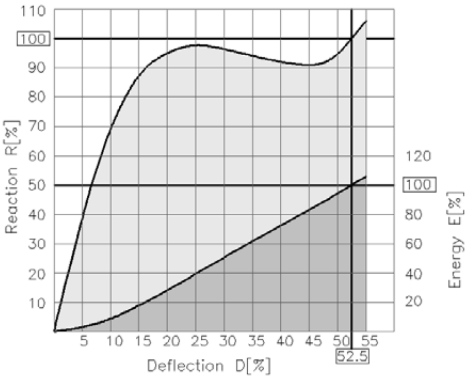

Figure 7.5: Deflection curve cone fender (Prosertek, 2016)

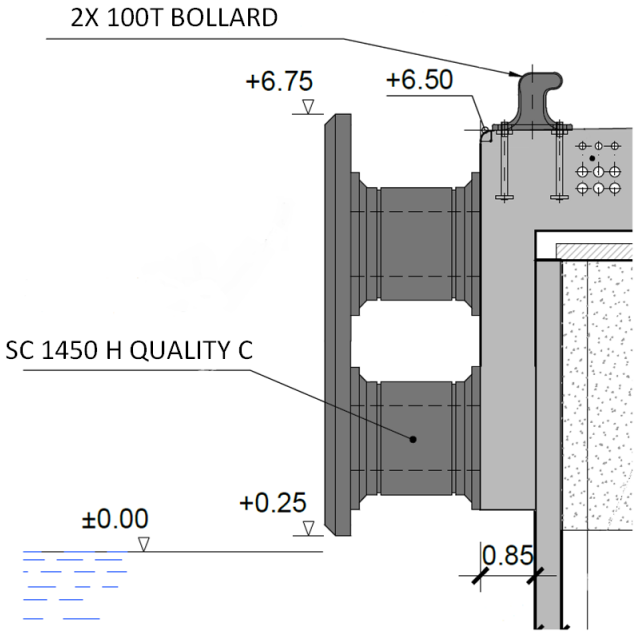

Figure 7.6: Quay and fender design (Port Authority of A Coruña, 2014)

Right above every fender, a bollard is found with maximum capacity of 200t. The vessels mooring lines are attached to the bollard according to the mooring arrangement shown in Figure 7.7. To determine the position of the fairleads on deck, a typical bulk carrier deck plan is scaled to the target length and width. During the measurement campaign, the mooring configuration was noted. Therefore, it is known which fairleads are linked to which bollards.

The mooring line characteristics are estimated based on similar bulk carriers. In Figure 7.8 a photo is shown of the mooring lines. From that photo, it is concluded that the material of the mooring lines is polyester. In another DMA report, a similar size bulk carrier was modelled with polyester mooring lines. The diameter assumed there was 80 mm with a MBL (Mean Breaking Load) of 900 kN. The vessel Aloe is modelled with the same mooring lines, but a sensitivity analysis is done for the mooring lines.

The starting position of the vessel is estimated based on the photos made during the measurements and

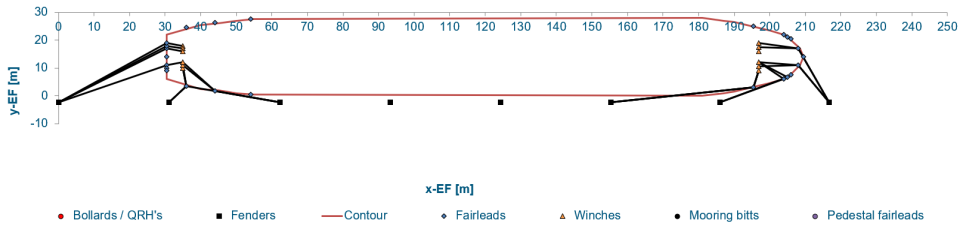

Figure 7.7: Mooring configuration Aloe used for the aNySIM model

Figure 7.8: Photo of the mooring of the Aloe at the start of the measurements

based on a top view of a different but similar size Bulk Carrier that has been moored at the same quay. The distance along the quay between the rear side of the vessel and the first bollard is found to be roughly 30 meters.

7.2. Base Case

7.2.1. Wave Climate

Table 7.3: PHAROS Wave climate input, Base case

Quantity	Symbol	Value
Significant Wave Height	H_s	2.41 m
Peak Period	T_p	14.3 m
Peak Direction (buoy coordinates)	Dir_p	312°
Peak Direction (PHAROS coordinates)	Dir_p	318°
Peak Enhancement Factor	γ	3.3
Directional spreading parameter	m	12
Water level	-	+1.05 m
Number of frequencies	-	9
Number of directions	-	7

In Table 7.3 the wave climate imposed as boundary condition for the PHAROS computations are presented for the base case. Most parameters are know from the measurements, however, some must be assumed. The peak enhancement factor and directional spreading are assumed, based on literature values. The average peak enhancement factor found during the JONSWAP research (Hasselmann, 1973) was $\gamma = 3.3$. The directional spreading factor is something that can be measured, however, the wave buoy offshore of La Coruña

does not measure the directional spreading. For swell waves it is known that the directional spreading is generally smaller than for wind waves and Goda found a spreading factor of $s = 70$ for the so-called *cos2s-spreading function*. This function reads:

$$D(\theta) = B \cdot cos^{2s}(\frac{\theta - \theta_{main}}{2}) \tag{7.1}$$

However, Goda's value is used for engineering purpose, which means being on the safe side, as the energy is very concentrated around the peak direction. This leads to the greatest impact on structures.

For this model, more spreading can lead to more waves penetrating into the port basin, and there it is not considered conservative to use low directional spreading. The spreading function used by PHAROS, *cosm-spreading function*, equals:

$$D(\theta) = B \cdot cos^{m}(\theta - \theta_{main}) \tag{7.2}$$

Deltares typically uses $s = 2$ for waves with $T_p < 10s$ and $s = 7$ for $T_p > 10s$. Rewritten for the cosm-function these values are $m = 1$ and $m = 3$ respectively. However, the governing swell conditions have very large travel distances due to the exposure to the Atlantic Ocean and a T_p in the range of 14 to 19 s, therefore less spreading is expected than these values. To find a balance between the Goda engineering values and the Deltares assumptions, the m value is set to 12, which implies a 1-sided standard deviation of approximately 16°. Additionally, a sensitivity analysis is done to assess the influence of this spreading factor.

With the pre-processing step, the 2-dimensional wave spectrum is discretized. This is based on a equal weight approach for the frequency spectrum and a equal step size approach for the angular spectrum. For now, a directional resolution of 10° is used, and every 10% of the cumulative energy distribution the wave period is selected. See Figures 7.9 and 7.10 for the descritization applied.

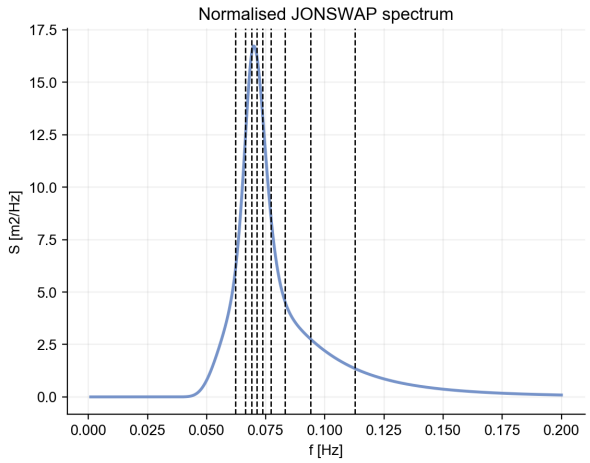

Figure 7.9: Discreet frequencies base run

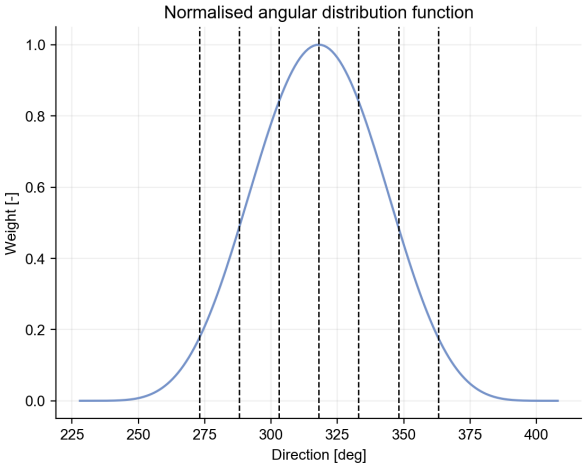

Figure 7.10: Discreet directions base run

As mentioned earlier, the tidal level was measured by the tidal gauge in the port basin. Time series are found on the website of the National Port Authority of Spain (Port Authority of A Coruña, 2019b). At the modelled moment in time, 10:40h, the water level was found to be 1.05 m.

7.2.2. Results Computations and Comparison

In this section, the results of the base case are presented. In Figure 7.11, the computed wave field is presented for the base case. It can be seen that for the primary waves, the port basin is sheltered, leading to significant wave heights in the order of 10's of centimeters.

In Figure 7.12, the output of the r-DPRA tool at the berth is presented. Every dot represents a component. The components reflected by the quay are filtered out. These components are directly imposed in aNySIM to

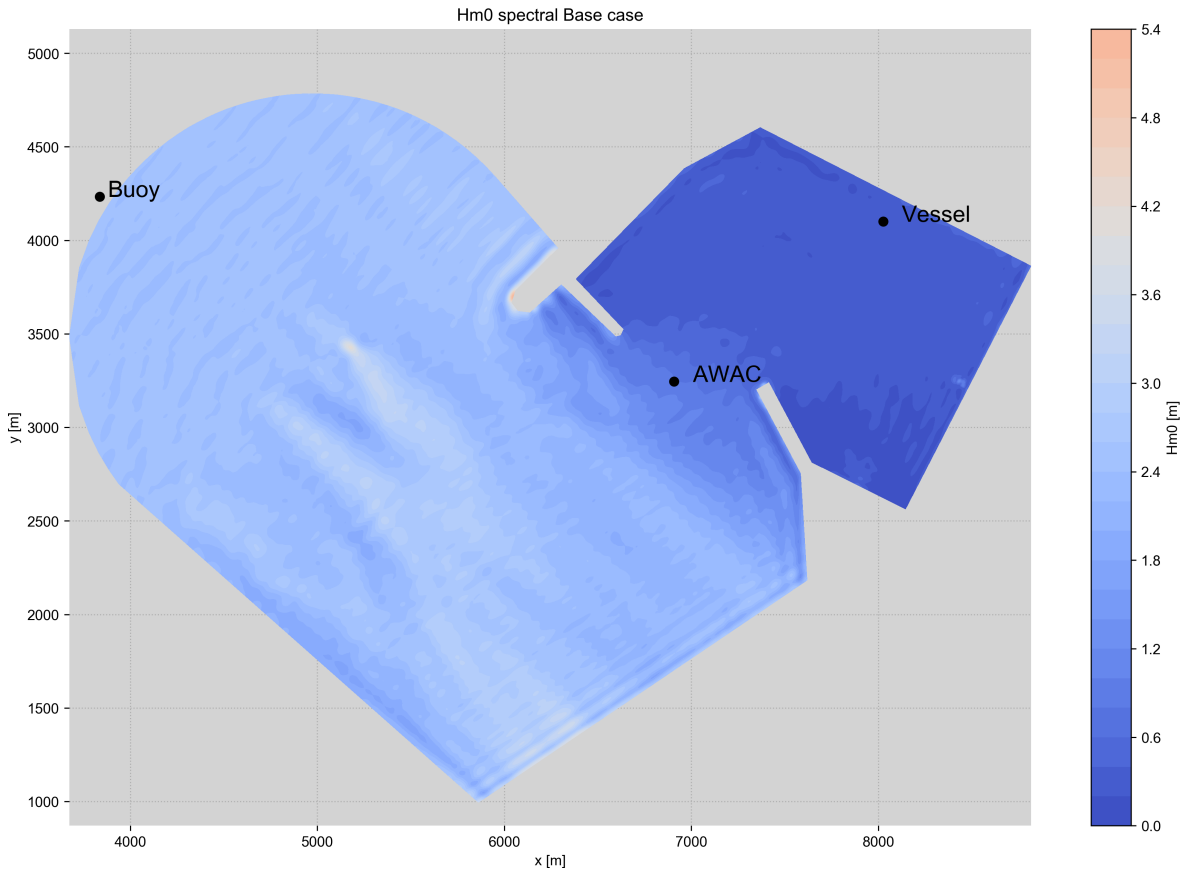

Figure 7.11: Weighted H_{m0} PHAROS, Base Case

model the related ship motions.

The base case was run with wave breaking and bottom friction disabled. It was expected that these processes don't play a significant role in the considered model. To check, a run was done with both enabled and the results show no significant influence of enabling wave breaking and bottom friction.

The weighted H_{m0} found by PHAROS on the location of the quay was 0.25 m. This includes the reflected components that are filtered out for the aNySIM model. Therefore for comparison on the level of H_{m0}, the reflected components must be taken into account as well. The weighted H_{m0} found after the rDPRA analysis is 0.33 m. When the reflected components are filtered out, the H_{m0} found by the rDPRA tool is 0.19 m. In Table 7.4, the conditions are summarized.

Table 7.4: Wave field at quay, Base Case

	Unfiltered	Filtered
H_{m0} PHAROS	0.25 m	-
H_{m0} r-DPRA	0.33 m	0.19 m

An extra check is done to help understand the difference between the H_{m0} directly from PHAROS and the one found by the r-DPRA tool. Close to the entrance, the r-DPRA analysis is done in two ways:

- All found components included. The weighted H_{m0} equals 2.91 m.
- Only the components belonging to the incoming wave field. The weighted H_{m0} equals 2.42 m.

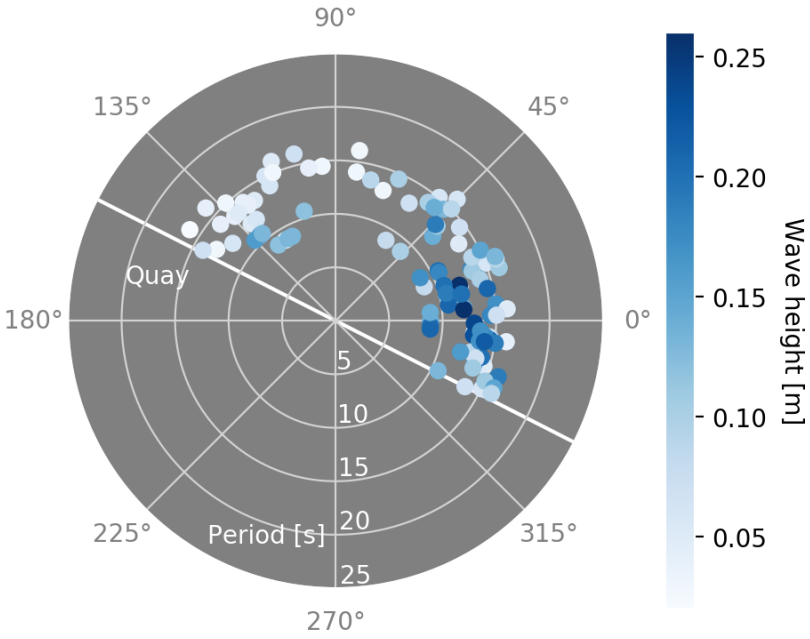

Figure 7.12: r-DPRA output Base Case, with the dots representing the going-to direction of the wave component

From this, it can be concluded that the overestimation of the $Hm0$ is originated from the side lobes found by the r-DPRA tool, these are non-existent components.

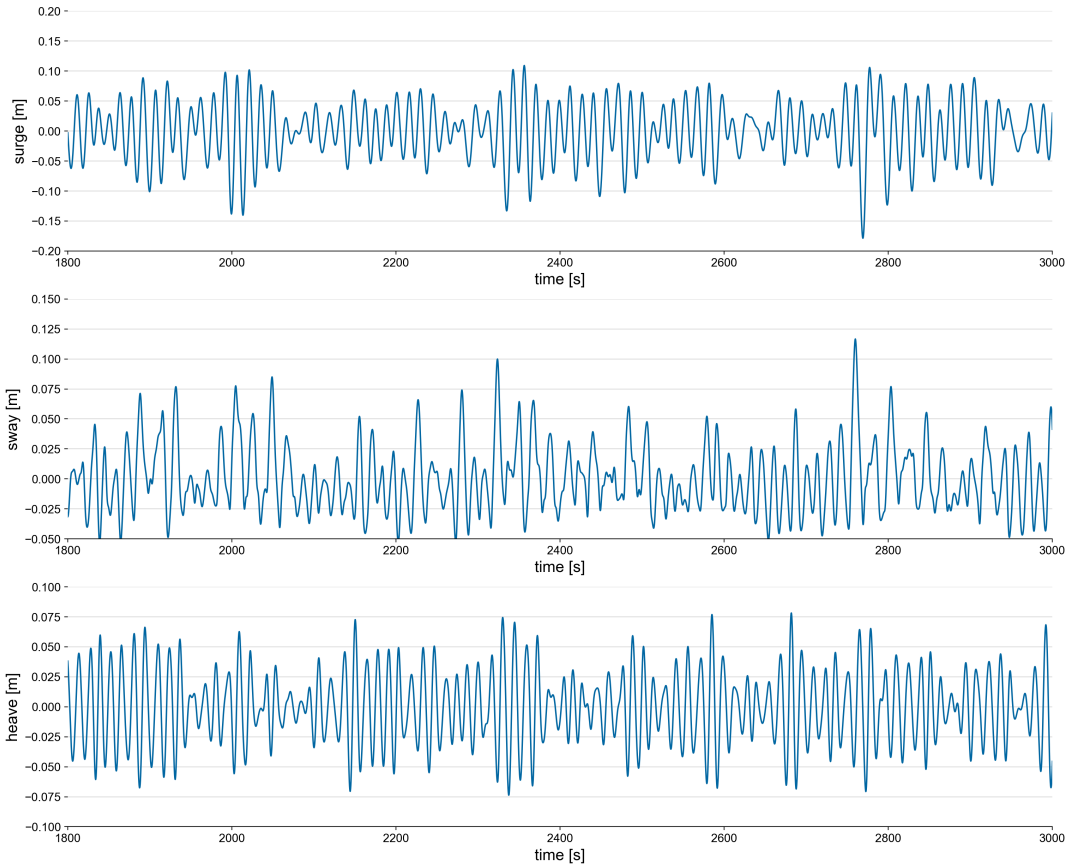

Figure 7.13: Modelled translations of the Base Case

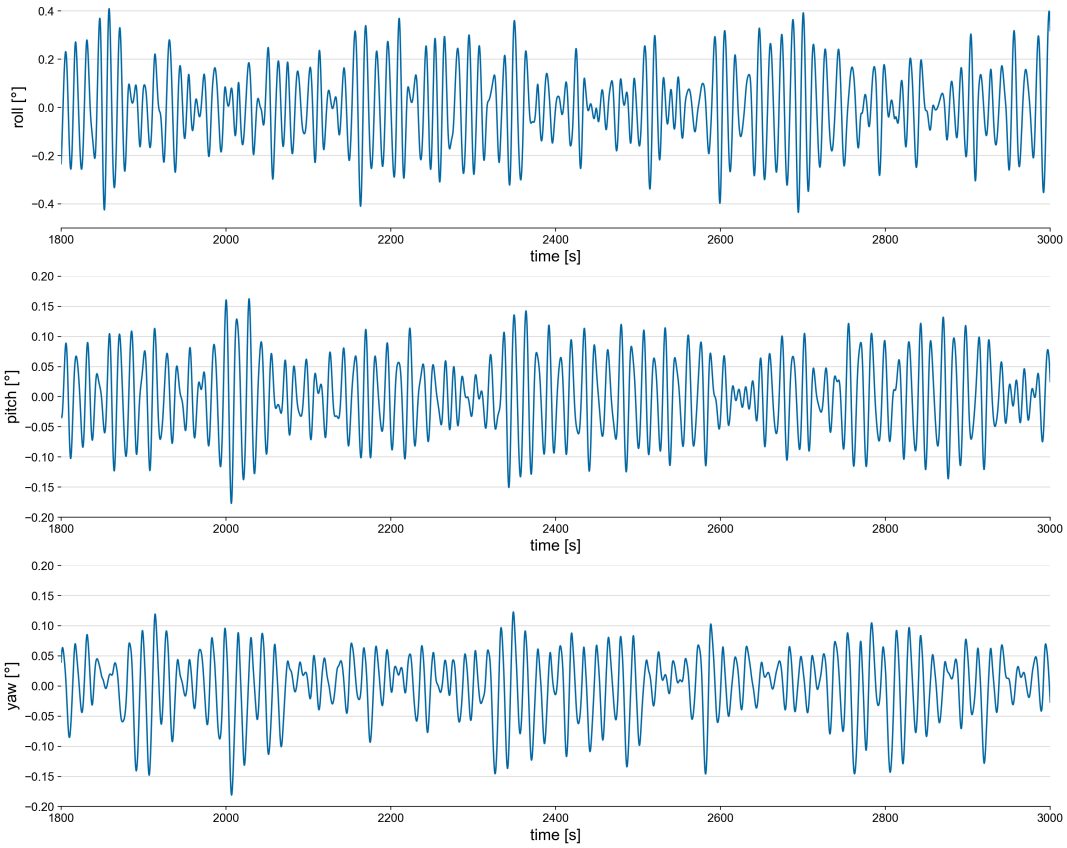

Figure 7.14: Modelled rotations of the base case

In Table 7.5, the results of the computation of the base case are presented. Both the peak-peak values as the significant motions are shown. The peak-peak motion is the difference between the minimum modelled value and the maximum modelled value while the significant motion is calculated by taking the average of the third highest "waves".

Table 7.5: Modelled Peak-Peak and significant motions, Base case.

Motion	**Peak-Peak**	**Significant**
Roll	1.14°	0.70°
Pitch	0.41°	0.26°
Yaw	0.37°	0.20°
Surge	0.35 m	0.19 m
Sway	0.27 m	0.12 m
Heave	0.23 m	0.14 m

In Table 7.6, the results of the computation of the base case are compared with the measurements on the level of statistics. It can be seen that yaw is not modelled accurately and this motion is significantly underestimated by the numerical model. It must be noted that the measured yaw angle is particularly high compared with the other rotations. Surge is also underestimated significantly, while the sway is more accurately modelled based on the absolute difference. Heave, however, is not modelled very accurately either.

Comparing the time series of the surge motion, in Figure 7.15, it can clearly be seen that the long wave pattern found in the measurements is not accurately modelled. However, in the sway time series, the long wave pattern is more visible in the numerical model results. Comparing the rotation time series (Figure 7.14), the primary wave forcing is clearly visible just like in the measurements. Moreover, large differences are found in surge, yaw and heave. It must be noted that the measured yaw is relatively large compared to other motions. To conclude, the modelled motions of the base case do not show good resemblance with the measured motions, both in terms of statistics as in time series.

Table 7.6: Modelled significant motions compared with measurements base case

Motion	**Measured**	**Modelled**	**Compared with base**	
Roll	1.21°	0.70°	-42%	−0.51°
Pitch	0.19°	0.26°	+36%	+0.07°
Yaw	2.29°	0.20°	-91%	−2.09°
Surge	0.64 m	0.19 m	-70%	-0.45 m
Sway	0.07 m	0.12 m	+71%	+0.05 m
Heave	0.42 m	0.14 m	-67%	-0.28 m

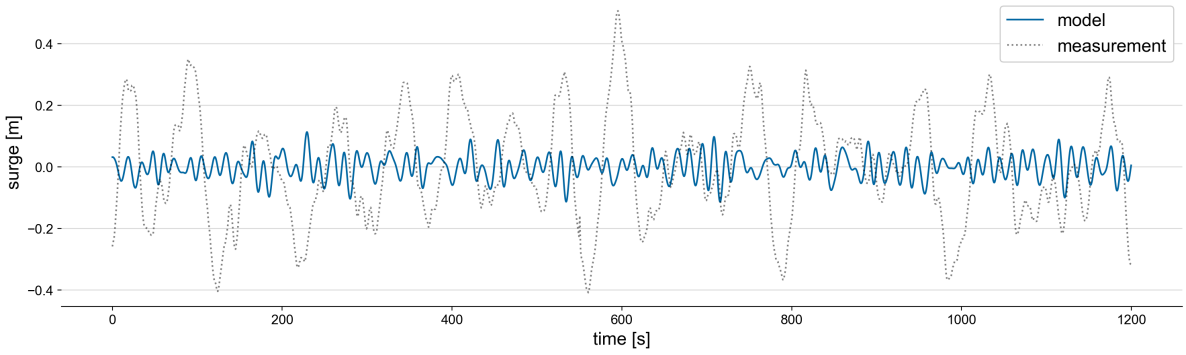

Figure 7.15: Comparison time series base case

7.3. Heavy Case

7.3.1. Draft estimation

Looking at the time series of the significant wave height and peak period, the simulated base case can be considered as a moderate wave climate. In order to check the model chains performance for a more severe wave climate, a different moment in time is selected while the same vessel, the Aloe, was moored. On February 20th, the same day as the base situation, at 18:00h much heavier wave conditions were present. The offshore significant wave height was around 3.7 m, the peak period 16.7 s and the peak direction 316 degrees. During high tide, the vessels position was higher with respect to the quay. The base situation had a water level of C.R. +1.05 m while the heavy situation has a water level of C.R. + 3.43 m, this means the water level was 2.38 m higher. The heave time series data show a shift in mean position from 0 m to 4.6 m, see Figure 7.16. As mentioned, 2.38 m of this is caused by the tidal difference, which leaves 2.22 m caused by the unloading of cargo in the time interval. This leads to a new draught of the vessel of $8.50m - 2.22m = 6.28m$. The change in draught can be seen when comparing different frames of the heave camera, see Figures 7.17 and 7.18

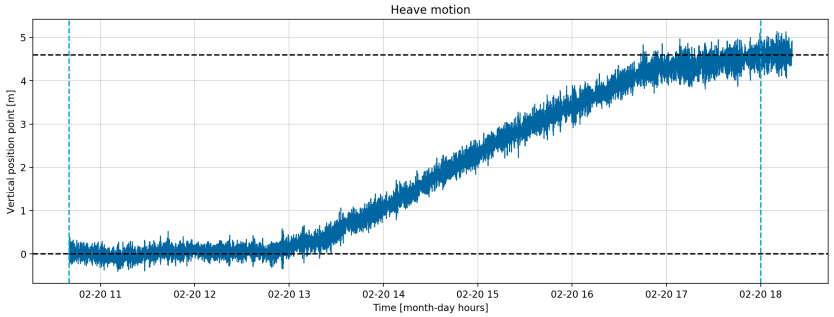

Figure 7.16: Unfiltered heave measurements Aloe

Figure 7.17: First frame of the measurements of the VTS camera

Figure 7.18: Last frame of the measurements of the VTS camera

With this new draft and new water level, a DIFFRAC run is done to create a new hydrodynamic database for the aNySIM run. A new hull mesh must be made to account for the new draught of the vessel. The KG-value becomes 9.65 m and the mass of the vessel 24.382t. The radii of gyration are kept constant, as the previous values were estimated based on rules of thumb that were solely based on the beam and length of the vessel.

In PHAROS, a new run is done with a different wave climate, see Table 7.7. The H_s of the JONSWAP spectrum equals 3.7 m, the T_p 16.7 s and the Dir_p 314 degrees. The directional spreading factors remains $m = 12$ and the peak enhancement factor $\gamma = 3.3$. The number of discreet frequencies modelled by the PHAROS model to represent the measured wave spectrum is equal to 10. The directional resolution is set to 15 degrees, which leads to 5 directions.

Table 7.7: PHAROS Wave climate input, Heavy case

Quantity	Symbol	Value
Significant Wave Height	H_s	3.70 m
Peak Period	T_p	16.7 m
Peak Direction (buoy coordinates)	Dir_p	316°
Peak Direction (PHAROS coordinates)	Dir_p	314°
Peak Enhancement Factor	γ	3.3
Directional spreading parameter	m	12
Water level	-	+3.45 m
Number of frequencies	-	10
Number of directions	-	5

7.3.2. Results Computations and Comparison

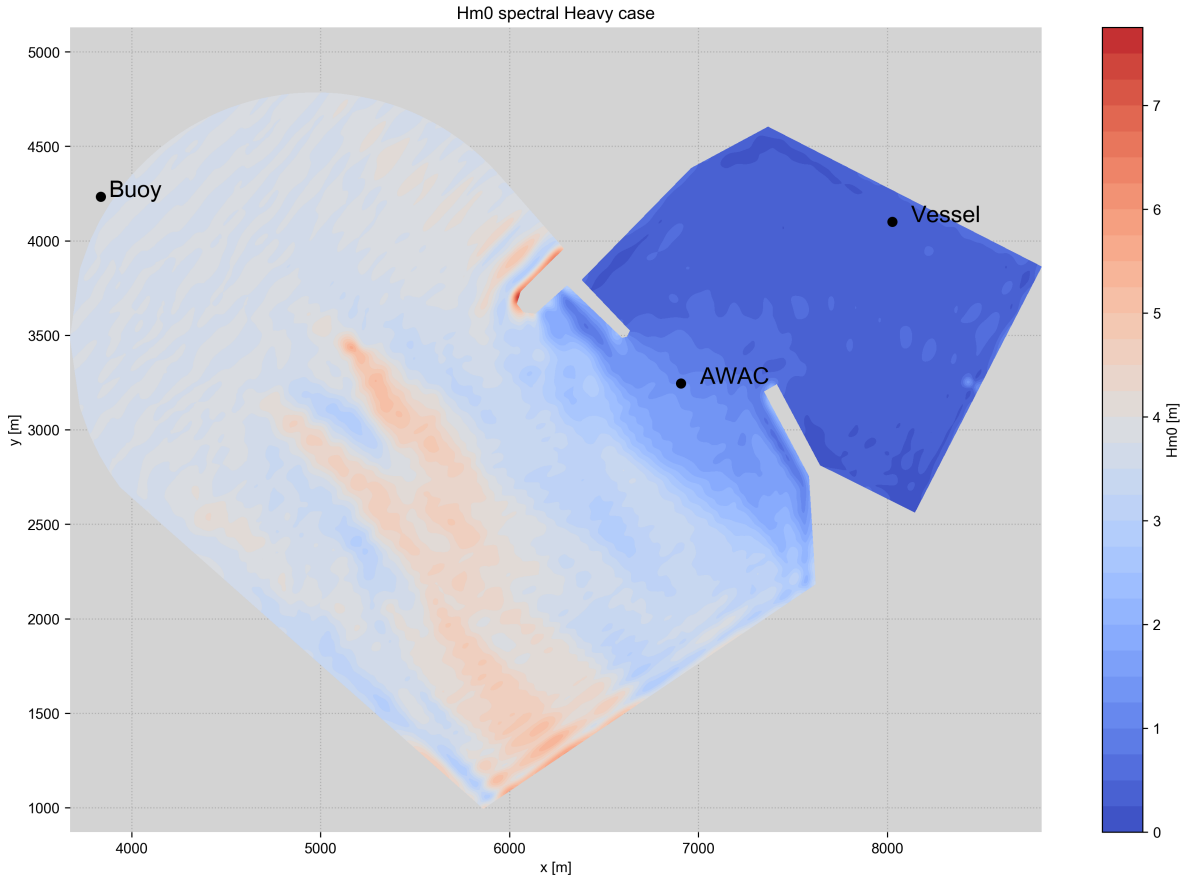

Figure 7.19: Weighted Hm0 PHAROS, heavy case

The H_{m0} directly found from PHAROS equals 0.41 m, while the rDPRA tool finds an H_{m0} of 0.59 m. When the quay wall is taken into account and the reflected components are filtered out, the r-DPRA finds a H_{m0} equal to 0.35 m. The H_{m0} computed by PHAROS is shown for the whole domain in Figure 7.19. It can be seen that most of the energy does not penetrate into the port basin, with a high gradient in wave energy just in front of the port entrance.

As an extra verification step, the measured AWAC wave height is compared to the modelled wave height in PHAROS. In Figure 7.20, the hourly measured wave heights of the AWAC are presented for the full duration of the mooring of the vessel Aloe. Due to missing data (due to a battery change), only the heavy case can be compared with AWAC data. The moment considered in the heavy case (the 20th of February, 18:00h), the

AWAC data show a measured H_{m0} of 1.30 m.

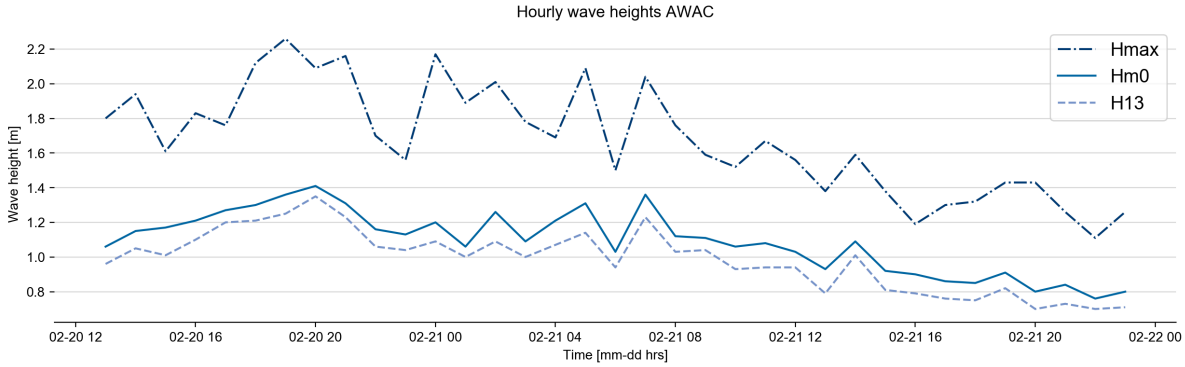

Figure 7.20: Hourly wave height statistics, measured by AWAC

In PHAROS, a weighted H_{m0} is found of 1.23 m, which is considered a good match and provides confidence in the wave model results. Important to see is that the at the location of the AWAC a steep gradient in wave height is found, and therefore the value is highly sensitive to the exact location of the AWAC.

Then, the r-DPRA analysis resulted in the components presented in Figure 7.21. These components are used as input for the aNySIM simulations and are passed through to aNySIM in a list of components.

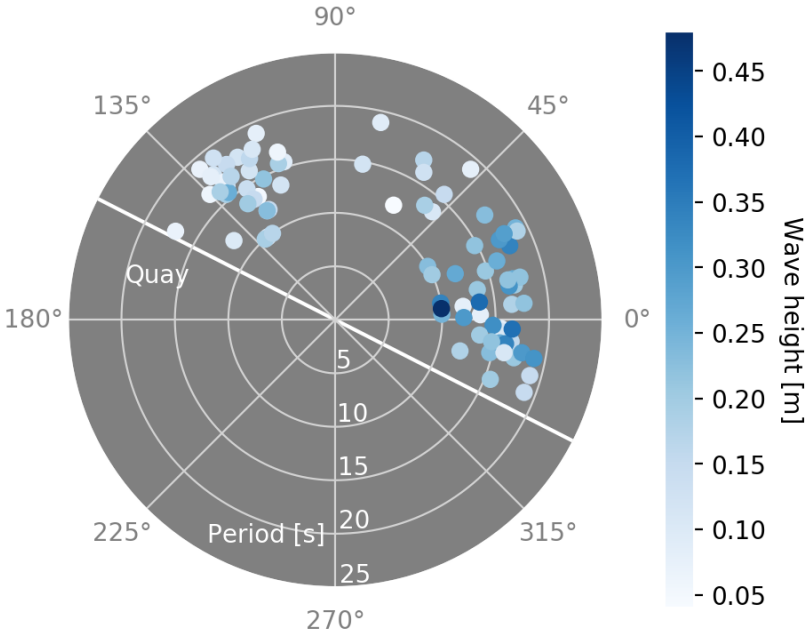

Figure 7.21: r-DPRA output Heavy Case

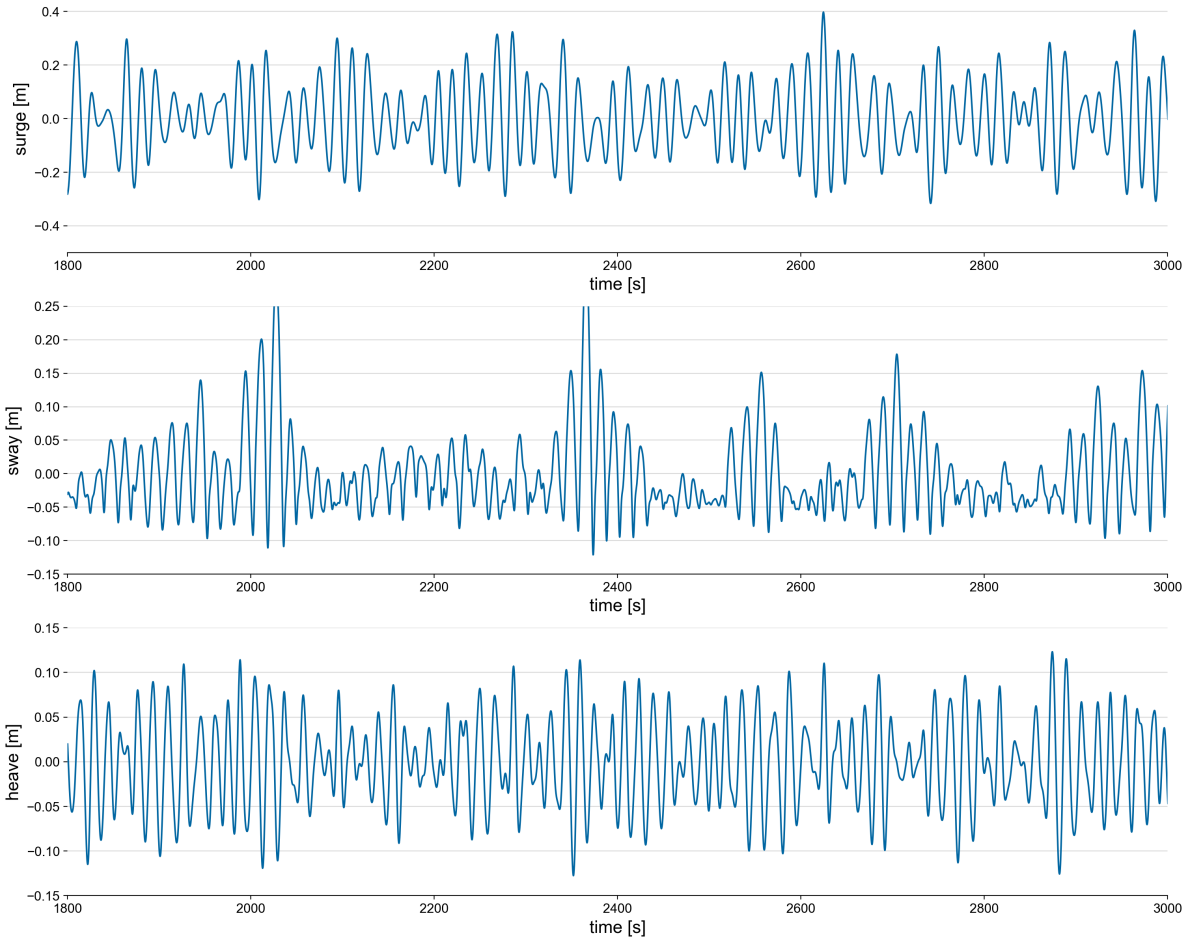

Figure 7.22: Modelled translations of the heavy case

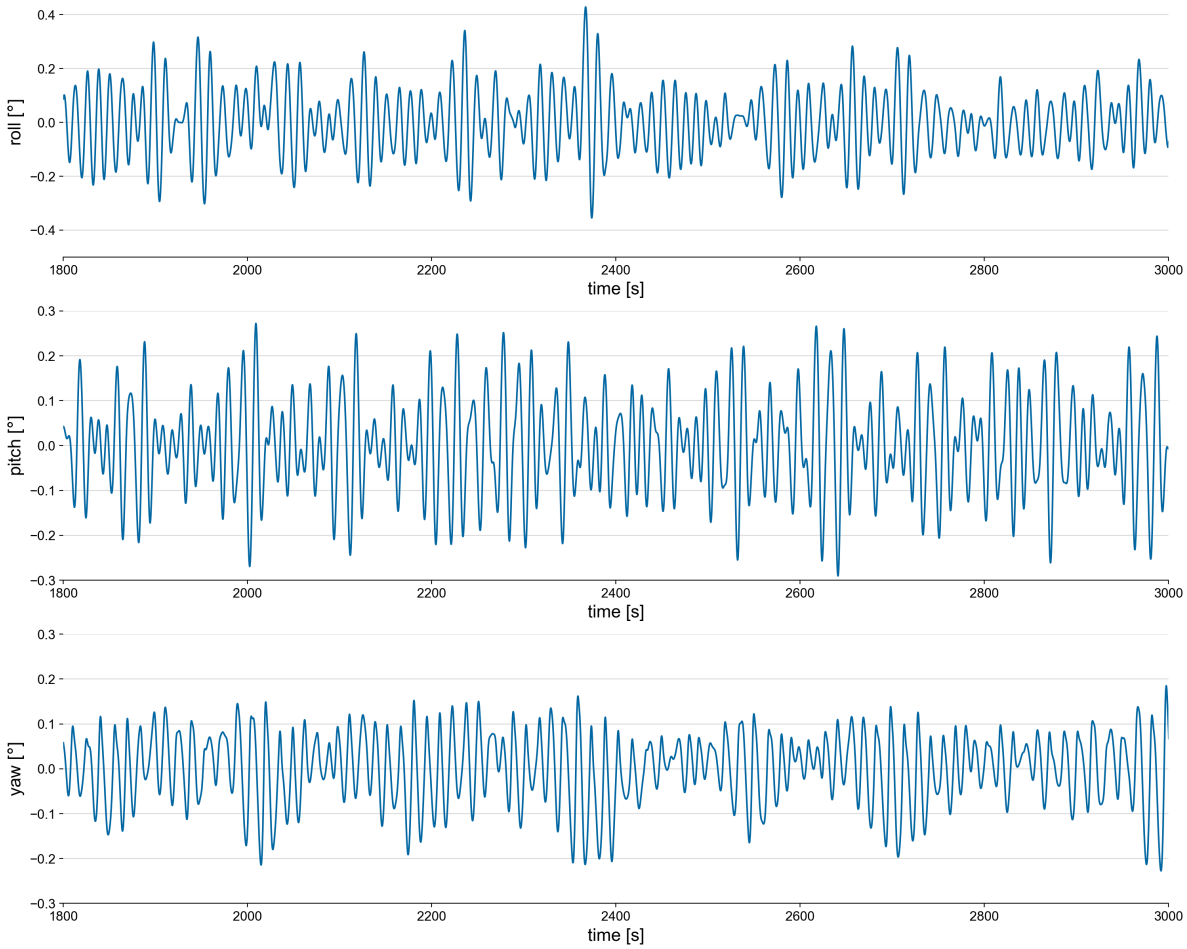

Figure 7.23: Modelled rotations of the heavy case

The modelled time series are shown in Figures 7.22 and 7.23. The same holds as for the base case; the low frequency pattern is not visible in the surge and sway, whereas the measurements do show a low frequency pattern. In Table 7.8, the statistics of the modelled motions are shown.

Table 7.8: Modelled peak-peak and significant motions Heavy case

Motion	Peak-Peak	Significant
Roll	1.07°	0.54°
Pitch	0.71°	0.40°
Yaw	0.85°	0.39°
Surge	0.99 m	0.57 m
Sway	0.63 m	0.31 m
Heave	0.44 m	0.27 m

In Table 7.9, the comparison is made between the model results and the measurements. Opposed to the base case, the heavy case is more accurate for some motions. The surge and the sway are within 0.26 m and 0.06 m respectively, which is more accurate than in the base case. The relatively high yaw angle seems far off as well, just like the base case. The pitch has a relative error of 74%, which seems high, but it must be noted that the absolute error is only 0.17°. The smaller the values, the larger the relative errors.

Overall, the heavy case performs slightly better for surge and sway, compared with the base case. The yaw motion and the heave motion are, just like with the base case, relatively inaccurate. A visual comparison for the time series is shown in Figure 7.24. It can be seen that the difference in amplitude is relatively small, however, the long wave pattern found in the measurements is not found in the modelled motions.

Table 7.9: Modelled significant motions compared with measurements heavy case

Motion	Measured	Modelled	Compared with heavy	
Roll	0.90°	0.54°	-40%	−0.36°
Pitch	0.23°	0.40°	+74%	+0.17°
Yaw	1.72°	0.39°	-77%	−1.33°
Surge	0.83 m	0.57 m	-31%	-0.26 m
Sway	0.37 m	0.31 m	-17%	-0.06 m
Heave	0.72 m	0.27 m	-63%	-0.45 m

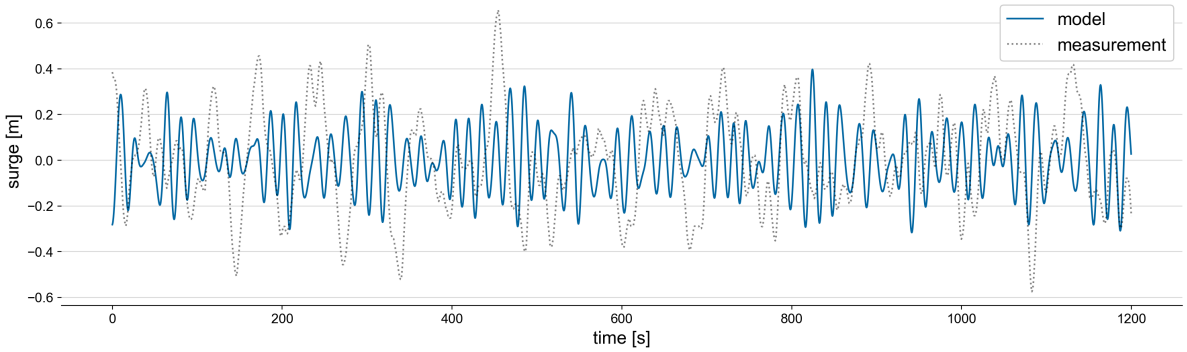

Figure 7.24: Comparison time series heavy case

7.4. Free Long Waves

7.4.1. Long waves

As discussed in Chapter 2, long waves can be of major importance when it comes to moored ships in ports. This long wave, in a bound state, exists due to the change of mean water level on the scale of wave groups.

The lower wave groups have a higher 'mean' water level than the higher wave groups, see Figure 7.25 for an illustration of the principle (Journée and Massie, 2001). This second order effect leads to a so-called bound long wave. Its wave period typically ranges form 30 s to 300 s. As soon as waves start to break, this bound long wave is partially released, as the groupiness that induces the bound long wave is reduced. Once released, it becomes an individual wave, not longer travelling with the velocity of the wave group. As their wave lengths are in the order of hundreds to thousands of meters and their wave heights being only in the order of centimeters to decimeters, the free long waves are fully reflected by most structures and even mildly sloping beaches nearly fully reflect these free long waves. Moreover, these waves can fully diffrac around structures and into port basins. Both harbour resonance as ship resonance can be a consequence of these long waves.

The horizontal degrees of motions (surge, sway and yaw) of moored ships typically have a low natural periods, due to the mooring lines, fenders and little damping in the horizontal plane. Wave periods of both the bound long wave as the free long wave can be in the range of the natural periods of the system, leading to resonant behaviour of the moored ship. Because of this resonance, low wave forces can generate high ship motions and mooring line forces. Although the long waves in port basins typically have wave heights of 5 to 15 cm, the subsequent ship motions can become problematic.

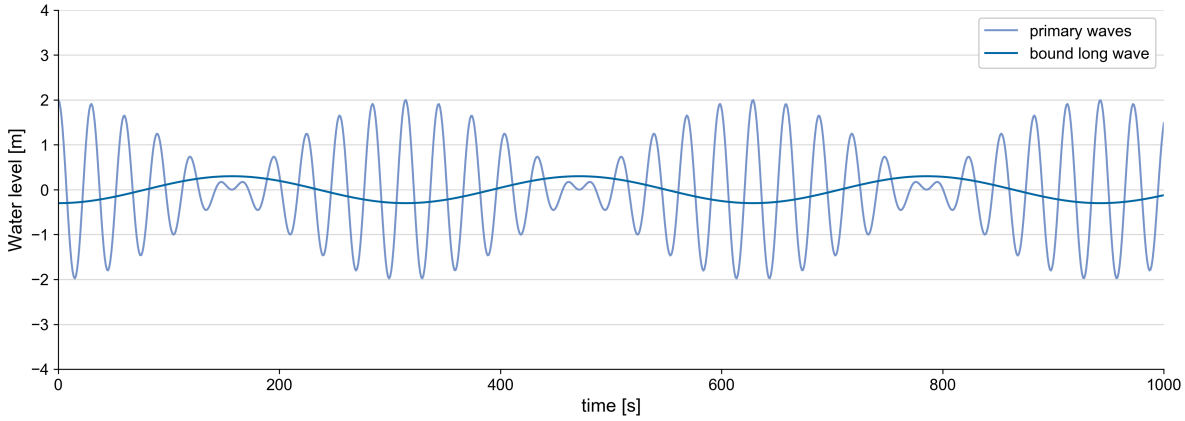

Figure 7.25: Principle of bound long wave generation, a higher 'mean' water level when the primary waves are low energetic

7.4.2. Approach

Because PHAROS is a linear wave model, bound long waves are not taken into account. DIFFRAC, however, does calculate the associated bound long wave that corresponds with the incoming primary waves. As the wave height next to the quay is relatively low, in the order of 0.3 m and the bound long wave height scales with the primary wave height to the power 2, the bound long wave next to the quay is relatively small in wave height. In general, bound long waves play a significant role in offshore structures and exposed jetties. Port basins are usually sheltered from the primary waves and therefore not subject to high bound long waves.

In port basins, however, the free long waves can cause large ship motions. As wave breaking happens outside of the port basin, the associated wave heights of the primary waves can be in the range of meters. The bound long wave is much higher when released than inside the port basin and shoaling can cause the wave height to even increase.

Therefore, to get more understanding of the hydraulics inside the port basin, the free long waves are schematized and modelled by PHAROS separately. Then, they are added to the list of primary waves that is inserted into the aNySIM ship motion simulation to assess the effect on the ship motions.

The offshore wave conditions are described by a JONSWAP spectrum, this contains the energy distribution of the primary waves. Associated with the spectrum there is also energy at the low frequencies due to the bound long wave. The water depth, however, is an important parameter for this low frequency wave energy. Therefore, in this approach, a water depth is chosen at which the first primary waves are expected to break in front

of the basin entrance. There, the bound long wave is released as a free long wave. A research done by Deltares (Van Der Hout et al., 2012) describes an estimation for the infra-gravity waves that is used in this method as well. For a given set of offshore wave conditions, the low frequency wave energy spectrum is calculated by Deltares and provided for this research, see Figure 7.26. The results are presented in Table 7.10.

As long waves are reflected more easily, the reflection coefficients must be adjusted with respect to the primary wave reflection coefficients. The South-West sea side is still considered an open boundary and therefore the reflection coefficients is maintained at zero. The beach coefficient is set to 80%, as some energy is expected to dissipate there. All other boundaries must be set to almost fully reflective 95-100% reflection, according to De Jong et al. (2016). In this case, 100% was chosen.

Table 7.10: Long wave assesment parameters

	Base Case		**Heavy Case**	
Parameter	Primary waves	LF waves	Primary waves	LF waves
H_s	2.41 m	0.05 m	3.70 m	0.15 m
T_p	14.3 s	88 s	16.7 s	102 s
Dir_{mean}	318°	318°	314°	314°
m	12		12	
γ	3.3	-	3.3	-
water depth	-	29 m	-	29 m

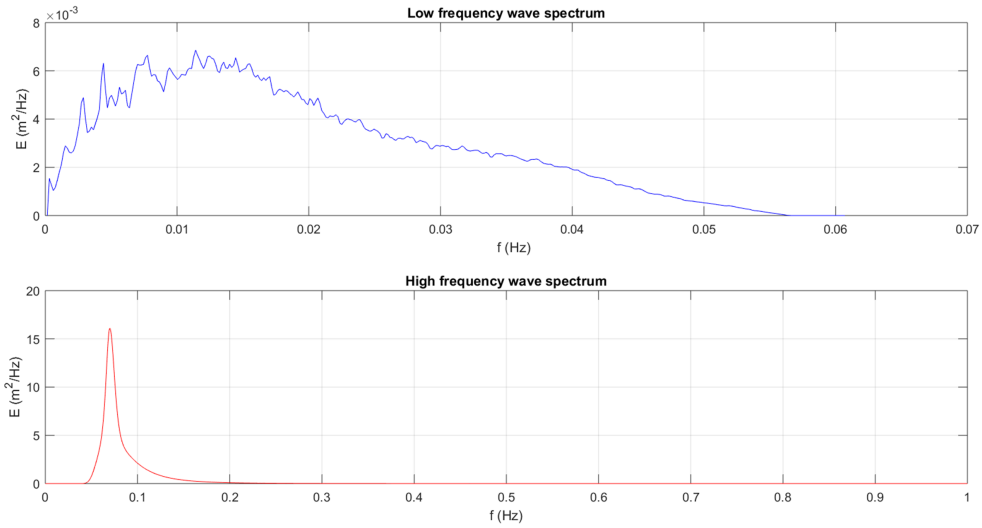

Figure 7.26: In the top panel the LF wave spectrum of the base case. The lower spectrum shows the primary JONSWAP spectrum on which it is based

A polynomial is fitted through the Low-Frequency spectrum to have a continue function. Then, the same procedure is used as for the discretization of the primary waves: energy is divided over bins of variable width. In this case, the number of discreet frequencies is set to 4, while the directional resolution equals 30 degrees. This leads to 12 separate runs in PHAROS. In Figures 7.27 and 7.28, the discretization is shown.

Then, the r-DPRA tool finds the LF components within the port basin and a list of them is added in aNySIM to find the related ship motions. The long waves are added to the primary waves as computed before. Therefore, the plotted results include both primary and LF wave excitation of the vessel.

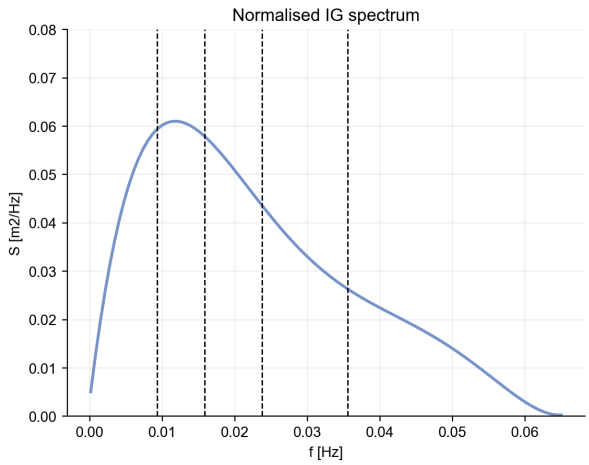

Figure 7.27: Discreet frequencies LF spectrum, Base Case

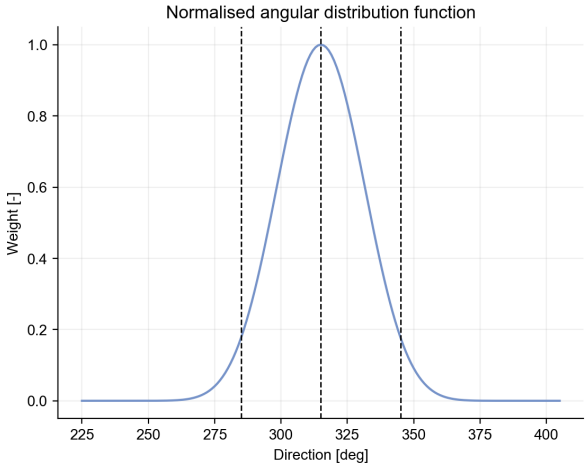

Figure 7.28: Discreet directions LF spectrum, Heavy Case

7.4.3. Results computation and comparison

In Figure 7.29, the time series of the computed surge and sway motions are plotted. These motions are the most influenced by the long wave excitation. From the time series, it can clearly be seen that the long wave forcing is present. In Table 7.11, the statistics are shown and compared with the measurements.

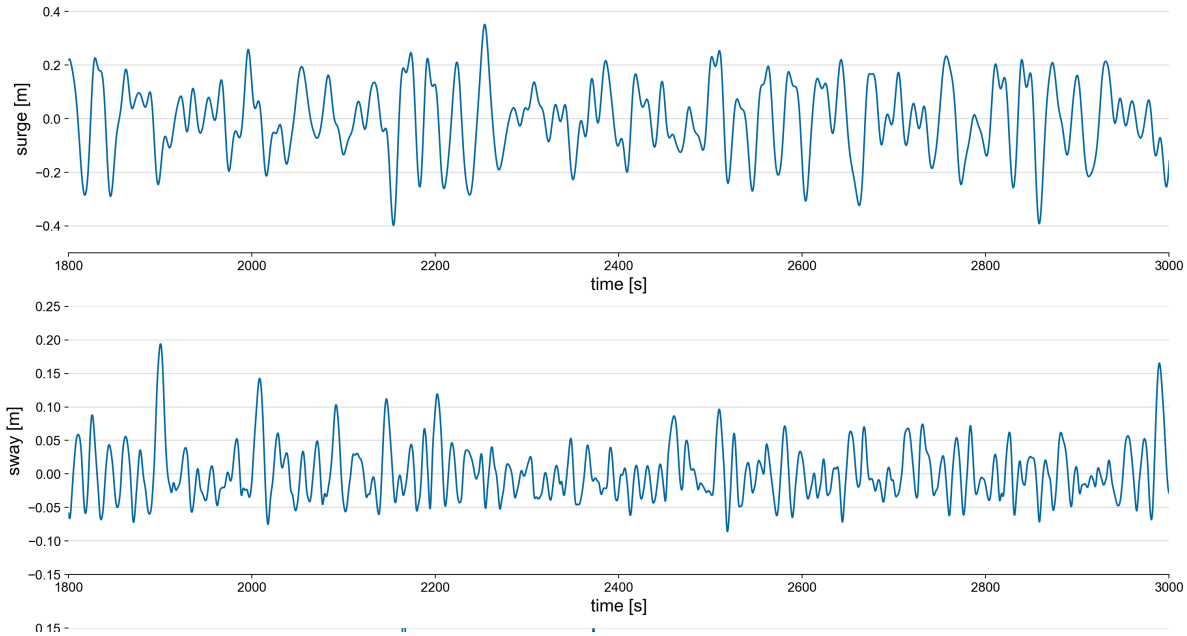

Figure 7.29: Modelled translations Base Case, including the added free long waves

If the time series are compared with the time series of the measurements, more resemblance is found because of the long wave pattern. Moreover, the statistics show an improvement for all motions except the sway. Most improvement is found for surge (from 0.45 m to 0.15 m off) and heave (0.28 m to 0.18 m off), see Table 7.11. The improvement in surge can be explained by the presence of long waves. As can be seen in the time series in Figure 7.30, the LF pattern is found that is not visible in the time series of the base case without the addition of long waves. The increase of heave motion can be explained because wave energy is added to the primary wave field, so that the water level amplitude in general increases. As the heave was underestimated, the underestimating now becomes smaller. Yaw, finally, is still significantly underestimated.

Table 7.11: Modelled significant measured motions, modelled motions and modelled with LF wave motions. Comparison between measured motions and modelled + LF waves motions

Motion	Measured	Modelled	Modelled + LF	Compared with measured
Roll	1.21°	0.70°	0.70°	−0.51°
Pitch	0.19°	0.26°	0.27°	+0.08°
Yaw	2.29°	0.20°	0.23°	−2.06°
Surge	0.64 m	0.19 m	0.79 m	+0.15 m
Sway	0.07 m	0.12 m	0.15 m	+0.08 m
Heave	0.42 m	0.14 m	0.24 m	-0.18 m

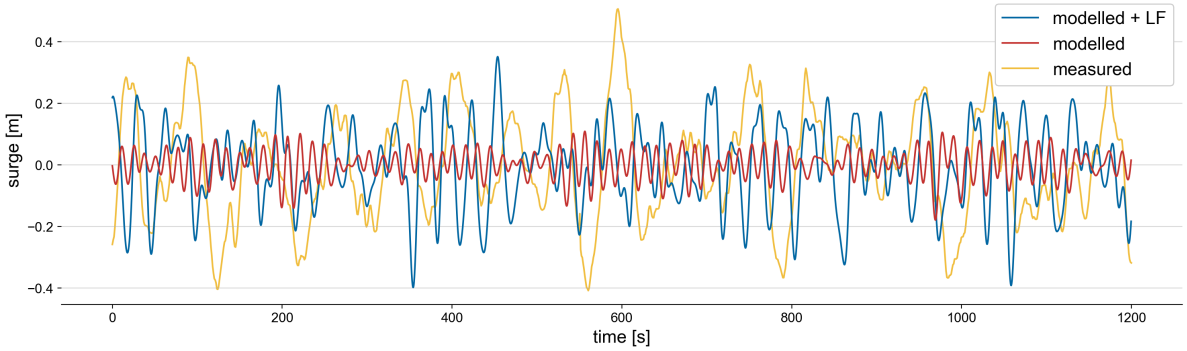

Figure 7.30: Comparison time series Base Case, including the added free long wave

7.5. Sensitivity Analysis

During the modelling, many assumptions have been made. Some of them are expected to have relevant influence on the resultant ship motions and those are discussed in this section.

7.5.1. Directional spreading

The first parameter that is expected to influence the results is the spreading parameter. As this was not measured at the wave buoy, an assumptions was made based on numbers available in literature. The spreading parameters that is used for the base case is m = 12, this is considered relatively low spread. As with higher spreading, more waves should be able to penetrate into the port basin, a run is done with higher directional spreading. A spreading factor of m = 5 is used to assess this influence. To keep the number of discreet directions equal, the resolution is set to 15°, which results in 7 components. In Figures 7.12 and 7.13, the r-DPRA output and the directional spreading function are shown.

The results show a small increase in wave height at the location of the AWAC, and minimal to no change in wave height next to the quay wall. It's is therefore concluded that it is not required to model the vessel motions with a higher DSPR, one-sided Directional Width of the Wave Spectrum. In Table 7.14, the results are shown.

7.5.2. Reflection coefficient beach

Next, the beach reflection coefficient is expected to influence the resultant wave height in the port basin, as the waves reflected by the beach can diffract into the basin. The reflection coefficients provided by Aquatica state that the beach reflection coefficient equals 0.10 for low tide and 0.20 for high tide. For the base case, a coefficient of 0.15 is used. To assess the influence of this coefficient, a run is done with a coefficient of 0.20 as well. It appeared the wave height at the quay increased from $H_{m0} = 0.25m$ to $H_{m0} = 0.29m$, as expected due to more energy from reflected waves penetrating into the port basin. This increase can lead to higher ship motions, however, it is not considered the main reason of difference between the modelled motions and measured motions.

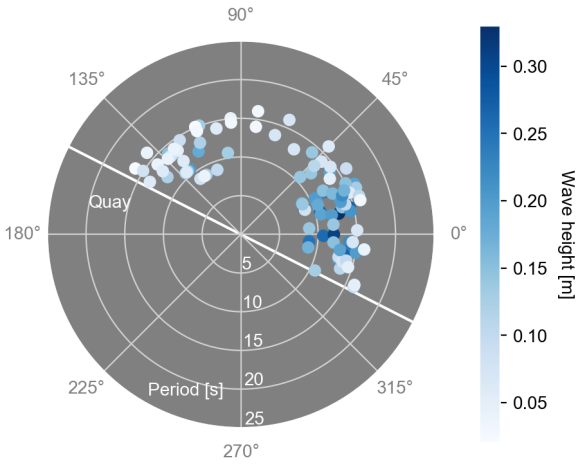

Table 7.12: Components found by r-DPRA, high spreading

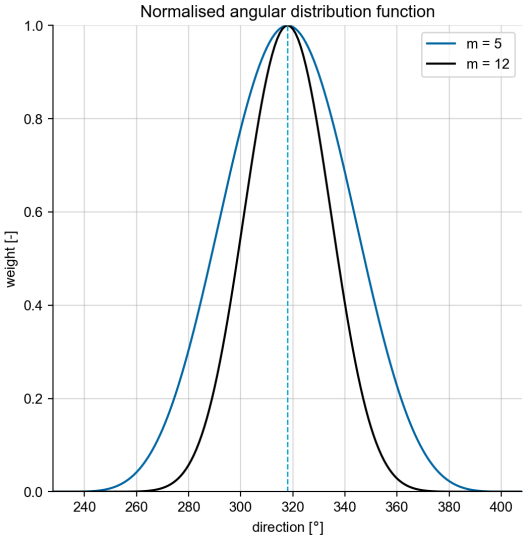

Table 7.13: Directional spreading function, cos^m

Table 7.14: Directional spreading sensitivity

	Base	**High Spreading**
m	12	5
DSPR	15.7°	22.9°
$H_{m0,quay}$, rDPRA	0.33 m	0.34 m
$H_{m0,quay}$, PHAROS	0.25 m	0.25 m
$H_{m0,awac}$, PHAROS	0.78 m	0.82 m

7.5.3. Mooring lines

Then, the mooring equipment assumptions are evaluated. Two major mooring characteristics are expected to influence the response of the vessel: The mean breaking load (MBL) of the mooring lines and the pretension of the mooring loads. The MBL was assumed to be 900 kN and the pretension 5% of the MBL, thus 45 kN. Increasing the MBL of the mooring lines also increases its stiffness, decreasing de natural periods of the system. In Appendix E, the natural periods are calculated for both the base case as for the heavy case. For a clean comparison, the exact same set of random phases is used and therefore the excitation is equal. First, the MBL is set to 600 kN, while the pretension is kept at 5%, 30 kN. The results are shown is Tables 7.15 and 7.16. It can be seen that the influence on the motions is minimal, in the order of centimeters.

Table 7.15: Weaker mooring lines, MBL = 600 kN

Motion	**Peak-Peak**	$4 \cdot \sigma$
Roll	0.30°	0.18°
Pitch	0.12°	0.08°
Yaw	0.11°	0.07°
Surge	0.38 m	0.21 m
Sway	0.29 m	0.18 m
Heave	0.21 m	0.13 m

Table 7.16: Standard mooring lines, MBL = 900 kN

Motion	**Peak-Peak**	$4 \cdot \sigma$
Roll	0.29°	0.19°
Pitch	0.12°	0.07°
Yaw	0.09°	0.06°
Surge	0.35 m	0.20 m
Sway	0.24 m	0.13 m
Heave	0.21 m	0.13 m

Then, two cases are considered with increasing and decreasing pretensions. One with a pretension of 10%, thus 90 kN and one with a pretension of 0%. The results are shown in Tables 7.31 and 7.32. It can be concluded that the effect of using weaker mooring lines does not significantly increase motions. The significant sway motions increases the most, with only 0.05 m. Reducing the pretension to 0%, does influence the surge and sway motion, with an increase of 0.09 m and 0.15 m respectively, which could indicate that during the measurements the mooring lines were looser than the assumed value of 5%. An increase to 10% pretension does not influence the significant motions too much, the roll motion shows the biggest increase: 0.04°.

Figure 7.31: MBL = 900 kN, pretension = 0%

Motion	**Peak-Peak**	$4 \cdot \sigma$
Roll	0.24°	0.14°
Pitch	0.12°	0.08°
Yaw	0.12°	0.07°
Surge	0.51 m	0.29 m
Sway	0.41 m	0.28 m
Heave	0.21 m	0.13 m

Figure 7.32: MBL = 900 kN, pretension = 10%

Motion	**Peak-Peak**	$4 \cdot \sigma$
Roll	0.36°	0.23°
Pitch	0.12°	0.07°
Yaw	0.12°	0.08°
Surge	0.32 m	0.20 m
Sway	0.27 m	0.15 m
Heave	0.20 m	0.12 m

8

Discussion and Conclusion

8.1. Discussion

This research can be considered as an exploratory study. The potential for using mild-slope wave models for dynamic mooring analysis is investigated and provides insight into the performance of the full model chain. It is important, however, to note that the comparison was made with full scale measurements. This is fairly unique for this type of research. Previous coupling studies were mostly compared with scale model measurements where conditions are optimal and wave conditions are selected beforehand. Wang (2018), Dobrochinski (2014) and Van der Ven (2012) all compared results on the level of forces on the vessel, and not without reason.

For comparison with real-life cases, wave forces are not measured and therefore ship motions or line loads need to be used. This introduces more uncertainties (lines, fenders, friction, added mass, etc...). It makes comparison of different methods harder, but provides insight in general applicability of a method and can be used to quantify uncertainties in the assumptions made.

This research emphasized the complexity of comparing model results with real life measurements. Where scale tests are designed for the purpose of the research, the measurements used for this study were not intended for ship motion model verification, and therefore key elements were not recorded, like wave height at the berth, mooring line characteristics and draught of the vessel. These unknown parameters lead to a higher uncertainty when interpreting the results. The best example of this uncertainty is found in the natural periods of the moored vessel. In the measurements a peak is found for surge around 75 s, while the modelled vessel had a natural period of around 31 s. This discrepancy makes it difficult to have a clear comparison of the ship motions.

The approach in this research, in contrary with scale model tests, identifies elements and processes that are relevant for the dynamic mooring analysis concept. The objective of a DMA in general is to model the (future) real life situations and not idealised situations as considered with scale model tests. Therefore the step to full scale measurements must also be made when starting with scale model tests. The steps taken in this research resemble the same steps required for DMA's. This emphasizes the exploratory character of this research in the broader idea of making DMA's more efficient and therefore more suitable for preliminary studies. Moreover, the outcomes of this research can be used to improve the scale model tests, by focusing on processes that were considered important in this study.

Furthermore, the port considered in this research is subjected to strong swell wave climates that are known to have associated low frequency waves in the range of periods that can cause problems for moored vessels. This is a non-linear effect and it can be seen that when modelling non-linear effects with linear models, like PHAROS, certain schematizations must be made that directly affect the accuracy of the results. For a more accurate comparison, ports subjected to wind waves only are more suitable for assessing the performance of a linear wave penetration model.

Moreover, choices are made that are known to be not the most accurate choice, however, they have a practical advantage. Due to the extend of the research and the amount of time available, the r-DPRA tool is chosen to be used for the coupling. Previous research suggests the panel method can lead to better results, however, this method is not fully developed and tested yet, while the r-DPRA tool has been already by De Jong and Borsboom (2012) and therefore could be implemented quickly.

Lastly, this research must be seen in the broader context of dynamic mooring analysis modelling. Much research has been done on connecting complex wave penetration models with different types of ship diffraction and ship motion models, however, most research is aimed on computational more demanding wave models. This research takes a different perspective and does not aim to make the results more accurate, it looks at how much accuracy can be sacrificed in order to win valuable time. This is a complete different approach and therefore this research can be regarded as exploratory, leaving room for further research.

8.2. Benefits and Limitations

8.2.1. Benefits Developed Method

The setup time of a model inPHAROS is considered moderate. When all developed scripts are used, a full model can be setup in a single day. The most crucial for the setup time is to have the bathymetry and boundaries ready in the correct format.

In terms of computational time, Van Mierlo (2014) showed that PHAROS is at least an order of magnitude faster than other conventional wave models like SWASH and TRITON. He modelled the same port geometry in both PHAROS, TRITON and SWASH and used roughly twice the number of grid cells for SWASH than for PHAROS. The PHAROS model contained just over 1/5th of the number of grid cells used for the model of La Coruña. He compared the total computational time needed and it was found that half an hour was needed for a PHAROS run, and just over one day for a SWASH run. For the La Coruña model, the order of magnitude has been in the order of a few hours. As a first conservative estimate, assuming a linear relation between computation time and number of grid cells, the SWASH computational time could be in the order of 125 hrs, as the La Coruña grid is five times larger.

This results a in computational time of PHAROS in the order of hours, while SWASH, for example, can last over five days. It can be concluded that the main benefit of PHAROS is the computational efficiency. In the full DMA chain, the wave modelling is considered the most time consuming in terms of computational costs. Therefore, the efficiency of the wave penetration model is considered to be the most important.

It must be noted that another benefit is found for the use of PHAROS as wave model. A DIFFRAC hydrodynamic database can be created in two different ways: 1) Computing the related forces for a given range of frequencies and directions, and 2) Imposing wave potentials of one specific wave field on the panels.

When PHAROS is used with the r-DPRA method, the transfer of information to the ship motion model, aNySIM, is done by means of the individual wave components. Therefore, DIFFRAC is only required to create a single hydrodynamic database, which is compatible with an unlimited amount of PHAROS conditions, as long as these wave are included in the modelled range in DIFFRAC. However, for the panel method, every computed wave field requires a new DIFFRAC simulation, as the potentials are directly imposed on the panels and exported as a time series of forces on the vessel. The same holds for using SWASH, this is also based on creating time series of forces on the vessel. This makes the use of PHAROS in combination with the r-DPRA method more suitable when having to model more wave conditions, as DIFFRAC only has to run once.

De Jong et al. (2016), proposed using a cascade of wave model types for the design of green ports. This meant that for different cases, different models can be considered the most suitable. A spectral model (SWAN), a mild-slope model (PHAROS) and a Boussinesq-type model (TRITON) were compared on applicability. For operational conditions, PHAROS was considered a suitable option for their case study, as moderate wave heights were accurately modelled by PHAROS. This research emphasized that the most complex model is not always the most suitable model to use, for instance if the model domain is too large. As DMA's mostly consider operational conditions as well, the cascade approach can be suggested for DMA's too, depending on the size of the domain and relevant physical processes that play a significant role. For ports where LF waves are

expected to be less dominant, diffraction plays an important role and the domain is relatively large, PHAROS is a suitable for the wave penetration modelling.

8.2.2. Limitations developed Method

The main limitation that was found is the long wave modelling. As known beforehand, PHAROS is a linear wave model and therefore not able to model interaction between waves. Wave groups form bound long waves, and these are therefore not included in the model. For ports susceptible to LF waves, PHAROS is not recommended when highly accurate model results are required.

For first estimates, however, a method has been applied to take the LF waves into account as well. A separate PHAROS run is setup with a low frequency wave spectrum following the approach as described by Van Der Hout et al. (2012). The same approach as with the primary waves was followed, and the 2D spectrum discretized into multiple components. This approach gives better results when modelling ports subject to LF waves in PHAROS.

Furthermore, PHAROS is not considered to be a user-friendly environment for setting up a model. As the software has been initially launched decades ago, there is a lack of automation in different steps of the model setup. The discreet wave frequencies that must be modelled have to be manually inserted, just like the different wave directions. The work flow could be optimized by updating the PHAROS graphical user interface and by automating pre-processing steps.

The last limitation of PHAROS is the reflection coefficients of the boundaries. They must be set manually for every boundary individually and therefore it is not advised to accurately model the coastline of a model, as every line element requires manual input. For every wave direction, the expected angle of incidence must be given. This implies iteration, as the incoming angle is for some boundaries depended on the reflected components of other boundaries. Multiple test runs must be done to calibrate incoming wave directions. The first iteration would focus on the beach and outer boundaries, while the next iterations would diverge to inside the port basin. For the model used in this research, three iterations were done.

8.3. Conclusion

In this research, the possibilities of PHAROS were extended and a method was developed to calculate the wave forces on ships. This method was first checked based on academic schematized situations. Then, this method was applied on the case study of La Coruña and compared with the measurements. Based on this research conclusions can be drawn on the suitability of the developed method. Finally, the main research question is answered: *How can a mild-slope wave model be used for the ship motion calculation on ships moored in ports and what are the benefits and limitations?*

First, it was investigated what coupling method could be considered the most suitable for this research. Both the panel method as the r-DPRA method were discussed and the decision was made to use the r-DPRA tool. This was based on the fact that this method was already tested (De Jong and Borsboom, 2012) and ready to apply. Moreover, a single DIFFRAC run would be sufficient to model different wave climates in contrary to the panel method, where every wave climate needs a new DIFFRAC run.

Secondly, the effect of modelling a quay wall was investigated. It was researched what the most accurate way of modelling a quay wall was without compromising the objective of this research to win computational efficiency. It was concluded that the quay wall should be modelled in DIFFRAC and reflected components found by the r-DPRA tool should be filtered-out to prevent double counting of wave components.

Then, full 2-dimensional wave spectra were tested. Multiple approaches to implement the r-DPRA outcome into aNySIM were discussed and finally it was chosen to directly impose a list of components into aNySIM, assigning random phase angles to those components. As a phenomena called 'phase-locking' occurred, it was decided, in order to obtain representative results, that five simulations must be run in aNySIM and the results have to be averaged. As these runs take in the order of tens of seconds, the computational efficiency goal was not compromised with this approach.

The developed method (Chapters 3, 4 and 5), was then applied to the case study of La Coruña, Spain. From the available measurements, one vessel was selected to be modelled as it had the most hours overlapping all three measurement techniques. It was decided to model two distinct moments in time, a moderate case and a more severe case, to test the performance of the model under different wave climates.

The two distinct moments in time were both modelled in PHAROS in the conventional way. The moderate case, however, was also used to apply a workaround to include free long waves as well. Assumptions and estimates were used for the unknown parameters like the draught of the vessel and the type and pretension of the mooring lines. For the mooring line characteristics, the directional spreading of the wave spectrum and the reflection coefficient of the beach, a separate sensitivity analysis was done to evaluate the effects of those parameters on the resultant wave heights and/or ship motions.

The wave penetration modelled by PHAROS was verified with the AWAC data at the entrance of the port. This showed an accurate modelling of the wave field. This research and previous research of the suitability of PHAROS for primary wave modelling in port basins shows the potential of implementing PHAROS as wave penetration model for the DMA workflow.

As PHAROS is a linear wave model, non-linear processes, such as bound long waves, are not included. The measurements show that for the case study, low-frequency wave forcing plays a significant role. With a conventional PHAROS run, without the low-frequency addition, the measured motions were not accurately modelled. Both the statistical data (significant and peak-peak values), as the time series were not considered to show much resemblance. In the measured time series, it could be seen that low-frequency wave forcing was dominant in the surge and sway motion, while this was not visible in the modelled time series.

As it was clear that free long waves played a significant role in the port of La Coruña, an additional step was described and applied in order to parametrize these free long waves. The modelled ship motions were more accurate in comparison with measured motions when these free long waves were added. Both statistically an increase in accuracy was found as in a visual comparison of time series, showing the low frequency wave pattern as found in the measurements.

When the low-frequency waves are modelled separately and added to the primary waves, the developed method can be considered more accurate. However, without further research it is not recommended to directly use this method for the detailed design of port layouts. This method is more suitable for preliminary studies, alternative layout comparison and performing quick-scans of layouts. When non-linearities such as the low frequency waves are expected to be significant, the wave models that accurately model these processes are required as the effect on the ship motions are significant as well. For case studies with less dominant low-frequency wave forcing, it is expected that the developed method performs better.

Finally, the main research question is answered:

How can a mild-slope wave model be used for the ship motion calculation on ships moored in ports and what are the benefits and limitations?

This research explored the possibilities of using the more computational efficient mild-slope wave model in the dynamic mooring analysis workflow. In Chapters 3, 4 and 5, a method was developed to couple this model with the ship diffraction model and ship motion model. The benefits of this method are:

- The computational efficiency; Conventionally used complex wave penetration models can take days to run a single simulation up to even weeks for large size domains. PHAROS runs take in the order of hours per wave condition and therefore has a clear advantage.
- Using the r-DPRA tool for coupling, only a single DIFFRAC run can be used to model multiple wave climates, whereas using the panel method for PHAROS or the direct coupling of the more complex wave models needs a new DIFFRAC run for every wave condition.

The main limitation of the proposed method is:

- The computations showed that the (non-linear) 2nd order effect of free long waves is not accurately modelled in the linear wave model PHAROS. A workaround to include free long waves improved the accuracy of the modelled ship motions, however, caution must be taken when applying the proposed method for ports where free long waves are expected to cause mooring issues.

The strengths of the this method are the computational efficiency and simplicity and it shows potential for use in dynamic mooring analyses. However, as this exploratory research provides first insights in the suitability, more research is required before commercially applying it.

8.4. Recommendations

8.4.1. Further Research

As mentioned in the discussion, a comparison was made based on full scale measurements done in the port of La Coruña. Fundamentally, it is more accurate to use scale model tests for validation. Deltares has a data set available that has been used by (Dobrochinski, 2014) and Wang (2018). This data set can be seen as a suitable validation for fundamental comparison on the level of forces. It is emphasized that this fundamental validation with scale model data should be the next step in the development of this new model chain. Hereafter, a case study of a port not subjected to long wave issues is recommended. In general, ports with direct exposure to oceans are subjected to swell waves which generate the bound long waves, it is therefore recommended to find ports without direct exposure to oceans. The proposed time path for further research is presented in Figure 8.1.

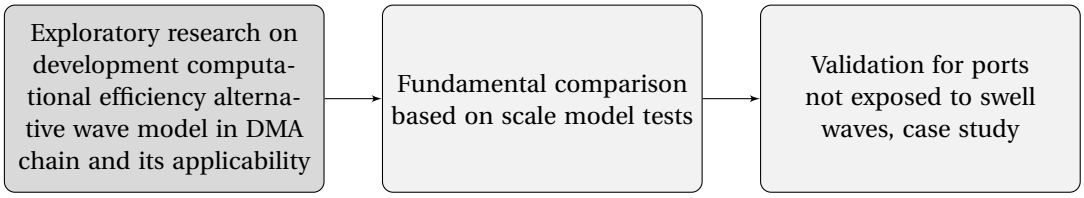

Figure 8.1: Proposed further research, with in the left box the research done in this thesis

8.4.2. Coupling method

In this research, the decision was made to use the r-DPRA tool for the coupling of PHAROS and aNySIM/DIFFRAC. This choice was also based on the applicability of r-DPRA, as it has been tested and ready to use. (Oude Vrielink, 2016) already showed that the panel method, directly imposing the wave potentials on the panels of the hull of the vessel, shows more accurate results. When scripts are developed to automate the extraction of the wave potentials and the panels of the ship, it is recommended to further investigate the performance of this panel method to see if the possible increase in accuracy out weights the need to run multiple DIFFRAC runs to model various wave fields.

8.4.3. Case studies

As known beforehand, PHAROS is not modelling the bound long associated with wave groups. In the port of La Coruña, however, these long waves appeared to be governing for surge and sway motions. Therefore, PHAROS is not capable of accurately modelling the motions in the port of La Coruña.

Therefore, it is recommended to apply the developed model chain to a port less exposed to long waves. In this way, it can be evaluated if PHAROS gives more accurate results for cases were the non-linearities do not play a significant role. In general, ports with direct exposure to oceans are subjected to swell waves which generate the bound long waves that can approach the resonance frequencies of the mooring systems.

8.4.4. Measurements

The measurement campaign in the Port of La Coruña included all six motions of the vessel, the mooring configuration and the wave buoy provided the offshore wave climate in terms of statistics. For more accurate modelling, raw buoy data could be made available to evaluate if the JONSWAP spectrum is indeed representative for the governing wave field. The same holds for the AWAC data, when rough data would be available, the

low frequency energy could be separated from the primary wave energy in order to validate the model performance. Moreover, especially for testing the model performance, it is recommended to have waves measured in front of the quay as well. Then, with more certainty the source of errors can be allocated, if it is the wave model itself or the coupling method where errors are introduced.

It must be noted that the initial goal of the measurement campaign was not to validate model chains, and therefore it was setup for other purposes and appeared to be useful for model validation.

With respect to the ship motion measurements at the quay, a few additional suggestions can be done for more accurate results. First, the draught of the ship is not measured and therefore estimates had to be made. More accurate HYD-files can be made when a camera would be pointed at the measuring line at the hull of the vessel.

Although a sensitivity analysis showed no great influence by the mooring line characteristics, more accurate results are expected when the actual characteristics are noted down. Any changes to mooring configuration during the mooring can be noted down as well, in order to accurately model moments at a later stage of the mooring.

Lastly, for more accurate calibration, it would be useful to use some sort of mooring line tension monitoring. When the tensions, and therefore pretensions, are known beforehand aNySIM can be calibrated on the pretensions in order to fully focus on the performance of the wave model. Moreover, the line loads can be compared for validation. Once the uncertainties of aNySIM and DIFFRAC are reduced, the conclusion about the wave model becomes stronger.

8.4.5. PHAROS development

As mentioned earlier in this chapter, the PHAROS software can be considered not very user-friendly. The Graphic User Interface works inefficient, multiple windows pop-up and the size of these windows is not always flexible. Much work is done by clicking with the cursor and navigating within tables is not always possible with the arrow keys. Moreover, some functionalities do not work the way they should, as saving a file is only done with pressing exit and not when pressing the save button. Also, inserting discreet wave frequencies and directions is much hand work as well.

Then, there is much to win if it comes to automation of the pre-processing of PHAROS. For this research, scripts have been developed that automate processes that are manually done in PHAROS. The selection process of discreet frequencies and directions can easily be implemented within PHAROS, in a way that only the number of components or resolution should be given and the model automatically selects the right frequencies based on either the equal energy distribution or the equal bin size distribution.

Furthermore, the definition of the expected angle of incidence for every boundary is a manual process is PHAROS. A script used for this research can be implemented and extended to automate this labor intensive process.

Overall, there is still much to improve or automated for PHAROS but this also expresses the potential for speeding up processes making PHAROS even more suitable for quick first estimates of hydrodynamics.

Bibliography

Aquatica (2019). Realización de una Campaña de Campo Mediante Sensores de Presion Y Dispositivos Doppler en el Puerto Exterior de Langosteira. Technical report.

Battjes, J. A. and Janssen, J. P. F. M. (1978). Energy loss and set-up due to breaking of random waves. *Proc. 16th Conf. Coastal Engineering (Hamburg)*, pages 569–587.

Berkhoff, J. (1972). Computation of Combined Refraction-Diffraction. *Proc. 13Th. Coastal Engng. Conf., (Vancouver, Canada)*, 1:471–490.

Bingham, H. (2000). A hybrid Boussinesq-panel method for predicting the motion of a moored ship. *Coastal Engineering*, 40(1):21–38.

De Jong, M., Reijmerink, S., Capel, A., and van der Hout, A. (2016). Combining Numerical Wave Models for Efficient Design of Port Layouts and Entrance Channels. *Pianc-Copedec*, pages 1–16.

De Jong, M. P. C. and Borsboom, M. J. A. (2012). A Practical Post-Processing Method to Obtain Wave Parameters from Phase-Resolving Wave Model Results. *The International Journal of Ocean and Climate Systems*, 3(4):203–216.

Deltares (2018). *PHAROS User Manual Version 9.13*.

Dobrochinski, J. P. H. (2014). A combination of SWASH and Harberth to compute wave forces on moored ships. *Delft University of Technology*.

Eikema, B. J. O., Attema, Y., Talstra, H., Bliek, A. J., De Wit, L., and Dusseljee, D. W. (2018). Spectral modeling of wave propagation in coastal areas with a harbor navigation channel. *PIANC-World Congress Panama City,*, pages 1–15.

Hasselmann, K. (1973). Measurements of Wind-Wave Growth and Swell Decay during the Joint North Sea Wave Project (JONSWAP). 46(8).

Holthuijsen, L. H. (2007). *Waves in Oceanic and Coastal Waters*. Cambridge University Press.

International Tanker Owners Pollution Federation (2019). URQUIOLA, Spain, 1976.

Janssen, T. and Van Dongeren, A. (2001). Phase Resolving Analysis of Multidirectional Wave Measurements. *Proceedings of Waves 2001*.

Journée, J. and Massie, W. (2001). *Offshore Hydromechanics*. Number January.

MARIN (2015). *DIFFRAC User Guide*.

MARIN (2018). *aNySIM Theory Documentation*.

Mciver, P. and Evans, D. V. (1984). The occurrence of negative added mass in free-surface problems involving submerged oscillating bodies. *Journal of Engineering Mathematics*, 18(1):7–22.

Ministerio de Transportes Movilidad Y Agenda Urbana (2019). Puertos del Estado.

Oude Vrielink, J. J. (2016). Improved Coupling PHAROS - DIFFRAC.

Peña, E., Figuero, A., Sande, J., Guerra, A., Perez, J. D., and Maciñeira, E. (2017). Integrated System to Evaluate Moored Ship Behavior. *ASME 2017 36th International Conference on Ocean, Offshore and Arctic Engineering*.

Port Authority of A Coruña (2014). Muelle Transversal y Explanada.

Port Authority of A Coruña (2019a). Fechas Batimetrias. Technical report.

Port Authority of A Coruña (2019b). Punta Langosteira.

Prosertek (2016). SC Fender Data Sheet. pages 2–5.

Putnam, J. A. and Johnson, J. W. (1949). The dissipation of wave energy by bottom friction. *Trans. Am. Geophys. Union*, 30(1):67–74.

Reijmerink, B. (2012). Golfrandvoorwaarden in havens. *Delft University of Technology*.

Van Der Hout, A. J., De Jong, M. P., Moerman, E., Timerman, G. J., and Ribeiro, E. O. (2012). Determination of infragravity wave conditions at a nearshore location with a non-uniform coastline - Case study of Baía de Todos os Santos, Brazil. *Proceedings of the International Conference on Offshore Mechanics and Arctic Engineering - OMAE*, 5:249–257.

Van der Molen, W. and Wenneker, I. (2006). *Behaviour of Moored Ships in Harbours*. PhD thesis.

Van der Ven, P. (2012). The use of numerical models to determine the response of moored vessels to waves in a complex harbour geometry. *Delft University of Technology*.

Van Essen, S., Van der Hout, A., Huijsmans, R., and Waals, O. (2013). Evaluation of Directional Analysis Methods for Low-Frequency Waves to Predict LNGC Motion Response in Nearshore Areas. *OMAE2013*, pages 1–11.

Van Mierlo, F. (2014). Numerical modelling of wave penetration in ports.

Wang, H. (2018). Frequency domain diffraction analysis to determine wave forces on a moored ship in a complex wave field. *Delft University of Technology*.

A

Appendix A

A.1. r-DPRA sensitivity analysis

In this paragraph, the sensitivity of the r-DPRA tool is being tested. Before deploying the r-DPRA tool to a PHAROS output wave field, two parameters have to be set: the location of the target point and the radius of the analysis circle. The right combination must be found to reduce inaccuracies in the resultant wave information.

The first issue is the cutoff of the circle by structures. As ships are moored next to quay walls, the r-DPRA tool is frequently used to calculate wave information close to domain boundaries. When the radius of the circle is larger than the distance to the quay wall, the circle gets cutoff. When the cutoff is large enough, this can lead to misinterpretation of the wave field by the r-DPRA tool, see Figure A.1.

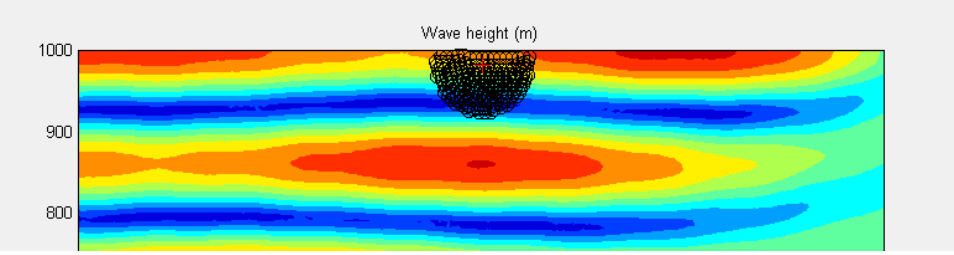

Figure A.1: Cutoff by r-DPRA tool

A second issue that might be raised is that the radius is too small for accurately interpreting the wave information. In the PHAROS manual, it is recommended to use a radius of 0.1 to 0.3 times the wave length. Different non-existing components might appear in the r-DPRA results when the a wrong circle radius is used.
The three variables that determine the quality of the r-DPRA tool are:

- **Energy conservation**; the wave heights of incoming and reflected components can be over-or underestimated by the tool, this difference in energy directly leads to an error in the ship motions. Due to linearity, the ship motion caused by the undisturbed wave field changes with the same factor as the wave height error.
- **Directional accuracy**; Inaccuracies in wave direction can lead to different added mass and damping factors to be used for the ship motion and therefore lead to errors.
- **Non-existing components**; When non-existing components are found, certain motions of the ship can be triggered. For example, bow-on waves cause little roll motion, but when a non-existing beam-on component is found, roll can become significant.

For this analysis, two parameters are evaluated: The distance to the quay wall and the radius of the analysis circle. The distance to quay wall changes from 20 m to 100 m, with a spatial resolution of 10 m and the radius

from $0.1 * wavelength$ to $0.3 * wavelength$ with a resolution $0.05 * wavelength$, the results are presented below.

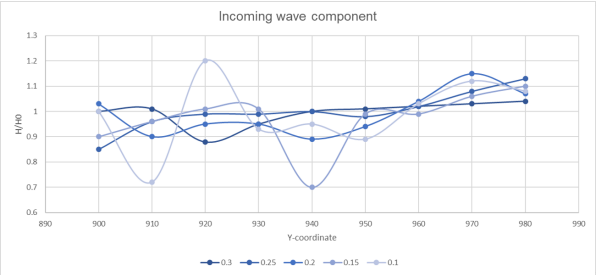

Figure A.2: Incoming wave heights, expressed relative to theoretical wave height

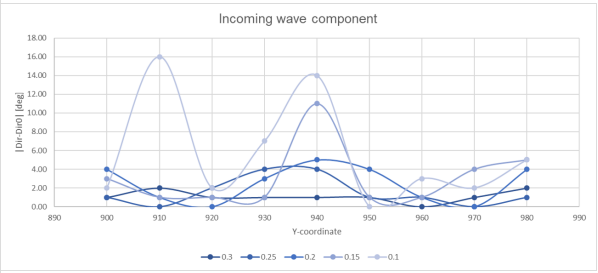

Figure A.3: Incoming wave direction, expressed relatively to theoretical wave direction

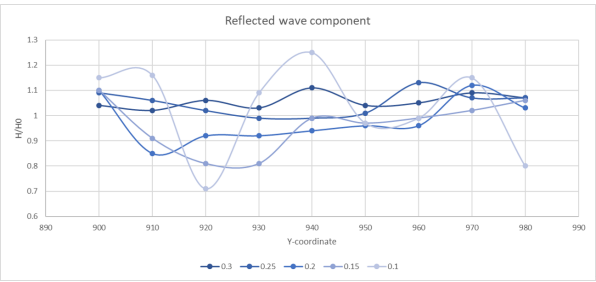

Figure A.4: Reflected wave heights, expressed relative to theoretical wave height

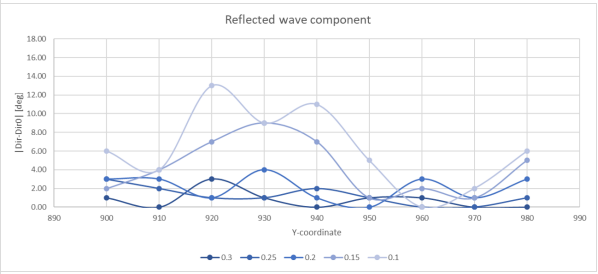

Figure A.5: Incoming wave direction, expressed relatively to theoretical wave direction

The results do not show an optimal combination, but a few notes can be made about the choices of parameters.

- Both the incoming and reflected wave can introduce an error which can be up to 30% of the theoretical value. The error in wave energy tends to become larger for smaller radii of the analysis circle. The largest errors are found, both in incoming and reflected wave, for the radii of 0.10 and 0.15 times the wavelength. It is therefore not recommended to use a small radius of the circle.
- The errors in wave direction are in the order of 10% for the incoming wave and 5% for the reflected wave. Also for this variable it holds that the radii of 0.10 and 0.15 perform the worst.
- Additional non-existent wave components are found in the cases with a radius of 0.1 and in the cases with a large radius (0.3) in combination with a small distance to the quay wall, which means a large cutoff. Also, at the particular case of 60 m distance from the quay wall introduces extra components. This means non-existing components are also introduced randomly, depending on the target point.

These results were checked with the base model from Chapter 3 and similar results were found; The radius of 0.1 perform weakly both in terms of energy conservation as in number of non-existing components. In this case, however, the relative errors are smaller. Moreover, the radius of 0.3 performs weakly as well.

Table A.1: Sensitivity r-DPRA tool, quay wall case

radius	dist. to quay	H1	dir1	H2	dir2	add. components	circle cutoff
67	20	1.04	137	1.07	225	1	yes
67	30	1.03	136	1.09	225	1	yes
67	40	1.02	135	1.05	226	0	yes
67	50	1.01	134	1.04	226	0	yes
67	60	1.00	136	1.11	225	0	yes
67	70	0.95	134	1.03	226	0	no
67	80	0.88	134	1.06	228	0	no
67	90	1.01	133	1.02	225	0	no
67	100	1.00	134	1.04	224	0	no
56	20	1.13	136	1.07	224	0	yes
56	30	1.08	135	1.07	225	0	yes
56	40	1.02	136	1.13	225	0	yes
56	50	0.98	134	1.01	226	0	yes
56	60	1.00	131	0.99	223	1	no
56	70	0.99	131	0.99	224	0	no
56	80	0.99	133	1.02	226	0	no
56	90	0.96	135	1.06	227	0	no
56	100	0.85	136	1.09	222	0	no
44	20	1.07	131	1.03	228	0	yes
44	30	1.15	135	1.12	226	0	yes
44	40	1.04	134	0.96	228	0	yes
44	50	0.94	131	0.96	225	0	no
44	60	0.89	130	0.94	224	0	no
44	70	0.95	132	0.92	229	0	no
44	80	0.95	135	0.92	226	0	no
44	90	0.90	134	0.85	222	0	no
44	100	1.03	131	1.10	222	0	no
33	20	1.10	130	1.06	230	0	yes
33	30	1.06	131	1.02	226	0	yes
33	40	0.99	134	0.99	223	0	no
33	50	0.99	134	0.97	224	0	no
33	60	0.70	124	0.99	218	2	no
33	70	1.01	136	0.81	234	0	no
33	80	1.01	136	0.81	232	0	no
33	90	0.96	136	0.91	221	0	no
33	100	0.90	138	1.10	227	0	no
22	20	1.08	130	0.80	231	1	yes
22	30	1.12	133	1.15	227	0	no
22	40	1.03	132	0.99	225	0	no
22	50	0.89	135	0.97	220	0	no
22	60	0.95	149	1.25	214	1	no
22	70	0.93	142	1.09	216	1	no
22	80	1.20	133	0.71	238	2	no
22	90	0.72	151	1.16	221	1	no
22	100	1.00	137	1.15	219	1	no

Table A.2: Sensitivity r-DPRA tool, base case (no structures)

radius	dist. to quay	H1	dir1	add. components	circle cutoff
67	20	0.88	138	0	yes
67	30	0.94	138	0	yes
67	40	1.00	136	0	yes
67	50	0.96	135	0	yes
67	60	1.00	133	0	yes
67	70	0.86	133	0	no
67	80	0.86	132	0	no
67	90	0.98	135	0	no
67	100	0.98	135	0	no
56	20	0.99	138	0	yes
56	30	0.99	135	0	yes
56	40	0.99	135	0	yes
56	50	0.99	134	1	yes
56	60	1.02	134	0	no
56	70	1.02	134	0	no
56	80	0.94	135	0	no
56	90	1.02	135	0	no
56	100	1.06	136	0	no
44	20	1.01	136	0	yes
44	30	0.97	134	0	yes
44	40	0.97	134	0	yes
44	50	0.98	136	0	no
44	60	0.98	134	0	no
44	70	1.00	137	0	no
44	80	1.02	135	0	no
44	90	0.96	137	0	no
44	100	0.92	135	0	no
33	20	1.02	134	0	yes
33	30	1.04	133	0	yes
33	40	1.03	134	0	no
33	50	1.00	134	0	no
33	60	0.95	134	0	no
33	70	1.02	133	1	no
33	80	0.99	134	0	no
33	90	1.00	139	0	no
33	100	0.95	138	0	no
22	20	1.04	134	0	yes
22	30	1.03	134	0	no
22	40	0.99	133	0	no
22	50	0.98	133	0	no
22	60	0.87	137	2	no
22	70	1.02	131	0	no
22	80	1.06	135	0	no
22	90	0.78	136	4	no
22	100	1.00	135	1	no

B

Appendix B

Table B.1: Overview vessels

Year	**Vessel**	**IMO**	**DWT**	**Length**	**Beam**	**Cargo**	**Bollards**	**Incidents**	**Hs,max**	**Tp,max**	**Dir**	**IMU**	**Distance**	**Cameras**
-	-	-	t	m	m	-	-	-	m	s	deg	hours	hours	hours
2017-2018	Kyzikos	9343845	92,598	229.5	36.9	MaiE	17-26	No	4.0	13.7	318	23	24	22
2017-2018	Nord Saturn	9644536	77,288	225.0	32.3	Bauxite	9-18	Broken lines	6.5	14.3	335	72	71	15
2017-2018	CSK Unity	9727314	77,105	225.0	32.2	Maize	13-22	No	5.2	15.0	314.5	96	98	20
2017-2018	Aloe	9320336	30,618	178.7	28.0	Wheat	31-24	Broken lines	3.8	16.7	316	51	45	24
2017-2018	Don Juan	9394222	21,057	158.0	23.0	Coal, clinker	63-50, 19-26	No	3.5	10.5	2.0	69	57	13
2018-2019	Pegasus	9611242	81,852	179.9	30.0	Unknown	22-30	No	7.2	18.2	333	23	43	7

C

Appendix C

C.1. Reference case

	1st Order Excitation Force			2nd Order Excitation Force			
	Surge	**Sway**	**Heave**	**Surge**	**Sway**	**Heave**	**Water lvl**
run1	9.93E+05	3.56E+06	5.53E+06	950.12	1511.46	19785.4	0.272031
run2	1.09E+06	3.71E+06	5.92E+06	9.72E+02	1.71E+03	1.77E+04	2.61E-01
run3	1.01E+06	3.31E+06	5.03E+06	7.79E+02	1.64E+03	1.77E+04	2.43E-01
run4	1.10E+06	3.47E+06	5.65E+06	8.71E+02	1.65E+03	1.86E+04	2.52E-01
run5	948078	3.42E+06	5.45E+06	829.847	1266.41	15363.4	0.2294
run6	998698	3.47E+06	5.39E+06	8.58E+02	1.45E+03	1.85E+04	2.51E-01
run7	931092	3.15E+06	5.09E+06	8.51E+02	1.59E+03	1.45E+04	2.57E-01
run8	1.14E+06	4.16E+06	6.55E+06	9.12E+02	1.72E+03	2.18E+04	2.85E-01
run9	955021	3.53E+06	5.46E+06	1.03E+03	1.80E+03	1.88E+04	2.38E-01
run10	1.09E+06	3.29E+06	5.37E+06	8.93E+02	1.71E+03	1.93E+04	2.71E-01
run11	1.06E+06	3.78E+06	6.05E+06	9.52E+02	1.76E+03	1.70E+04	2.68E-01
run12	9.26E+05	3.11E+06	4.90E+06	8.64E+02	1.42E+03	1.82E+04	2.33E-01
run13	9.31E+05	3.04E+06	4.86E+06	9.36E+02	1.50E+03	1.83E+04	2.39E-01
run14	1.04E+06	3.51E+06	5.85E+06	9.02E+02	1.79E+03	1.52E+04	2.55E-01
run15	9.59E+05	3.47E+06	5.35E+06	8.09E+02	1.41E+03	1.74E+04	2.29E-01
run16	9.94E+05	3.44E+06	5.33E+06	8.08E+02	1.19E+03	1.76E+04	2.42E-01
run17	1.09E+06	3.51E+06	5.29E+06	9.03E+02	1.72E+03	2.35E+04	2.48E-01
run18	1.16E+06	3.97E+06	6.35E+06	1.14E+03	1.95E+03	2.45E+04	2.82E-01
run19	1.02E+06	3.61E+06	5.49E+06	7.46E+02	1.44E+03	1.87E+04	2.30E-01
run20	9.49E+05	3.00E+06	4.83E+06	6.85E+02	1.71E+03	1.87E+04	2.34E-01
run21	9.85E+05	3.16E+06	5.06E+06	8.62E+02	1.85E+03	1.80E+04	2.34E-01
run22	1.03E+06	3.01E+06	5.03E+06	9.52E+02	2.21E+03	1.58E+04	2.39E-01
run23	1.01E+06	3.71E+06	5.75E+06	8.10E+02	1.45E+03	1.68E+04	2.56E-01
run24	1.03E+06	3.44E+06	5.29E+06	8.97E+02	2.28E+03	2.08E+04	2.64E-01
run25	1.04E+06	3.18E+06	5.14E+06	7.24E+02	1.64E+03	2.04E+04	2.37E-01

	1st Order Excitation Force			2nd Order Excitation Force			
	Surge	**Sway**	**Heave**	**Surge**	**Sway**	**Heave**	**Water lvl**
run1	9.93E+05	3.56E+06	5.53E+06	9.50E+02	1.51E+03	1.98E+04	2.72E-01
run2	1.04E+06	3.63E+06	5.73E+06	9.61E+02	1.61E+03	1.88E+04	2.67E-01
run3	1.03E+06	3.53E+06	5.49E+06	9.00E+02	1.62E+03	1.84E+04	2.59E-01
run4	1049581	3512445	5531900	892.8805	1628.515	18457.78	0.257123
run5	1029281	3494008	5515806	880.2738	1556.094	17838.9	0.251578
run6	1024184	3490098	5494288	876.6062	1538.863	17952.63	0.251436
run7	1010885	3441587	5436624	873.0134	1546.001	17457.86	0.252267
run8	1026494	3531833	5575503	877.8991	1567.63	17996.38	0.256393
run9	1018553	3531817	5562551	895.2759	1593.734	18080.91	0.254351
run10	1025640	3507312	5543675	895.048	1605.172	18207.34	0.255969
run11	1.03E+06	3.53E+06	5.59E+06	9.00E+02	1.62E+03	1.81E+04	2.57E-01
run12	1.02E+06	3.50E+06	5.53E+06	8.97E+02	1.60E+03	1.81E+04	2.55E-01
run13	1.01E+06	3.46E+06	5.48E+06	9.00E+02	1.60E+03	1.81E+04	2.54E-01
run14	1.02E+06	3.46E+06	5.51E+06	9.00E+02	1.61E+03	1.79E+04	2.54E-01
run15	1.01E+06	3.46E+06	5.50E+06	8.94E+02	1.60E+03	1.79E+04	2.52E-01
run16	1.01E+06	3.46E+06	5.49E+06	8.89E+02	1.57E+03	1.79E+04	2.52E-01
run17	1.01E+06	3.47E+06	5.47E+06	8.90E+02	1.58E+03	1.82E+04	2.51E-01
run18	1.02E+06	3.49E+06	5.52E+06	9.04E+02	1.60E+03	1.85E+04	2.53E-01
run19	1.02E+06	3.50E+06	5.52E+06	8.95E+02	1.59E+03	1.86E+04	2.52E-01
run20	1.02E+06	3.48E+06	5.49E+06	8.85E+02	1.60E+03	1.86E+04	2.51E-01
run21	1.02E+06	3.46E+06	5.47E+06	8.84E+02	1.61E+03	1.85E+04	2.50E-01
run22	1.02E+06	3.44E+06	5.45E+06	8.87E+02	1.64E+03	1.84E+04	2.50E-01
run23	1.02E+06	3.45E+06	5.46E+06	8.83E+02	1.63E+03	1.83E+04	2.50E-01
run24	1.02E+06	3.45E+06	5.45E+06	8.84E+02	1.66E+03	1.84E+04	2.51E-01
run25	1.02E+06	3.44E+06	5.44E+06	8.78E+02	1.66E+03	1.85E+04	2.50E-01

C.2. Time Series

	1st Order Excitation Force			2nd Order Excitation Force			
	Surge	**Sway**	**Heave**	**Surge**	**Sway**	**Heave**	**Water lvl**
sim1	1.15E+06	2.74E+06	4.84E+06	1.93E+04	4.98E+04	4.06E+04	2.52E-01
sim2	1.16E+06	2.75E+06	4.87E+06	2.15E+04	5.56E+04	4.05E+04	2.53E-01
sim3	1.14E+06	2.71E+06	4.78E+06	2.06E+04	5.28E+04	3.95E+04	2.50E-01
sim4	1.14E+06	2.71E+06	4.79E+06	2.02E+04	5.23E+04	4.11E+04	2.50E-01
sim5	1.15E+06	2.75E+06	4.86E+06	1.85E+04	4.81E+04	4.13E+04	2.53E-01
average	1.15E+06	2.73E+06	4.83E+06	2.00E+04	5.17E+04	4.06E+04	2.51E-01

	1st Order Excitation Force			2nd Order Excitation Force			
	Surge	**Sway**	**Heave**	**Surge**	**Sway**	**Heave**	**Water lvl**
sim1	1.15E+06	2.74E+06	4.84E+06	1.93E+04	4.98E+04	4.06E+04	2.52E-01
sim2	1.15E+06	2.75E+06	4.85E+06	2.04E+04	5.27E+04	4.05E+04	2.53E-01
sim3	1.15E+06	2.73E+06	4.83E+06	2.05E+04	5.27E+04	4.02E+04	2.52E-01
sim4	1.15E+06	2.73E+06	4.82E+06	2.04E+04	5.26E+04	4.04E+04	2.51E-01
sim5	1.15E+06	2.73E+06	4.83E+06	2.00E+04	5.17E+04	4.06E+04	2.51E-01

	1st Order Excitation Force			2nd Order Excitation Force			
	Surge	**Sway**	**Heave**	**Surge**	**Sway**	**Heave**	**Water lvl**
sim1	13.1%	-20.3%	-11.0%	2101.9%	2907.3%	119.0%	0.8%
sim2	13.3%	-20.2%	-10.8%	2226.4%	3083.4%	118.8%	1.1%
sim3	12.7%	-20.5%	-11.3%	2234.0%	3084.7%	117.0%	0.7%
sim4	12.5%	-20.7%	-11.4%	2225.9%	3077.9%	118.3%	0.5%
sim5	12.6%	-20.6%	-11.3%	2182.2%	3023.5%	119.2%	0.6%

C.3. Direct component conversion

	1st Order Excitation Force			2nd Order Excitation Force			
	Surge	**Sway**	**Heave**	**Surge**	**Sway**	**Heave**	**Water lvl**
sim1	9.77E+05	2.92E+06	4.52E+06	9.60E+02	8.82E+02	2.34E+04	2.31E-01
sim2	1.25E+06	3.88E+06	6.50E+06	9.43E+02	1.07E+03	1.83E+04	2.55E-01
sim3	8.78E+05	2.85E+06	4.37E+06	8.17E+02	8.50E+02	1.71E+04	2.31E-01
sim4	1.08E+06	3.43E+06	5.47E+06	9.54E+02	8.93E+02	1.69E+04	2.53E-01
sim5	1.07E+06	3.46E+06	5.57E+06	8.51E+02	1.03E+03	1.78E+04	2.47E-01
sim6	1.07E+06	3.37E+06	5.39E+06	1.02E+03	1.02E+03	2.52E+04	2.73E-01
sim7	1.12E+06	3.77E+06	5.87E+06	8.60E+02	9.71E+02	2.49E+04	2.70E-01
sim8	1.16E+06	3.48E+06	5.42E+06	1.14E+03	1.03E+03	2.46E+04	2.60E-01
sim9	1.01E+06	2.92E+06	4.65E+06	9.57E+02	9.30E+02	2.02E+04	2.41E-01
sim10	1.00E+06	3.30E+06	5.15E+06	1.02E+03	1.02E+03	1.93E+04	2.48E-01
Average	1.05E+06	3.31E+06	5.29E+06	9.05E+02	9.45E+02	1.87E+04	2.43E-01

	1st Order Excitation Force			2nd Order Excitation Force			
	Surge	**Sway**	**Heave**	**Surge**	**Sway**	**Heave**	**Water lvl**
sim1	9.77E+05	2.92E+06	4.52E+06	9.60E+02	8.82E+02	2.34E+04	2.31E-01
sim2	1.11E+06	3.40E+06	5.51E+06	9.51E+02	9.77E+02	2.09E+04	2.43E-01
sim3	1.03E+06	3.21E+06	5.13E+06	9.06E+02	9.34E+02	1.96E+04	2.39E-01
sim4	1.05E+06	3.27E+06	5.22E+06	9.18E+02	9.24E+02	1.89E+04	2.42E-01
sim5	1.05E+06	3.31E+06	5.29E+06	9.05E+02	9.45E+02	1.87E+04	2.43E-01
sim6	1.05E+06	3.32E+06	5.30E+06	9.25E+02	9.58E+02	1.98E+04	2.48E-01
sim7	1.06E+06	3.38E+06	5.38E+06	9.16E+02	9.60E+02	2.05E+04	2.51E-01
sim8	1.08E+06	3.40E+06	5.39E+06	9.43E+02	9.68E+02	2.10E+04	2.52E-01
sim9	1.07E+06	3.34E+06	5.31E+06	9.45E+02	9.64E+02	2.09E+04	2.51E-01
sim10	1.06E+06	3.34E+06	5.29E+06	9.53E+02	9.69E+02	2.08E+04	2.51E-01

	1st Order Excitation Force			2nd Order Excitation Force			
	Surge	**Sway**	**Heave**	**Surge**	**Sway**	**Heave**	**Water lvl**
sim1	-4%	-15%	-17%	9%	-47%	26%	-7%
sim2	9%	-1%	1%	8%	-41%	13%	-3%
sim3	2%	-7%	-6%	3%	-44%	6%	-4%
sim4	3%	-5%	-4%	5%	-44%	2%	-3%
sim5	3%	-4%	-3%	3%	-43%	1%	-3%
sim6	3%	-4%	-3%	5%	-42%	7%	-1%
sim7	4%	-2%	-1%	4%	-42%	11%	0%
sim8	6%	-1%	-1%	8%	-41%	14%	1%
sim9	5%	-3%	-2%	8%	-42%	13%	0%
sim10	4%	-3%	-3%	9%	-41%	12%	0%

Appendix D

In Chapter 5, the phenomena phase-locking is first described. This occurs when there are multiple components with the exact same frequency present in a wave field. In this section, the phenomena will be explained and the an alternative way to bypass this phenomena will be assessed.

As the two waves have the same frequency, their phase velocity is equal. This means that their phases are "locked", over time this phase angle will not change. When assigning random phases, as is done when going from a wave spectrum to a time series, the initially assigned phases create a fixed phase angle between components, that lasts for the full simulation. Therefore, extending the simulation time will not influence the results. However, running multiple simulations with different sets of phase angles will deliver different results. Running a large number of simulation and finally averaging the result will lead to an accurate solution.

In Figure D.1 and D.2, the influence of the phase angle between two harmonics can be seen. In Figure D.1, the phase angle is chosen in a way that the two harmonic strengthen each other; the sum has a greater amplitude than the individual waves. When the two waves are in phase, the amplitude doubles and when they are exactly out of phases, the amplitude goes to zero.

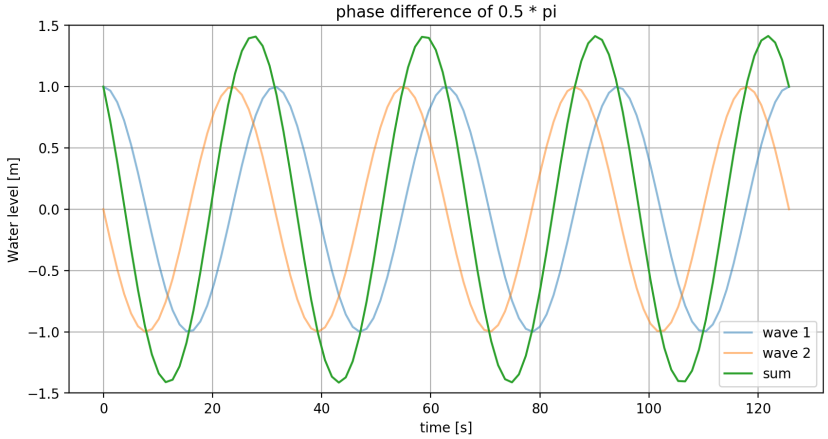

Figure D.1: Bichromatic wave with a phase angle of $0.5 * \pi$

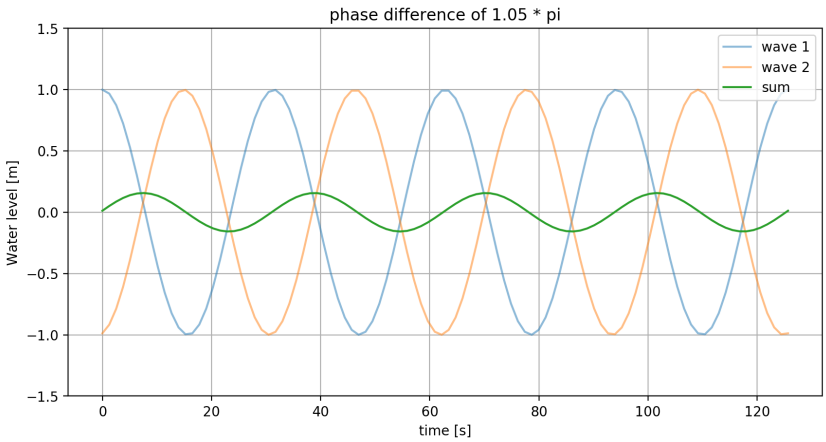

Figure D.2: Bichromatic wave with a phase angle of $1.05 * \pi$

On a larger scale, this occurs with the Direct Component method. As the 2-dimensional spectrum is discretized in both frequency as in directional domain, one frequency will have multiple components with different directions. Therefore, phase-locking occurs in 2D. This method of summing the individual components is identified as the *double summation method*. **?**, considered the *single summation method*.

This single summation method is based on the principle that one single discreet frequency represents a bandwidth of frequencies around that same frequency. It is therefore considered that the energy can also be redistributed over multiple frequencies within this bandwidth. In this way, it is prevented that multiple components are summed with the exact same frequency and therefore phase-locking is avoided.

In Figures D.5 until D.10, the results are shown for using the alternative single summation method. It can be seen that the duration of the simulation influences the convergence of the averages. For a duration of T = 100,000s, almost 28 hours, the benefits of running 5 simulation instead of 1 is around 1% for the first order excitation. As expected, the benefit of running more simulations increases as the duration of the simulation decreases.

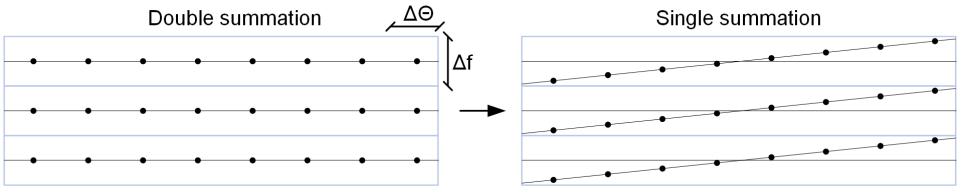

Figure D.3: Double summation method and single summation method

Next, the effect of using the single summation method is evaluated. A script is written that takes the original list of components that is used for the double summation method and the frequencies are adapted according to the single summation method.

The smallest frequency step in the discretization step of section 5.1.1 is about 0.0060 rad/s and the number of components per frequency is between 5 and 7. Therefore, the step size should be at one order of magnitude smaller, preferably smaller. It is set to 0.0001 rad/s to prevent new frequencies from leaving the frequency band.

In Figure D.4, the water level statistics are shown by means of the H_{m0}. Here, it is clear that for a longer duration, the H_{m0} converges faster.

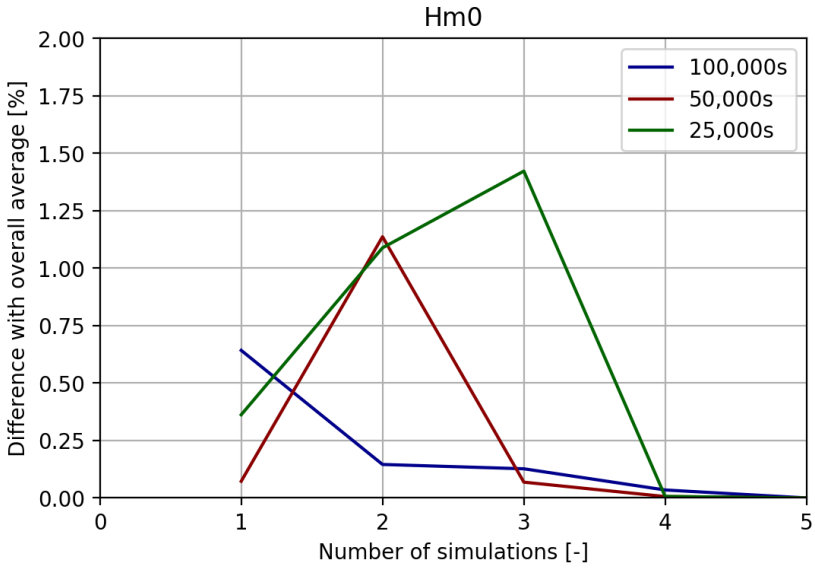

Figure D.4: Single summation method, Hm0 averages for different simulation durations

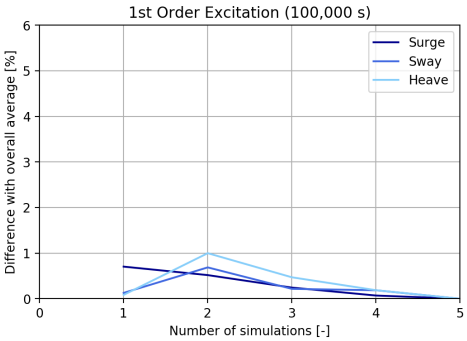

Figure D.5: Single summation method, 1st order forces (average standard deviation) T = 100,000s

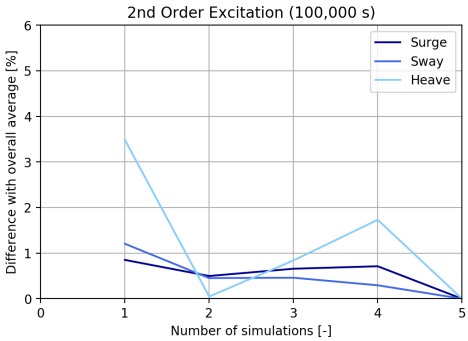

Figure D.6: Single summation method, 2nd order forces (average standard deviation) T = 100,000s

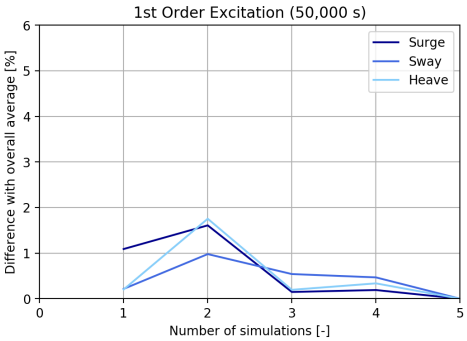

Figure D.7: Single summation method, 1st order forces (average standard deviation) T = 50,000s

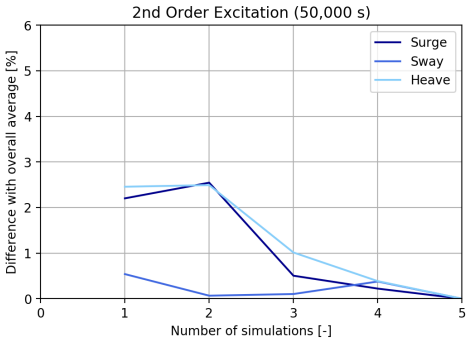

Figure D.8: Single summation method, 2nd order forces (average standard deviation) T = 50,000s

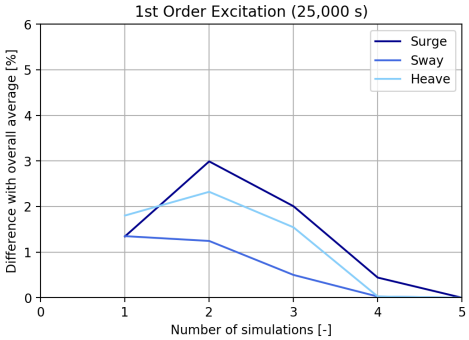

Figure D.9: Single summation method, 1st order forces (average standard deviation) T = 25,000s

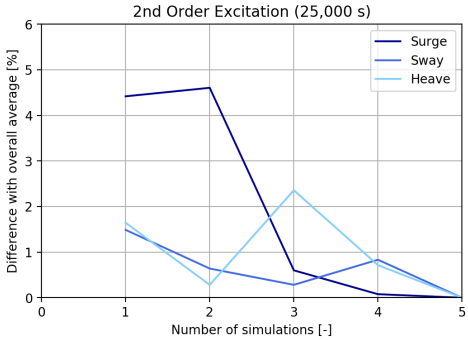

Figure D.10: Single summation method, 2nd order forces (average standard deviation) T = 25,000s

Appendix E

In this section, the natural periods of the vessel-mooring system will be calculated for both the base case as the heavy case.

The approach is to perform decay tests in aNySIM. In a still water run, the vessel is moored accordingly and kept in the equilibrium position. Then, an external force will be build up that pulls the vessel out of its equilibrium position. When the maximum force is reached, this force is kept constant for a while in order to reduce accelerations to zero. Then, suddenly, the force is reduced to zero in just one second, practically releasing the vessel. The vessel will then bounce back to it's equilibrium position by a harmonic motion. The period of this motion is the natural periods of the system for that specific degree of freedom. This same process holds for the rotations, just with a moment instead of a force.

Motion	MBL = 900 kN	MBL = 600 kN
Surge	31 s	36 s
Sway	27 s	28 s

Table E.1: Natural periods base case

Motion	MBL = 900 kN	MBL = 600 kN
Surge	26 s	32 s
Sway	17 s	20 s

Table E.2: Natural periods heavy case

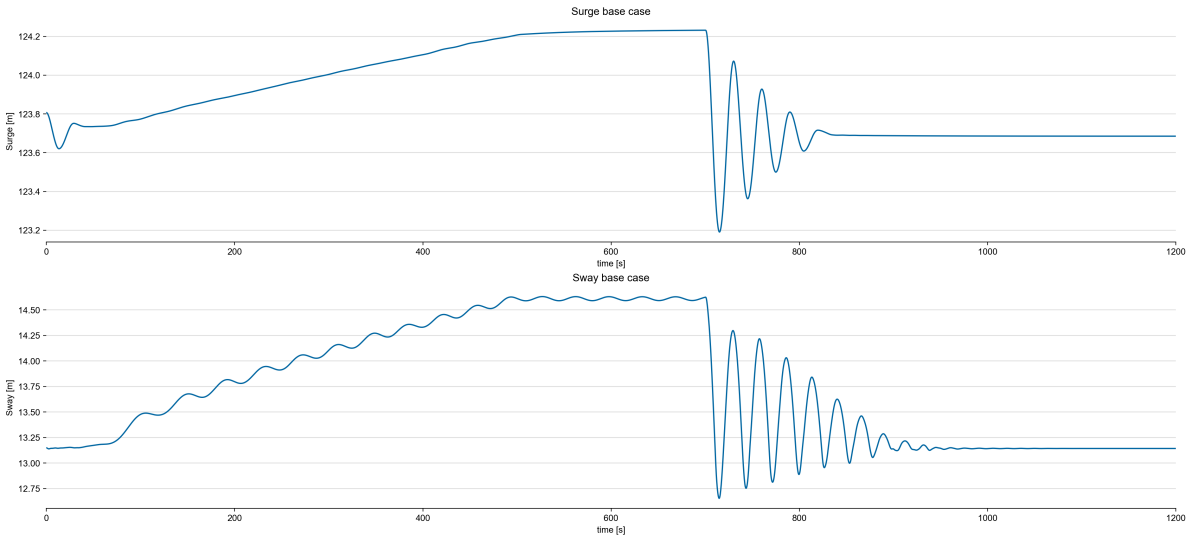

Figure E.1: Decay test base case for surge and sway

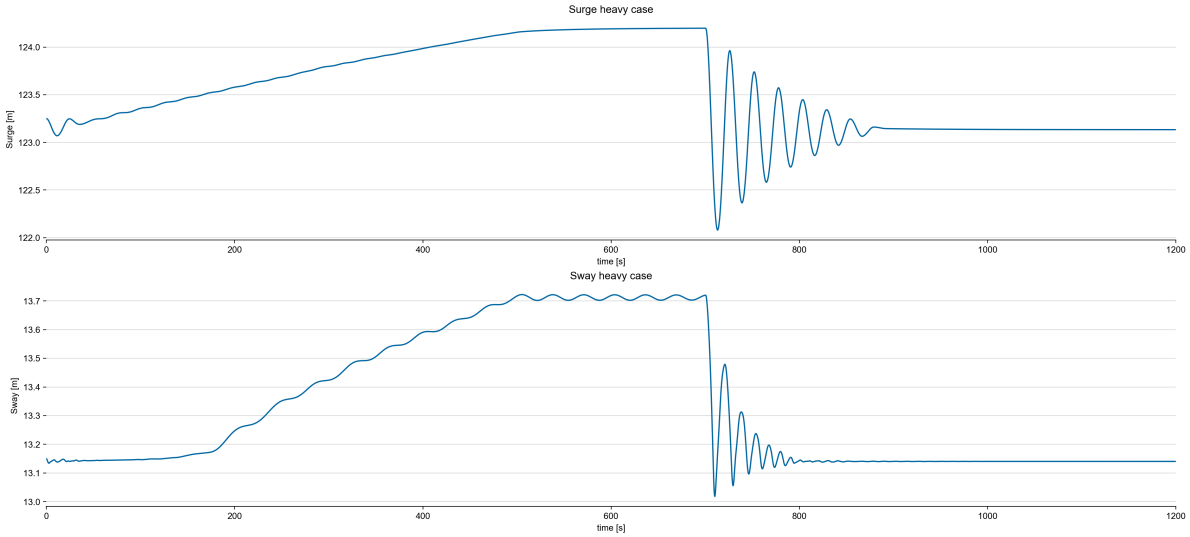

Figure E.2: Decay test heavy case for surge and sway

Appendix F

The modelled time series are presented in the report. Here, the related motion spectra will be shown.

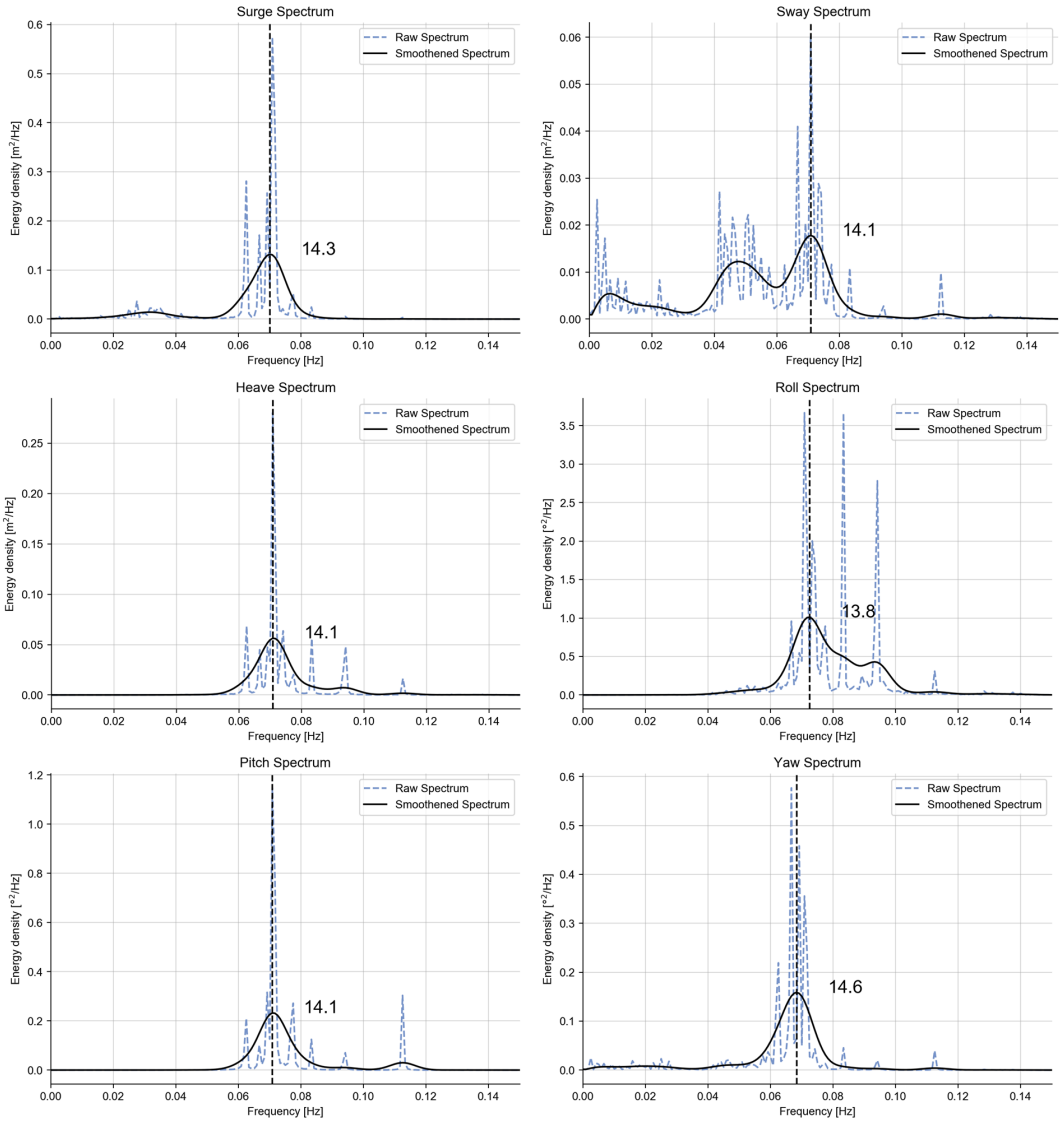

Figure F.1: Modelled motion spectra base case

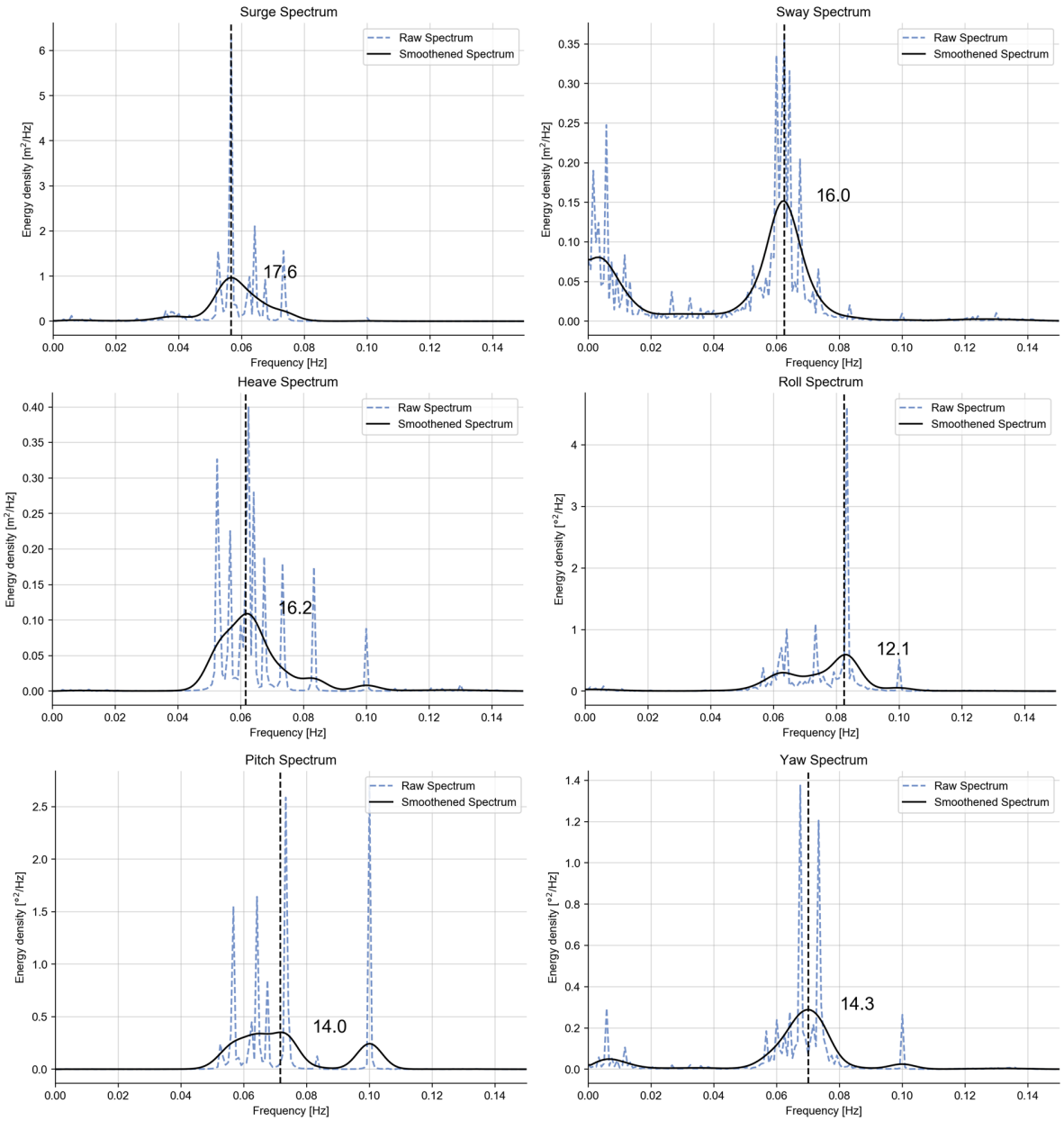

Figure F.2: Modelled motion spectra heavy case

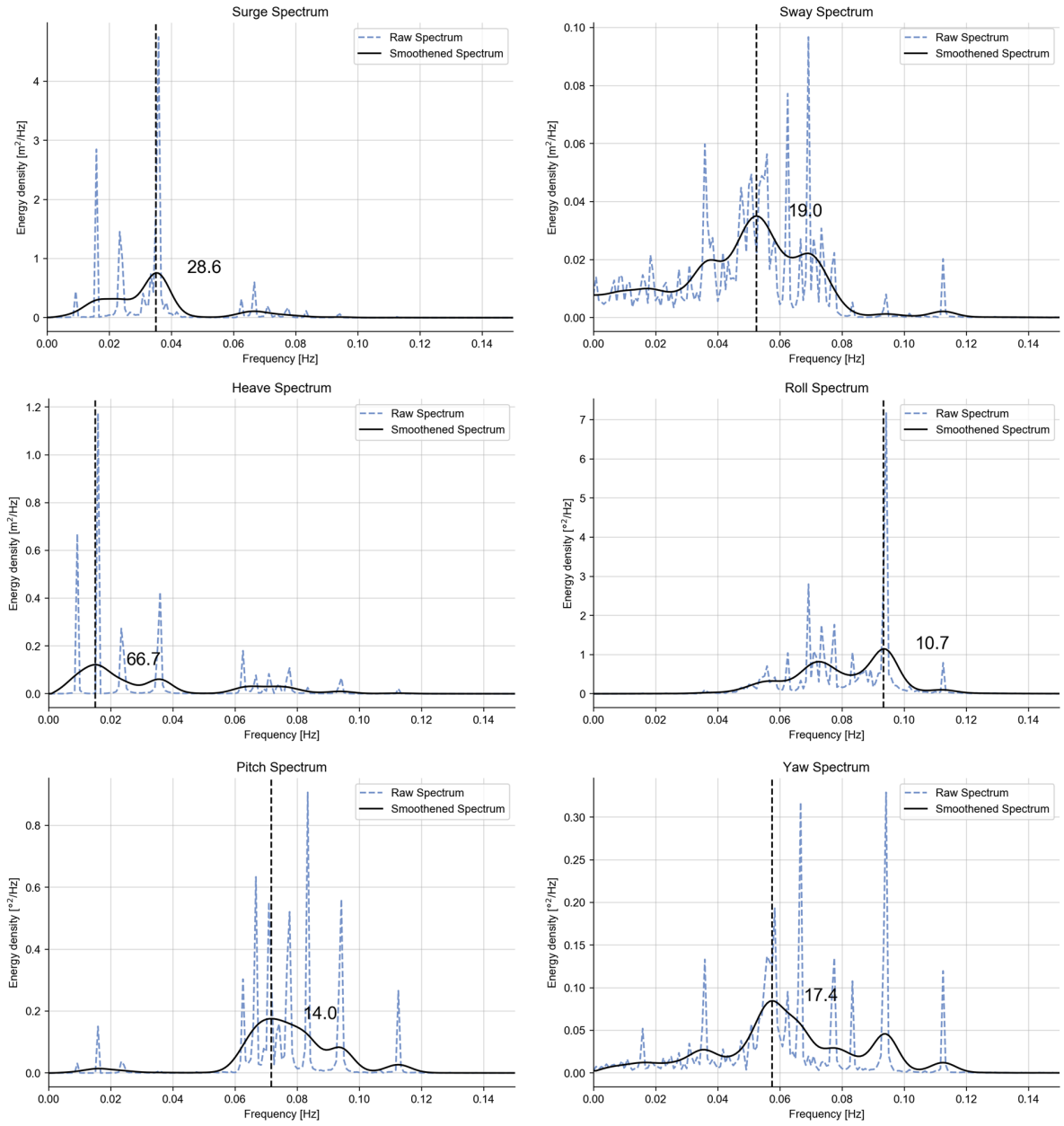

Figure F.3: Modelled motion spectra base case, ungrouped wth free long wave